Ph.D. THESIS UNIVERSITY COLLEGE LONDON

BOUNDARY AND BATHYMETRIC EFFECTS ON THE EVOLUTION OF ROTATING FLUIDS.

ROWENA GWENDOLEN ANN HURST.

ABSTRACT

The thesis examines several model flows in an attempt to elucidate the effects of boundaries and/or bathymetry on the development of a rotating flow. In particular, the numerical method of contour dynamics is employed in order to capture the combination of the nonlinear effects of advection and the effects of bottom topography. This method is based on the fundamental property of conservation of potential vorticity. Previous linear work on such topographic effects has not incorporated advection, thus in some cases this conservation law is violated. A brief review of others' work using contour dynamics is presented first, together with some simple examples to illustrate the uses of the method.

The first model flow then considered contains a cylindrical underwater obstacle. Various possible flow developments are revealed using the contour dynamics technique and in particular the effects of allowing a free surface are examined.

The influence of a sidewall on the formation of Taylor columns is the next problem approached. An underwater semi-cylindrical obstacle, flush against the wall, generates topographic waves in a uniform flow, which travel uni-directionally around the step. In previous such problems, where no wall is present, a Taylor column is set up on the timescale over which the fluid above the obstacle is spun down by Ekman pumping. In this case, however, the presence of the sidewall accelerates the formation of the Taylor column, which is now set up on the shorter topographic timescale.

The contour dynamics method is used again in the final chapter. In this problem uniform flow in a channel is forced over a longitudinal step, thus generating topographic waves. The resulting flow is highly dependent on the oncoming flow rate. It is shown that if the flow is sufficiently fast a permanent nonzero relative vorticity region is set up, whilst a slower oncoming flow allows the upstream propagation of the topographic waves, resulting in behaviour similar to that of hydraulic control.

TABLE OF CONTENTS.

ACKNOWLEDGEMENTS.

My grateful thanks go to Dr. E.R. Johnson for his help, encouragement and guidance throughout the work in this thesis. Thanks, too, go to Dr. M.K. Davey for his advice and suggestions, and to my friends and colleagues at U.C.L. Mathematics Department. I am grateful to Dr. D.G. Dritschel for the use of his contour dynamics code. Special thanks go to my husband, Dr. Robert Bowles, for his encouragement and help during the preparation of this manuscript.

Rowena Hurst, October 1990.

This work was made possible by the financial support of the S.E.R.C. and the U.K. Meteorological Office, Bracknell, Berks.

CHAPTER 1.

INTRODUCTION.

The complex behaviour of the oceans and atmosphere has long been a source of fascination for scientists. In spite of its complexity, however, this behaviour has proved to be well-represented by approximate scientific theory. The theory has, in general, been concerned with the fundamental dynamical concepts, rather than a detailed simulation, in order that from simple models a deeper understanding of the essential features may be gained. This knowledge can then be used both as a foundation for further investigation and as a tool for the interpretation of more complicated systems. In this thesis, a few simple model systems are examined in an attempt to isolate and hence illuminate some basic features of rotating flow over topography.

Historically, the subject of geophysical fluid dynamics is relatively young. The importance of the rotation of the earth was recognised by Hadley in the early eighteenth century, when he explained the easterly component of the trade winds by using the law of conservation of angular momentum, and also by Laplace, about fifty years later in his studies of the tides. In the latter half of the 19th century, Kelvin carried the subject further with his studies of the adjustment to equilibrium of a rotating fluid and in the early 20th century the work of Taylor led to, amongst other results, the fascinating "Taylor column" (Taylor 1923). But perhaps it was C.G. Rossby, in the late 1930s, whose pioneering work on rotating fluids is constantly acknowledged in the use of such basic concepts as the Rossby number and the Rossby radius, who laid the foundations for the subject as it is studied today.

One of Rossby's major contributions to the field was his investigation of the process by which a rotating fluid adjusts to equilibrium, Rossby (1937, 1938). This equilibrium is not a rest state, but a state of balance,

wherein the force of the pressure gradient is matched by the force due to the rotation itself, i.e. the Coriolis force. This balance was named geostrophy by Shaw (1916) and generally predominates in the large scale motions of the oceans and atmosphere. The geostrophic approximation is therefore an extremely powerful theoretical tool. However, due to an inherent mathematical degeneracy in the geostrophic equations of motion, it is insufficient to determine the dynamics of the system. It was with this degeneracy that Rossby was concerned.

In order to simplify the systems considered whilst remaining consistent with broad physical principles, several approximations are generally made, which remove unnecessary complications without losing the essential features of the flow which are the subject of the investigation. The assumptions made in this thesis, as elsewhere, include those of incompressibility and uniform density, ρ. Thus the effects of stratification are neglected here. In most of this work the fluid is assumed to be approximately inviscid, with the exception of the work in §4.4, which specifically considers viscous effects. In general the assumption that viscous effects are negligible is valid for large scale motions in the oceans and atmosphere because the Reynolds number is large. However, eddies and turbulence can be important. Here "large scale" is taken to mean motions for which the Rossby number, U/fL, is small, where U is a typical horizontal velocity scale, L is a typical horizontal length scale and the system rotates about a vertical axis with angular velocity f/2. A Rossby number of order unity or less implies that the effects of the rotation of the system are felt over the timescale of the motion, hence the Coriolis acceleration is at least as important as the relative acceleration of the fluid. In this work the Rossby number is assumed to be at most order unity, so it is to the large scale motions in the oceans and atmosphere that the results may be applied. For flows which are large scale but with horizontal scales

considerably less than the distance from equator to pole, the assumption may be made that the Coriolis parameter is constant, the f-plane approximation. Thus the curvature of the earth is not taken into account over the scales considered.

Another major assumption made is the shallow water approximation. The aspect ratios of the oceans and atmosphere are very small: a typical ocean depth may be 4 kilometers, while the horizontal length scales of some large scale motions may be hundreds or even thousands of kilometers. Thus the movement is essentially horizontal and vertical motions are relatively insignificant. This can be seen by considering the equation of conservation of mass, reduced by the earlier assumption of incompressibility to

$$\frac{\partial u}{\partial x} + \frac{\partial v}{\partial y} + \frac{\partial w}{\partial z} = 0, \tag{1.1}$$

where u,v,w are the components of horizontal and vertical velocities in the x, y, z directions respectively. By considering the orders of magnitude of each term it is clear that the vertical velocity scale, W, say, must be at most $O(\lambda U)$ where λ is the aspect ratio. A consequence of the relative insignificance of the vertical velocity follows from the vertical momentum equation, where the dominant terms are now the pressure gradient term and the gravitational acceleration, and is the last major assumption, the hydrostatic approximation, integrated to give

$$p(x,y,z) = \rho g(\eta - z), \tag{1.2}$$

where p is the pressure, g is the gravitational acceleration and $\eta(x,y)$ is the position of the surface of the fluid. In this assumption we are simply approximating the pressure at a point in the fluid by the weight of the

unit column of fluid above it at that instant. The horizontal momentum equations, incorporating all the above assumptions, are

$$\frac{\partial u}{\partial t} + u\frac{\partial u}{\partial x} + v\frac{\partial u}{\partial y} - fv = -g\frac{\partial \eta}{\partial x}, \tag{1.3a}$$

$$\frac{\partial v}{\partial t} + u\frac{\partial v}{\partial x} + v\frac{\partial v}{\partial y} + fu = -g\frac{\partial \eta}{\partial y}. \tag{1.3b}$$

The shallow water approximation implies that the horizontal velocities are independent of depth. This allows the integration of equation (1.1), which, on substitution of the boundary conditions at the surface, $z = \eta(x,y)$, and rigid bottom, $z = -H + h_B(x,y)$, where $h_B(x,y)$ is the bottom topography, becomes

$$\frac{Dh}{Dt} + h\left(\frac{\partial u}{\partial x} + \frac{\partial v}{\partial y} \right) = 0, \tag{1.4}$$

where $h = \eta + H - h_B$ is the total depth of fluid and $\frac{D}{Dt} = \frac{\partial}{\partial t} + u\frac{\partial}{\partial x} + v\frac{\partial}{\partial y}$ is the total derivative. Thus any increase in depth must be balanced by a horizontal convergence, so the volume of a given column of fluid remains constant.

The geostrophic approximation mentioned earlier may be derived from equation (1.3) by order of magnitude arguments. The relative acceleration terms on the left-hand side are smaller than the Coriolis term in each case, since the Rossby number is small, thus to leading order a balance is established:

$$v = g/f \frac{\partial \eta}{\partial x}, \tag{1.5a}$$

$$u = -g/f \frac{\partial \eta}{\partial y}. \tag{1.5b}$$

However, substitution of the above into equation (1.4)

only confirms that the flow is constrained to follow bottom contours in the geostrophic approximation, providing no new information. This is due to the degeneracy mentioned earlier. Taking the curl of equation (1.5) elucidates the problem. The curl of the pressure gradient is identically zero, whereas the curl of the Coriolis acceleration is the horizontal divergence of the geostrophic velocities, which, although small, is not zero. The geostrophic approximation is clearly only a first step, which must be amended and improved upon in order to determine the dynamics of the fluid. Equally clearly, it is the smaller, non-geostrophic terms, hitherto neglected, which must provide the extra information. It is through vorticity considerations that the further constraints on the flow are found. Due to the strongly two-dimensional nature of the flow, the only significant component of the vorticity is that in the vertical direction,

$$\zeta = \frac{\partial v}{\partial x} - \frac{\partial u}{\partial y}. \qquad (1.6)$$

The final equation required is found by taking the curl of equation (1.3) and substituting for the horizontal divergence using equation (1.4). The result is the equation of conservation of potential vorticity,

$$\frac{D}{Dt}\left[\frac{\zeta + f}{h}\right] = 0. \qquad (1.7)$$

The name "potential vorticity" was given to the quantity in square brackets by Rossby, who thus demonstrated that the development of an inviscid rotating fluid is eternally dependent on its initial state. It is the geostrophic approximations to the velocity and vorticity fields that are used in equation (1.7), thus the vital departures from geostrophy are included in the theory, without being found explicitly. By considering their

orders of magnitude, it is seen that the ratio of the relative vorticity, ζ, to the planetary vorticity, f, is given by the Rossby number. Thus in this work, wherein the Rossby number is at most order unity, the planetary vorticity is at least as important as the relative vorticity.

The extra information provided by this conservation equation enables us to establish both the development and the final steady state of a flow in a theoretical model, given the initial state. Kelvin (see Thomson 1879) considered such flows, with zero initial potential vorticity, but it was again Rossby who extended the work, to cover flows with non-zero initial potential vorticity. The final flow may be determined without considering the intermediate states, but in this thesis we are concerned mainly with the evolution of flows, i.e. with initial value problems, so here, by way of illustration, we briefly summarise some transient features which are often instrumental in the adjustment to equilibrium of a rotating fluid.

We consider first small perturbations to a flow containing no topography and seek a solution to the linear, unsteady equation for the surface displacement, η, obtained from the linearised shallow water equations:

$$\frac{\partial^2\eta}{\partial t^2} - gH\left(\frac{\partial^2\eta}{\partial x^2} + \frac{\partial^2\eta}{\partial y^2}\right) + f^2\eta = 0. \qquad (1.8)$$

A wavelike solution is possible, i.e. $\eta \propto \exp(ikx + ily - i\omega t)$, provided it satisfies the dispersion relation

$$\omega^2 = f^2 + (k^2 + l^2)gH. \qquad (1.9)$$

A very important length scale is apparent in this relation and in equation (1.8), namely the Rossby radius,

$a = (gH)^{1/2}/f$. This is the distance over which the surface is deformed equally by the gravitational effects and the effects of rotation. Thus over length scales which are small compared with the Rossby radius, the pressure gradient force dominates and rotational effects are scarcely felt by the surface, which therefore behaves as if it had a rigid lid. Over a larger scale, however, the effect of the Coriolis acceleration increases, dramatically altering the behaviour of the flow and dominating as the relative size of the Rossby radius tends to zero. In Chapter 3 this feature of rotating fluids is examined in detail, using a simple model with various values of the relative Rossby radius. It is shown that the flow is significantly altered and attains a qualitatively different final state for different values of the relative Rossby radius.

In Chapters 4 and 5, however, the rigid lid approximation is made, in which $g \to \infty$, but $g\eta$ remains finite. This is a realistic and widely-used approximation: in the ocean the gravitational acceleration is several orders of magnitude larger than the relative accelerations. This corresponds to the limit of infinite Rossby radius, in which the surface cannot deform over a finite length scale. Typical values for the Rossby radius vary between about 200 kilometers for a shallow sea and 2000 kilometers for deeper oceans.

From equation (1.9) it is clear that the behaviour of the wavelike solutions will depend on the relative size of the wavelength to the Rossby radius. If $(k^2+l^2)a^2$ is small, i.e. the waves are long compared with a, then the second term in (1.9), the so-called buoyancy term, is small, the frequency of the wave is approximately f, the inertial frequency, and gravity plays little part. If $(k^2+l^2)a^2$ is large, however, i.e. the waves are short, then the frequency $\omega \cong (k^2+l^2)^{1/2}(gH)^{1/2}$ i.e. the frequency of an ordinary gravity wave in a non-rotating system, and the effects of rotation are hardly felt. All the above waves are referred to as Poincaré waves. The

condition of no normal flow at a boundary cannot be satisfied by a Poincaré wave, so if an internal boundary is present in the flow a combination of these waves is required, known as a Kelvin wave. Such waves require the wavelength in the longshore direction to be much larger than the Rossby radius, so are not present in flows for which the rigid lid approximation is valid. The velocity normal to the boundary is zero, thus the (small) longshore component of the pressure gradient is not geostrophically balanced, but is balanced instead by the small longshore acceleration.

These waves, then, are some of the means by which a rotating fluid may adjust to geostrophic equilibrium and they have been widely used in time-dependent models. Here, however, we concentrate on another wave, whose existence depends on the presence of bottom topography, the topographic Rossby wave. With the advent of larger computing facilities, topographic effects are beginning to be incorporated in large scale models of ocean circulation. Simple theory and experiments caution that small topography can have large effects, particularly in the temporal evolution of relatively slow flows.

The existence of such a topographic wave can be inferred from the equation of conservation of potential vorticity, equation (1.7). It is clear that a change in the depth h of the fluid necessitates a change in the relative vorticity. This generation or destruction of vorticity can also be illustrated by considering a given column of fluid, moving to a region of deeper fluid. As its length increases, it must become narrower, to conserve its volume, as shown by equation (1.4). Thus its cross-sectional area decreases and therefore, by Kelvin's theorem, it experiences an increase of relative vorticity. Similarly, a fluid column moving into shallower fluid loses vorticity as it becomes broader. Now consider the effect that such a column has on its neighbours. A column that has moved to a deeper region will move neighbouring columns on its right into the

deeper region, and those on its left into the shallower region. The process is then repeated by the columns which have been thus moved. In this way the wave is produced and propagates along the change in depth, with the shallower fluid to its right, for an anticlockwise-rotating system. The above is a physical explanation in terms of vortex-stretching for the uni-directional phase propagation of the wave. Mathematically, this feature can be seen from the dispersion relation for the topographic Rossby wave,

$$\omega = - \frac{\beta k}{k^2+l^2+a^{-2}}, \qquad (1.10)$$

where the slope of the topography is assumed to be slight and is given by $h_B = \beta y$, with $\beta > 0$. Hence the phase speed normal to the slope, ω/k, is always negative. The maximum frequency for a given l,

$$\omega_{max} = - \frac{\beta}{2(l^2+a^{-2})^{1/2}}, \qquad (1.11)$$

is attained when $k = (l^2+a^{-2})^{1/2}$. Thus the absolute maximum frequency, when $l = 0$, is given by $-a\beta/2$ and is reached when $k = 1/a$.

It is the limiting case of a step in the bottom boundary which is considered in this thesis. The waves produced by a sudden change in depth are seen in continental shelf regions of the oceans, and have the vortex-stretching dynamics described earlier. Although the abrupt change in depth violates the assumption that the slope is small, these shelf waves have many features in common with Rossby waves, and indeed they may be regarded as a limiting form of a Rossby wave. (see Pedlosky (1987) §8.2, Gill (1982) §10.12 and Longuet-Higgins (1968)).

These waves may be produced by isolated topographic

features as well as in continental shelf regions, and the particular case of a flat-topped cylindrical sea-mount in a uniform stream is considered in Chapter 3. Here the interaction of topographic waves with the effects of advection are illustrated. The advective timescale, L/U, where L is a typical horizontal length scale and U is a typical horizontal velocity scale, is taken to be comparable with the topographic vortex-stretching timescale, which is inversely proportional to the background rotation rate and the fractional height of the obstacle, i.e. $(f\delta)^{-1}$. In this chapter both δ and the Rossby number are taken to be very small. In the absence of advective effects the waves cycle the obstacle indefinitely, as shown by Johnson (1984). This is no longer possible in the presence of advection, and the effects of the topographic waves combine with those of advection to determine the development of the flow. It is shown that the evolution depends on the relative strengths of these effects, measured by a parameter referred to throughout as the Hide parameter, after Hide (1961), given by $S = \delta/Ro$, where Ro is a Rossby number for the flow. If advective effects dominate, i.e. the Hide parameter is small, the fluid is swept away downstream before the topographic wave has had much influence. In this case a cyclonic eddy is produced by the fluid originally above the obstacle moving into the deeper region. This eddy is then advected away by the uniform stream, along a path which is found analytically. Similarly an anticyclonic vortex is produced over the obstacle by fluid moving up and hence losing vorticity. This vortex is constantly replenished by new fluid being carried in from upstream. At the other extreme, if topographic effects dominate and the Hide parameter is large, the original fluid remains in the vicinity of the obstacle for longer and some may be trapped over the topography, thus forming at least part of a "Taylor column".

This fascinating phenomenon was first demonstrated by

Taylor (1923), who towed a short obstacle slowly across the base of a rotating tank. The fluid above the obstacle was found to be at rest relative to it, whilst outside this region the flow was two-dimensional. This result is predicted by the Taylor-Proudman theorem (Proudman (1916), Taylor (1917)), which states that the slow, steady flow of a rapidly rotating, homogeneous, incompressible, inviscid fluid must be depth-independent. Much theoretical and experimental work has since been carried out on this strange feature of rotating fluids. Hide (1961) showed that for Taylor columns to exist the aforementioned Hide parameter must exceed a certain critical value. In Chapter 3 the effects of a free surface are examined, and this critical value of the Hide parameter is found as a function of the Rossby radius of deformation. It is found that as the Rossby radius decreases the topographic effects become more localised, so the fluid is less likely to be trapped by the obstacle, hence a larger value of the Hide parameter is required for the existence of a Taylor column. Similarly, as the Rossby radius tends to infinity, i.e. in the rigid lid limit, the critical Hide parameter has a minimum value which is that given by Huppert (1975).

Fluid may also be captured from upstream, as it is carried over the obstacle, provided the Hide parameter is sufficiently large. This is illustrated in Chapter 3 in the particular case where there is an upstream eddy which is advected towards the obstacle. It is assumed that the fluid originally over the obstacle has been swept away by an earlier episode of faster flow, and the oncoming eddy may be assumed to have been produced by another topographic feature, further upstream. It is found that an upstream eddy with negative vorticity, i.e. vorticity of the same sign as the topographic vortex over the obstacle, with which it interacts, may be partially captured by the topography, while a positive eddy is merely deflected by the obstacle as it passes.

The problem is further extended in Chapter 3 to

consider an oncoming shear flow rather than a uniform stream. Now two cyclonic vortices are shed, whose paths may again be approximated analytically. Again some fluid may be trapped above the topography and the results are compared with the steady solutions of Johnson (1983). As found by the latter, the results for positively sheared flows are shown to be qualitatively different from those for negatively sheared flows.

Taylor columns are examined further in Chapter 4, with the emphasis in this case on the effects on their development produced by the presence of a sidewall. Unlike the regime of Chapter 3, the advective timescale is here assumed to be long compared with the vortex-stretching timescale, over which the development is followed, so that the only effects considered are those of the topography and the sidewall. It is shown that a Taylor column is set up on this shorter timescale, in contrast to the result of Johnson (1984) that a topographic wave cycles an isolated obstacle indefinitely, thus the presence of a sidewall is shown to accelerate Taylor column formation. The reason is clear, the waves, being uni-directional, cannot propagate indefinitely when the isobaths end abruptly. The particular geometry considered is a flat-topped, semi-cylindrical obstacle, flush against the sidewall. The waves travel around the edge of the obstacle, but can go no further when they reach the wall-step junction. A Kelvin wave is not possible here, as the rigid lid approximation has been made.

Although the governing equation of conservation of potential vorticity is linear in this case, the advective terms being negligible, the final steady state achieved satisfies the nonlinear equation for advection of potential vorticity, thus time dependence has here given a specific solution to a nonlinear problem. Furthermore, the results, like those of Johnson (1985), are more widely applicable. A parameter HRo/L was introduced by Stewartson & Cheng (1979) which measures the importance

of inertial effects on the flow. For Ro « 1, the vertical wavelength of a typical topographically forced inertial wave is L/Ro, Johnson (1982). Thus the flow is effectively two-dimensional provided H « L/Ro, i.e. H/L « Ro^{-1}, a weaker condition than that for the shallow water approximation to be valid. Therefore these results apply also to slow flows with depth of the order of, or greater than, the obstacle width.

In §4.5 nonlinear effects are considered. For obstacles of fractional height of order unity, these become important for Rossby numbers of order unity and solutions are presented for arbitrary step height, under the assumption that the flow is sufficiently fast to have advected downstream all fluid initially above the obstacle. For obstacles of very small fractional height, nonlinear effects become important for Rossby numbers much less than unity. In this limit, as above, the restriction to shallow flows can be lifted, and the results apply to deep flows provided that H/L « Ro^{-1}. It is in this limit that the fractional height and the Rossby number combine to give a finite Hide parameter.

It is in Chapter 4 that the effects of viscosity are considered. It is shown in §4.4 that viscosity arrests the flow at some stage in its evolution, thus some fluid still crosses the obstacle in the steady state. These solutions suggest that experimental results on separation for a similar geometry obtained by Griffiths & Linden (1983) can tentatively be ascribed to entrainment and expulsion of fluid through vertical shear layers at the edge of the topography.

In Chapter 5 we return to the parameter regime of Chapter 3, in which the advective and topographic timescales are comparable. The ratio of these effects, given by the Hide parameter, is again shown to be crucial in determining the flow evolution. In this chapter the geometry is somewhat more complicated than that of Chapter 3, incorporating boundaries. The fluid is advected along a channel of uniform width. The topography

consists of a longitudinal step, separating a deep region beside one wall from a shallower region beside the other. There is a cross-stream perturbation to this step at some point along the channel, which, in a similar fashion to the topography in Chapters 3 and 4, generates regions of nonzero relative vorticity as fluid is advected to a new depth. For small values of the Hide parameter, i.e. for fast oncoming flows, all fluid is swept downstream, leaving a region of positive relative vorticity, in a similar way to the fast flows of Chapter 3. For larger values of the Hide parameter, however, the topographic waves can propagate upstream and a more complicated flow results.

Various limiting cases are examined analytically in §5.3. The results are compared in §5.4.1 with those found numerically using the contour dynamics technique and are shown to agree well. In the second part of §5.4 the computations are carried out for regions of parameter space which are not covered by these theories and qualitatively new results are revealed.

The numerical method used in Chapters 3 and 5, to follow the evolution of a rotating fluid under both topographic and advective influences is the method of contour dynamics. This highly efficient technique permits the nonlinear development of inviscid, two-dimensional flows with bounded patches of uniform vorticity to be modelled, allowing potential vorticity to be advected with the fluid, as is the case in reality. A further advantage of contour dynamics is again due to its roots in the equation of conservation of potential vorticity. The evolution of the entire flow can be determined by following the boundary which divides regions containing differing amounts of potential vorticity. Thus the two-dimensional problem is reduced to one dimension, hence contour dynamics has a great advantage over, for example, finite-difference schemes, which compute the velocity over a grid covering the entire area of fluid, and which must become unreliable as increasingly smaller

scales develop. The contour dynamics algorithm used allows for the development of smaller scales, as the resolution along this boundary is automatically adjusted at each time step.

The method is based on the fact that the flow field is determined solely by the instantaneous vorticity distribution and the boundary conditions. All particles conserve their potential vorticity, thus if the initial vorticity distribution is known, then at later times both it and the velocity distribution can be calculated. Chapter 2 first presents a review of some of the studies by earlier workers involving the method of contour dynamics. This provides some basic results and a background for the work of this thesis. A full description of the method is then given, together with some simple examples to illustrate part of the range of problems to which it may be applied.

CHAPTER 2.

THE CONTOUR DYNAMICS METHOD AND SOME APPLICATIONS.

§2.1 Introduction.

The method of contour dynamics is a relatively new numerical technique, based on the nonlinear equation of conservation of vorticity. The fact that the velocity field can be determined at all times by the instantaneous distribution of vorticity is used to reduce the two-dimensional task of calculating the velocity field throughout the flow to the one-dimensional problem of tracking the boundaries between regions of fluid with differing vorticity strengths. By concentrating the computational effort on this more specific task, much unnecessary calculation is avoided and the method allows the computation to continue far longer and more cheaply than a similar two-dimensional scheme would permit.

A brief introductory review of some of the studies carried out using contour dynamics is presented first, in order to illustrate some uses of the method, to set a background for the work of this thesis, and to provide some basic results which act as useful tools in understanding more complicated systems.

The method itself is described in detail in §2.2 and in §2.3 a few simple examples are given, showing a range of flows to which the method may be applied.

From the above description, it is clear that the contour dynamics method is particularly suitable for flows containing piecewise constant vorticity regions and this has led to applications in several fields, including that of geophysical fluid dynamics with which this thesis is concerned. For example, one major motivation of contour dynamical work has been the study of high Reynolds number flows. It is widely accepted that such flows generally develop coherent vortical structures, however the flow is forced. These structures, having formed, then dominate the flow evolution. This has led to a great deal of contour dynamical work on the dynamics of vortex patches and the nonlinear behaviour of the

boundaries of such regions.

A few fundamental results on vortex patch behaviour are outlined below. Various extensions to these results are then described. Deem & Zabusky (1978) find a class of "finite area vortex regions" (FAVRs) which rotate uniformly without change of shape, and similarly a class of FAVRs which translate uniformly. They refer to the members of these classes as "V-states". The rotating V-states are found to have m-fold symmetry; a well-known example is the Kirchoff ellipse (see Lamb 1932), shown in Figure 2.1, for which m=2. This V-state rotates with angular speed $\omega = ab\sigma/(a+b)^2$, where a and b are the major and minor axes respectively and σ is the vorticity strength within the ellipse. This example of vortex patch behaviour is often used as a test of the accuracy of contour dynamical algorithms. The translating V-states are pairs of opposite-signed FAVRs, i.e. regions containing vorticities of equal magnitude but opposite sign, which propagate in a direction perpendicular to the line joining their centres, with a speed dependent on the distance between them. This class may be regarded as a generalisation of the case of a pair of opposite-signed point vortices. Saffman & Szeto (1980) add the class of uniformly co-rotating V-states, i.e. a pair of FAVRs which rotate as a pair without change of shape.

A further investigation of the behaviour of FAVRs is carried out by Zabusky, Hughes & Roberts (1979) who examine the mutual interaction of such regions. It is shown that a pair of similarly-signed circular FAVRs rotate about one another, experiencing surface deformations which become increasingly more severe with decreasing inter-vortical distance. If the vortex regions are brought sufficiently close to each other, "arms" of vortical fluid are ejected, which then wrap around the other region. Figure 2.2 shows a case where the regions were initially so close that they have become entirely wrapped around one another.

The above basic results form a foundation for further

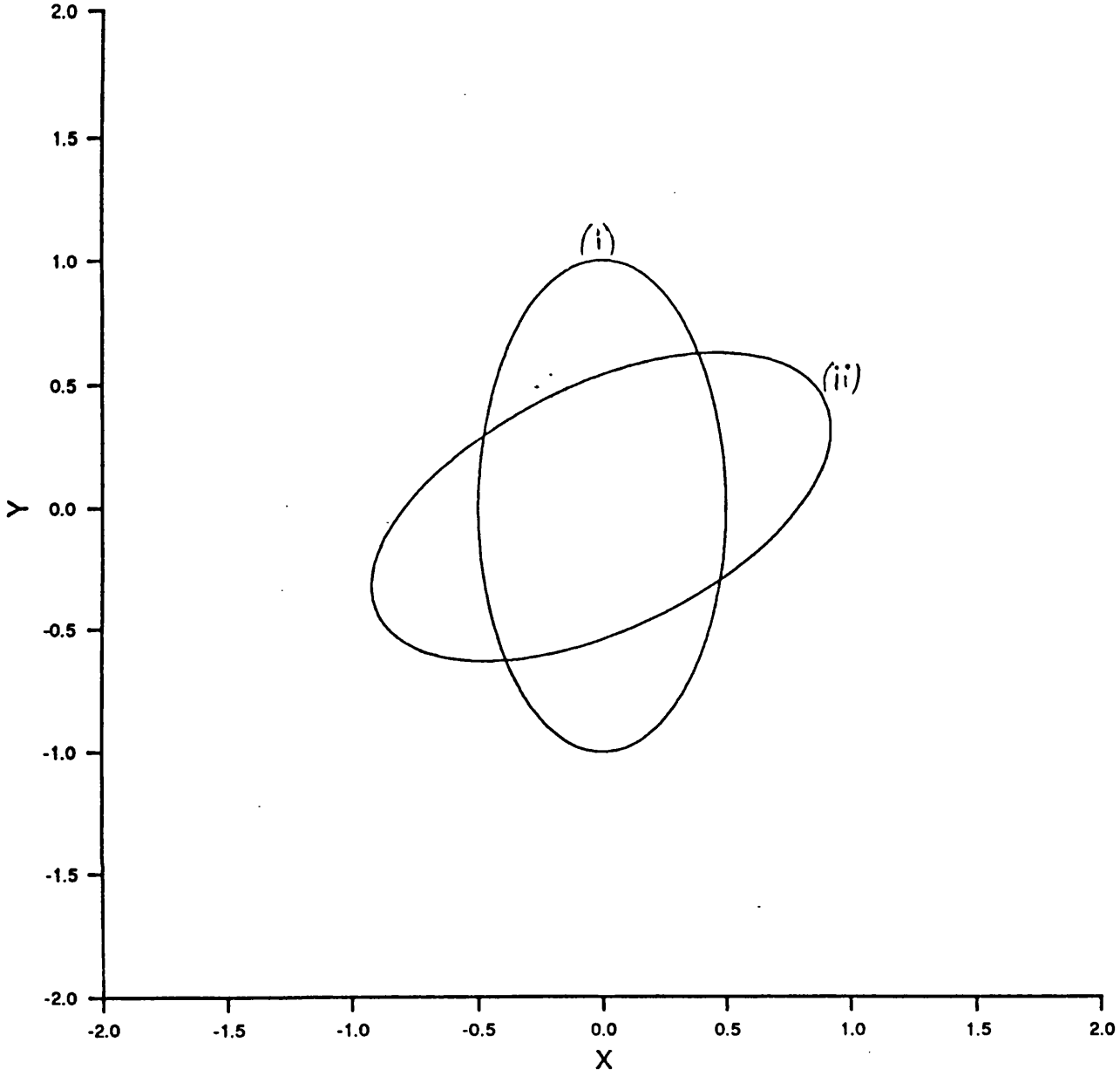

Figure 2.1

A steadily rotating elliptical vortex patch at (i) t = 0 and (ii) t = 1. The strength of the vorticity, σ, is 5 and the semi-axes are of length .5 and 1. The rotation rate is given by $\omega = \sigma ab/(a+b)^2$.

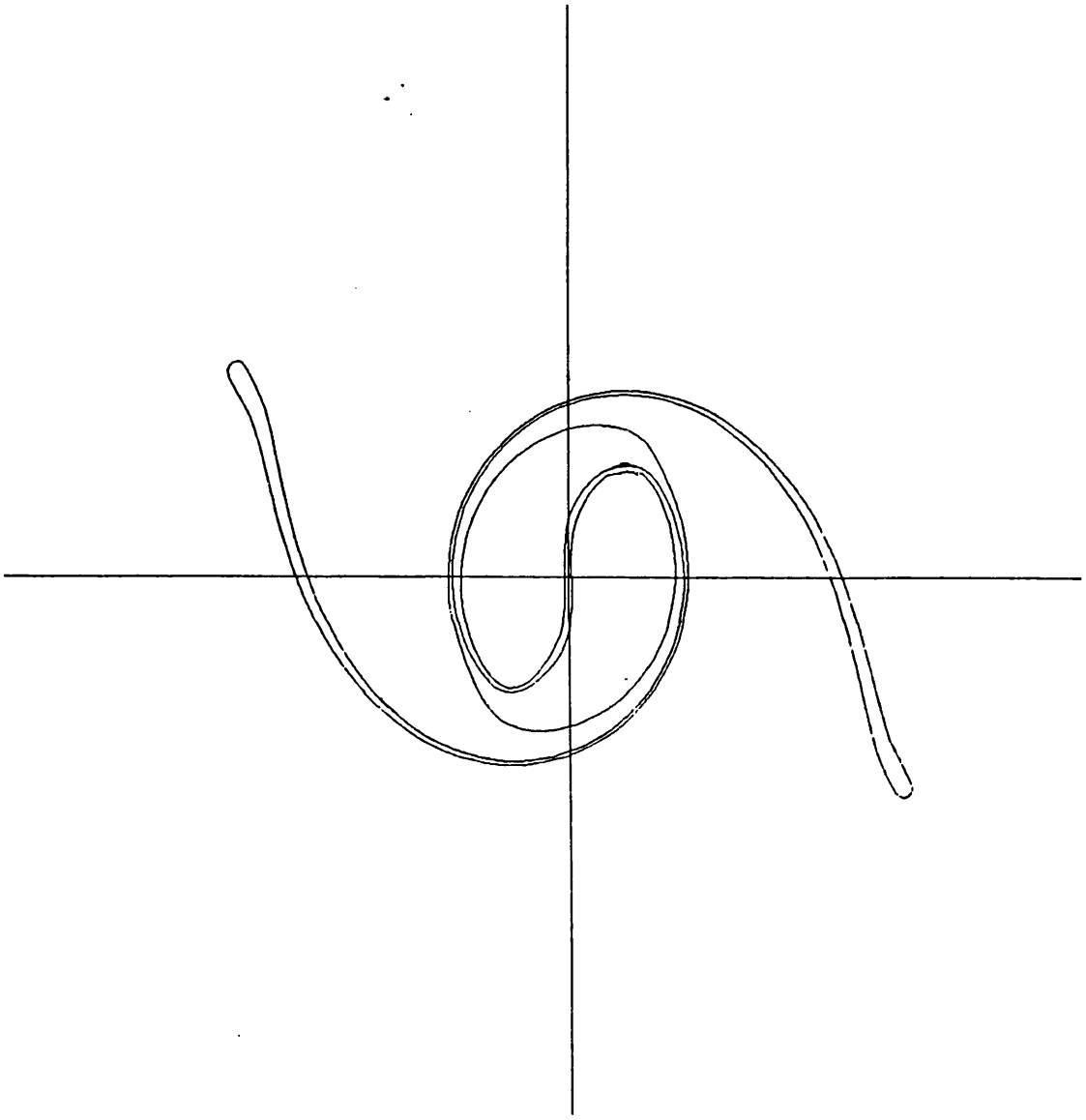

Figure 2.2

The mutual interaction of two FAVRs. The patches are initially circular, with centres at (±.7,0) and radius .5. They are drawn towards one another, eject arms about each other and finally become completely wrapped up in each other.

exploration of vortex-patch dynamics. Modifications and improvements to the contour dynamics method have allowed extended examinations of more complicated flows. One aspect of the original method which clearly needed immediate improvement was the problem of resolution along a contour, i.e. along a boundary of a vortex patch. The contour is modelled by a discrete number of points, known as "nodes", and as the flow evolves these nodes tend to become widely separated along some parts of the contour, leading to inaccuracy in the computation. Several "renoding" schemes have been devised, wherein the number of nodes required to satisfy a pre-set standard of accuracy is determined and the optimum positioning for them along the contour calculated. Most such schemes use the local curvature to determine the number of nodes required - regions of higher curvature need a greater number of nodes to resolve them accurately. This procedure allows the computation to continue longer without loss of accuracy.

Having obtained this greater accuracy for longer times, it became possible to use the contour dynamics for more detailed investigations. With the recognition of the basic V-states described above there naturally arises the question of stability. This line of enquiry has led to a great deal of contour dynamical work. Overman & Zabusky (1982) show that if two co-rotating V-states are perturbed beyond what the authors call the "point of exchange of stability" they will merge to form an ellipse, with extending arms of fluid being ejected at each end. These arms then "roll-up" at their tips. In the same work the "entrainment" of one FAVR by another is demonstrated, i.e. the phenomenon where one vorticity patch completely surrounds another.

Dritschel (1986) compares the nonlinear evolution of various vortex systems with the corresponding known linear stability theory. He illustrates the interesting point that transition from one equilibrium state to another is possible in some cases, for example a

perturbed ellipse may evolve into two stable vortex patches. Moreover this process may be reversed to recover the original ellipse. He finds that nonlinear instabilities occur in marginally linearly stable flows, for example an annulus may split into several distinct centres of vorticity, while flows which are linearly stable are shown to maintain this stability in the nonlinear case. This would seem to suggest that the parameter range for nonlinear stability is the same as that in the linear case. A further comparison with linear theory, this time for an elliptical vortex patch in an external straining flow, is carried out by Dritschel (1990). Here the effect on a vortex patch of randomly distributed distant vortices is modelled by a steady external straining flow together with a slight disturbance to the vortex boundary, to allow for variation in the external flow due to the other vortices. The contour dynamical results are compared with linear Floquet theory. The results are found to differ both in that linearly stable cases are found to be unstable and that linearly unstable cases appear to return recurrently close to the initial state.

The basic V-state results are extended by Polvani, Zabusky & Flierl (1989) to consider a two-layer fluid, as a first step towards geophysically relevant three-dimensionality. They examine the case wherein the lower layer has constant potential vorticity and find that the upper layer can be treated in a similar way to the one-layer case, but with a modification in the velocity calculation. The results show that in general the V-states found in the upper layer are similar to those for the one-layer case, except in the "equivalent barotropic" case, where the depth of the lower layer tends to infinity. This case is referred to in more detail in Chapter 3 of this thesis, which considers the similar case of a two-layer fluid with an infinitely deep upper layer.

Pullin & Jacobs (1986) present a further extension to

the fundamental studies of FAVRs, relaxing the somewhat restrictive condition of entirely uniform vorticity patches, by allowing nested contours. They consider pairs of counter-rotating elliptical vortices, each consisting of 4 nested contours, in an external strain field. Thus the evolution of each contour is determined by three agents: the local strain from the other vortices; the amplification of the vorticity by the external strain and the self-induction of the vortex. Their results show an intense rotating core developing in each vortex, while arms of vortical fluid spiral outward. If the external strain is strong, local instabilities develop on these arms and roll-up occurs at the tips.

A major departure from the original idea of an isolated patch of uniform vorticity is the inclusion of some external geometry in the flow. Much work has been carried out on flows adjacent to a wall. Pullin (1981) examines the effect of a finite amplitude sinusoidal disturbance to a layer of constant vorticity, beside a wall. The linearised solution, due to Rayleigh, shows a neutrally stable Kelvin-Helmholtz wave on the contour. However, as the disturbance amplitude is increased, it is shown that wedges of irrotational fluid may be entrained by the layer, in the valleys. This occurs for a broad range of wavelengths and with no preferred layer width. It happens if the lower part of the valley crosses the critical layer of the shear layer and is therefore convected against the direction of propagation of the wave, causing "overturning".

The periodicity of the above work is relaxed by Stern & Pratt (1985), with reference to coastal flows. They examine the evolution of the front, i.e. the bounding contour, as it develops from a given initial position. In particular, they study the development of the leading edge of an "intrusion" of constant vorticity, i.e. a layer which does not extend to infinity in the positive longshore direction. Longwave theory predicts a steepening of this leading edge, but it is shown that the

shortwave effects act as a balance to this process, leading to an equilibrium state. Lee waves are seen to develop behind the leading edge and "backward breaking" occurs, i.e. the crest at the leading edge folds back on itself, if the initial slope is above a suggested critical value.

A feature of such coastal currents in the ocean is a plume of coastal water extending far away from the shore. Stern (1986) isolates the dominant dynamics involved in the production of such features using contour dynamics, with an intrusive wall layer. The plumes are successfully generated and in some cases are seen to "pinch-off" from the rest of the rotational fluid. This pinching-off process is examined in more detail by Pratt & Stern (1986), with reference to the warm/cold core rings formed by the Gulf Stream. In their computations, the front initially contains one or more meanders, developing in some cases into elliptical eddies which are then pinched off. It is shown that wave dispersion acts to inhibit the pinching-off process, whilst the steepening of the meander acts to accelerate it. Interestingly, pinching-off may be more likely if a small wavelength mode is present, as this acts to inhibit the dispersion process.

The study of instabilities on the boundary of a constant vorticity layer by a wall has applications in the investigation of the onset of turbulence in high Reynolds number flows. This is the motivation for the contour dynamical work of Stern (1989), who considers such a layer, perturbed by a small patch of irrotational fluid immediately beside the wall, wholly contained in the shear layer, which is otherwise stable. It is shown that a strong instability can develop and that this patch of irrotational fluid may be brought out, into contact with the external free stream, while high velocity fluid from the outer part of the shear layer is brought close to the wall.

An analogy of the work mentioned earlier using nested

contours in FAVRs is carried out by Jacobs & Pullin (1989). They model a flow with several parallel nested uniform vorticity regions, of infinite length, in an external uniform strain field. Their results show initial perturbations leading to the formation of discrete cores of vorticity within the layer, which wrap around each other in a similar way to the basic FAVRs shown in Figure 2.2.

A ubiquitous problem occurring in contour dynamical simulations is that of "filamentation". In some circumstances a small instability on a contour may develop into an extremely long, thin strand of vorticity, which continues to grow and therefore demand more nodes than can eventually be provided. The computation therefore has to be terminated shortly after the onset of this phenomenon. Investigations of this process have been carried out, for example Pullin, Jacobs, Grimshaw & Saffman (1989) discuss the filamentation of spatially periodic waves on vortex layers of finite thickness and suggest possible mechanisms which may give rise to the process. One way of dealing with the phenomenon of filamentation, devised by Dritschel (see Dritschel 1988, 1989) is to truncate the contour when the width of the filament is less than a pre-set value. This procedure is one aspect of "contour surgery", a set of such contour dynamical modifications. Another is a mechanism which allows the merging of distinct contours containing the same vorticity when they come sufficiently close to one another. These devices allow the computation to continue longer, by removing the increasingly small spatial structures which otherwise tend to develop. One feature of contour surgery which is used in this thesis is the insertion and removal of "corners" along the contour, which are required when the angle of the contour is less than $\pi/2$ at a node. The renoding scheme used herein is also due to Dritschel (see Dritschel 1988) and uses a node density function which is a nonlocal function of curvature.

Clearly a weakness of the contour dynamics method is the restriction to inviscid flows. In the field of geophysical fluid dynamics this is not a great disadvantage, since a lot of the flows considered may be taken as effectively inviscid. However, the restriction has led to some disagreement over the validity of the method for application to high Reynolds number flows. The problem of viscosity is approached by Zabusky & Overman (1983), who introduce "contour regularization" procedures, to represent aspects of dissipative or dispersive processes. These procedures inhibit the development of singularities on the contour, allowing the computation to continue longer.

As well as the major fields of contour dynamical work mentioned above, i.e. V-state stability studies and shear layer work, the contour dynamical method has applications to a wide range of flows. An example of a quite different application of the method is given by Hermann, Rhines & Johnson (1989). In this work the well-known process of linear Rossby adjustment is extended to include nonlinear advective effects. Fluid in a channel, with an initial discontinuity in free-surface height, adjusts geostrophically at first, producing an antisymmetric pair of boundary currents travelling along the sidewalls. This is taken as the initial state for the contour dynamical computation. It is shown that on the longer, advective timescale, which this method is able to model, fluid travels downstream along both walls and eventually all fluid is washed downstream, in complete contrast to the linear solution.

Another important geophysical application of the contour dynamics method is made by Kozlov (1983), in an investigation of the effects that an underwater obstacle has on the uniform flow of a rapidly rotating fluid. The evolution of the vorticity patches generated by vortex-stretching and compression is modelled using a contour dynamical algorithm. It is with geophysical applications of contour dynamics that this thesis is

concerned and in particular with the effects of topography on rotating flows. An extension to the work of Kozlov (1983) is carried out in Chapter 3, which examines the effects of allowing a free surface and a different oncoming flow, as well as continuing the calculations longer to explore the possible final steady states. In Chapter 5, flow over topography in a channel is analysed and behaviour similar to hydraulic control behaviour is revealed. In both these contour dynamics chapters the results of the workers cited in this section prove valuable in interpreting and understanding the flows under consideration.

§2.2 The contour dynamics method.

As mentioned in §2.1, this method is particularly suitable for flows containing discrete regions of uniform potential vorticity. For such a flow the equation of conservation of potential vorticity, equation (1.7), ensures that within these regions the fluid retains this potential vorticity for all time. The relative vorticity of the fluid may be altered, however, by the stretching and compression of fluid columns, as described in Chapter 1. From the value of the relative vorticity, the stream function for the flow and hence the horizontal velocities may be calculated. This is the basis for the contour dynamics technique.

If the surface displacement, $\eta(x,y)$, and the topography, $h_B(x,y)$, are taken to be small, then equation (1.7) may be linearised to give

$$\frac{D}{Dt}\left[\frac{g}{f} \nabla^2\eta - \frac{f}{H} \eta + \frac{f}{H} h_B \right] = 0. \qquad (2.2.1)$$

From equation (1.5) it is clear that a stream function for the flow, $\Psi(x,y)$, may be introduced, given by $\Psi_y=-u$, $\Psi_x = v$. Equations (1.2), (1.5) then give the pressure and the surface displacement in terms of Ψ as

$$(f\rho)^{-1} \underline{\nabla} p(x,y) = gf^{-1} \underline{\nabla}\eta(x,y) = \underline{\nabla}\Psi(x,y). \qquad (2.2.2)$$

Nondimensionalising equation (2.2.1) using the following scalings

$$x = Lx' \ ; \ y = Ly' \ ; \ \Psi = UL\Psi' \ ; \ h_B = \delta H h_B',$$

and dropping the primes gives

$$\frac{D}{Dt}\left[\nabla^2\Psi - (L/a)^2 \Psi + Sh_B \right] = 0, \qquad (2.2.3)$$

where $S = \delta/Ro$ is the Hide parameter which was introduced in Chapter 1 and which measures the ratio of topographic to advective effects. It will be shown throughout this thesis that this parameter is of fundamental importance in the evolution of rotating flows over topography.

Consider a flow containing j discrete regions, A_j, of uniform initial potential vorticity, Ω_j. The contribution to the stream function from region A_j is given by

$$\nabla^2\Psi_j - (L/a)^2 \Psi_j + Sh_{Bj} = \Omega_j. \qquad (2.2.4)$$

Clearly a nonzero value for $h_{Bj}(x,y)$ may be taken to simply alter the magnitude of the right hand side of equation (2.2.4). In the rigid lid limit, which is used throughout §2.3 and Chapter 5, the nondimensional Rossby radius, a/L, is taken as infinitely large and hence the second term of equation (2.2.4) vanishes in this limit, leaving Poisson's equation

$$\nabla^2\Psi_j = -Sh_{Bj} + \Omega_j. \qquad (2.2.5)$$

In Chapter 3, a free surface is allowed and the equation for $\Psi_j(x,y)$ is the Helmholtz equation

$$\nabla^2\Psi_j - (L/a)^2\Psi_j = -Sh_{Bj} + \Omega_j. \qquad (2.2.6)$$

Equations (2.2.5), (2.2.6) may be solved in terms of Green's functions and hence the solutions may be written respectively as

$$\Psi=\sum_j \Psi_j(x,y)=(2\pi)^{-1}\sum_j(\Omega_j-Sh_{Bj})\iint_{A_j}\log r\,dx_0dy_0, \qquad (2.2.7a)$$

$$\Psi=\sum_j \Psi_j(x,y)=-(2\pi)^{-1}\sum_j(\Omega_j-Sh_{Bj})\iint_{A_j}K_0(rL/a)dx_0dy_0. \qquad (2.2.7b)$$

where $r^2 = (x-x_0)^2 + (y-y_0)^2$ and K_0 is the modified Bessel function of zeroth order. Thus it can be seen that the effect of a patch of vorticity decays exponentially with distance if a free surface is allowed, whereas the decay is only logarithmic if the rigid lid approximation is made. This point is explored in greater detail in Chapter 3.

The respective horizontal velocities $\underline{u}(x,y)$ may be found by differentiation of equations (2.2.7) and the use of Green's theorem to be:

$$\underline{u}(x,y) = (2\pi)^{-1}\sum_j(\Omega_j-Sh_{Bj})\int_{\partial A_j}\log r(dx_0,dy_0), \qquad (2.2.8a)$$

$$\underline{u}(x,y) = -(2\pi)^{-1}\sum_j(\Omega_j-Sh_{Bj})\int_{\partial A_j}K_0(rL/a)(dx_0,dy_0), \qquad (2.2.8b)$$

where ∂A_j is the boundary of region A_j. It is these integrals which are evaluated by the contour dynamics program. The velocity at each node along the boundary having been thus calculated, the new nodal positions can then be found, by integrating

$$\frac{dx}{dt} = u \quad ; \quad \frac{dy}{dt} = v. \qquad (2.2.9)$$

The nodes are re-positioned and the new velocities calculated. In this way the entire contour is advected, with no need to calculate the rest of the velocity field.

In order to evaluate the integrals in equation (2.2.8), the sections of contour between each pair of nodes are approximated by cubics. The contributions to the velocity integral for a given node from each of these small sections are calculated separately and the results are

added to give the total velocity at that node. The cubic approximation to a contour-section is given by

$$\eta^*(p) = \alpha_i p + \beta_i p^2 + \gamma_i p^3, \qquad (2.2.10)$$

where p is measured along the straight line joining node $\underline{x}_i$ to $\underline{x}_{i+1}$ (see Figure 2.3). The cubic coefficients α_i, β_i, γ_i are calculated by insisting on continuity of curvature at each end of the section. The curvature at a node is computed by passing a circle through the node and its two neighbouring nodes.

Thus the velocity contribution for node k from the section on contour j starting at node i is (in the rigid lid case)

$$d\underline{u}_i(x_k,y_k) = (2\pi)^{-1}(\Omega_j - Sh_{Bj})\int_{\underline{x}_i}^{\underline{x}_{i+1}} \log r_k \, d\underline{x}_0, \qquad (2.2.11)$$

where $r_k^2 = (x_k - x_0)^2 + (y_k - y_0)^2$ and

$$x_0 = x_i + pa_i - \eta^*(p)b_i \quad ; \quad y_0 = y_i + pb_i + \eta^*(p)a_i,$$

where $(a_i,b_i) = (x_{i+1} - x_i,\ y_{i+1} - y_i)$. Rewriting in terms of p,

$$d\underline{u}_i(x_k,y_k) = (2\pi)^{-1}(\Omega_j - Sh_{Bj})\int_0^1 \log\left[\left(x_k - (x_i + pa_i - \eta^*(p)b_i)\right)^2 + \left(y_k - (y_i + pb_i + \eta^*(p)a_i)\right)^2\right]^{1/2}\left\{a_i - \frac{d\eta^*}{dp}b_i, b_i + \frac{d\eta}{dp}a_i\right\}dp.$$

For the rigid lid case, the above may be expanded for small η^* and the integral consisting of the first two terms solved exactly (see Dritschel (1988)). For the free

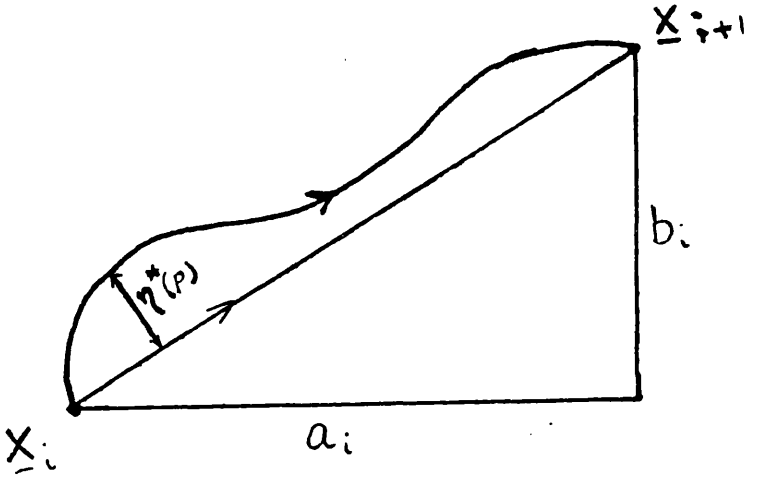

Figure 2.3

An internodal contour section. The section between node $\underline{x}_i = (x_i, y_i)$ and node $\underline{x}_{i+1} = (x_{i+1}, y_{i+1})$ is shown. The straight line joining the two nodes is given by (a_i, b_i) and p, varying between 0 and 1, is measured along this line. The cubic by which the contour section is approximated is given by $\eta^*(p)$.

surface case and for the case in Chapter 5, wherein the fact that the flow is in a channel leads to a more complicated Green's function in spite of the rigid lid approximation, the corresponding integrals must be evaluated numerically. This is done using the Lobatto approximation (see Abramowitz & Stegun). In this case several "sub-nodes" along the cubic are used. The integrand is evaluated at each sub-node and the weighted results are added.

If the node in question, node k, lies at one end of the section along which the integral is being evaluated, i.e $k = i$ or $k = i + 1$, as will occur twice for each node, the singularity in the integrand is dealt with by approximating the contour-section by a straight line and the integrand by a simple log in all cases, and by evaluating the integral exactly. This is, in general, the largest contribution to the nodal velocity.

In this way the velocities at all nodes are calculated. The new nodal positions are then computed from equation (2.2.9) by a 4th order Runge-Kutta scheme. Before the next set of velocities are calculated, however, the resolution must be checked. Stretches of contour with high curvature require a larger number of nodes to capture their evolution, which has led in the past to several renoding schemes based on the local curvature of the contour. However, as Dritschel (1988) points out, nodes near to regions of high curvature may also experience rapid change, although their local curvature may not necessarily be high. For this reason, Dritschel suggests a more complicated "node density function", which is a nonlocal function of curvature. It is this renoding scheme that is used throughout this thesis. The node density may be adjusted, i.e. the standard of the resolution may be set, by varying the parameters of the density function. Both the node density parameters and the timestep have been varied to check the contour dynamical results presented in this thesis.

Due to the cubic approximation to the contour and the

condition of continuity of curvature at the nodes, "corners" have to be inserted and removed along the contour if a discontinuity of curvature is required, as is the case in Chapter 5. Corners are inserted if the nodal angle becomes more acute than $\pi/2$. In this case the contour-sections adjacent to the corner node are approximated by straight lines. This surgical technique is due to Dritschel.

§2.3 Some simple examples.

In this section some simple flows containing particular points of interest are modelled using the contour dynamics method, to illustrate a sample of the range of problems for which the technique is suitable.

The first example demonstrates the way in which sources and sinks within a rotating fluid may be incorporated into the contour dynamical model. The simple but illustrative case of a flow containing one source and one sink is considered. The contour whose development is followed by the computation is the boundary of the fluid which enters at the source. This fluid has zero potential vorticity, originating from a non-rotating system, and therefore on entering a system which is rotating with speed f/2 it gains negative relative vorticity. Thus a patch of nonzero relative vorticity spreads outward from the source and it is the evolution of this patch which is traced by the calculation. As this patch approaches the sink, a cusp forms on the contour and clearly the flow contains a singularity, as the velocity at the sink is infinitely large. A truncation technique is demonstrated which allows the computation to continue in spite of this singularity.

The next question considered is the effect that a sidewall has on the development of a patch of relative vorticity. The presence of the wall may be modelled by the creation of an image patch containing vorticity of equal magnitude but opposite sign. The two FAVRs then translate in the manner of the vortex pairs described by Deem & Zabusky (1978) who find the class of pairs of FAVRs which translate uniformly without change of shape, i.e. the class of translating V-states. Their results apply to flows containing a wall and are extended by Pierrehumbert (1980) who considers the limiting case wherein the patch is actually touching the wall. In this work we restrict ourselves to this latter case, but

examine the development of a patch which is not of the steady shape found by Pierrehumbert. The initial shapes we consider are semi-ellipses of various aspect ratios, which are shown to lead to qualitatively different results.

The points of interest investigated in the first two examples are combined in the third, in which a flow containing both a source and a sidewall is modelled. Again the boundary of the growing patch of nonzero relative vorticity which emanates from the source is tracked, but in this case the competing effects of the radially-outward source flow and the advection by the image patch combine to produce a new and fascinating result.

§2.3.1 A source-sink flow.

We consider the flow relative to axes Oxy, with the source at the origin (0,0) and the sink at the point (1,0). By the equation of conservation of potential vorticity, equation (1.7), it is clear that the relative vorticity of the fluid as it enters at the source is given by

$$\zeta = -f. \qquad (2.3.1)$$

Nondimensionalising using the following scalings,

$$x' = Lx,\ y' = Ly,\ u' = Uu,\ v' = Uv,$$

where L is the distance between the source and the sink and UL is the inward flux at the source, and dropping the primes gives

$$\zeta = Ro^{-1}, \qquad (2.3.2)$$

where Ro = U/fL is a Rossby number for the flow.

Thus the evolution of the flow may be considered in terms of the relative importance of rotational and advective effects. If the Rossby number is large, advection dominates and the flow is similar to the non-rotating case. If the Rossby number is smaller, however, the effects of rotation are felt. In the absence of the sink the patch spreads radially from the source, remaining circular and rotating in a clockwise direction. The presence of the sink, however, causes the contour to deform as it rotates.

To incorporate the effects of the source and the sink into the contour dynamical model, their contributions to the nodal velocities are added after the contribution from the patch itself has been calculated. The velocities due to the source and sink are simply given by

$$u(x,y) = \frac{(x(1-x) + y^2)}{(x^2 + y^2)((x-1)^2 + y^2)}, \qquad (2.3.3a)$$

$$v(x,y) = \frac{y(1-x)}{(x^2 + y^2)((x-1)^2 + y^2)}. \qquad (2.3.3b)$$

The results are shown in Figure 2.4. In Figure 2.4(a) Ro = .5 The fluid spreads outward asymmetrically from the source and the contour develops a cusp as it approaches the sink. The effects of rotation are scarcely felt in this regime. The computation had to be terminated at this stage due to the singularity at the sink. In Figure 2.4(b) a truncation technique is illustrated which allows the computation to continue by distributing the sink. Nodes which are carried within a certain cut-off distance from the sink are repositioned at the cut-off distance. In Figure 2.4(b)(i) the cut-off distance is .2 and the first repositioning has been carried out, giving the

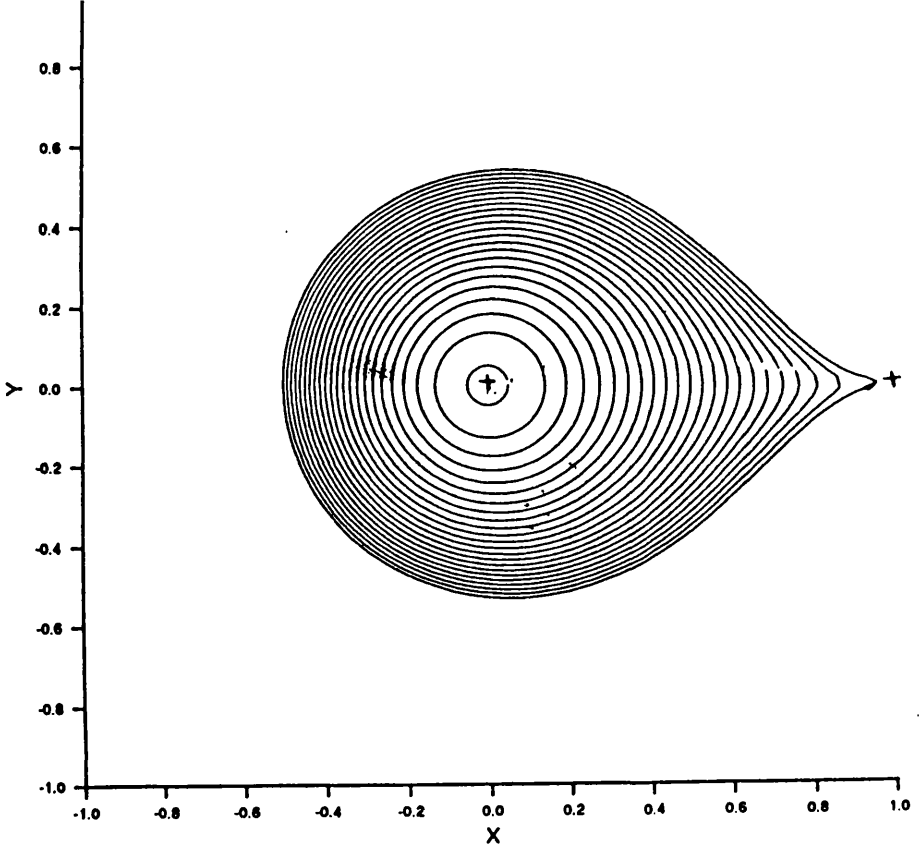

(a)

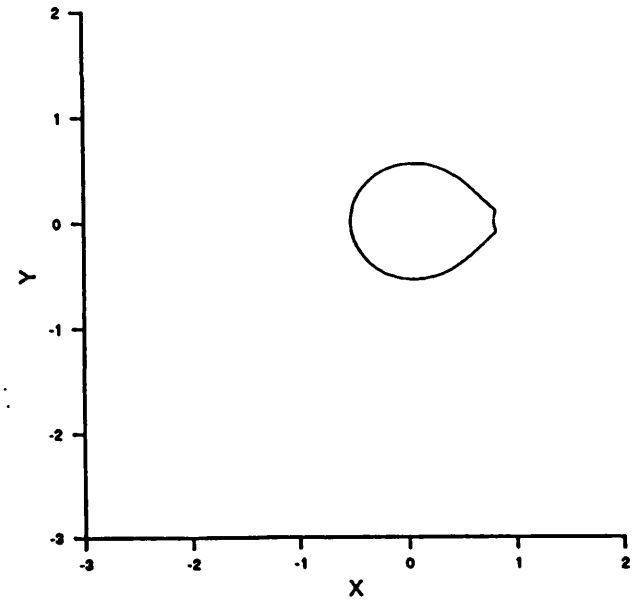

(b)(i)

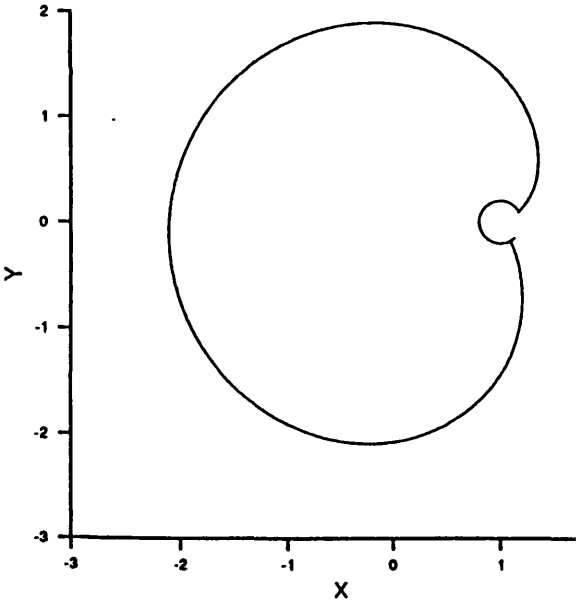

(b)(ii)

Figure 2.4

The source-sink results. (a) Ro = .5. A cusp forms on the contour along the x-axis as the patch approaches the sink at (1,0). (b) The contour is truncated when it is closer than .2 to the sink. (i) After the first repositioning. (ii) The contour surrounds the sink and continues to spread outward from the source.

contour a blunt appearance. Figure 2.4(b)(ii) shows the result at a later time. The contour has virtually encircled the sink, while the patch continues to spread slowly outwards from the source.

A smaller Rossby number is used in Figure 2.5, in an attempt to capture some rotational effects. Here Ro = .1. The cusp is no longer directed along the x-axis, but deflected by the clockwise rotation of the patch. Smaller values of the Rossby number are found to lead to instabilities along the contour, opening up a new line of investigation which is not pursued here.

§2.3.2 The effect of a sidewall.

In this subsection we extend the work of Pierrehumbert (1980) to consider the evolution of a semi-elliptical patch of relative vorticity adjacent to a sidewall, which is not a member of the class of uniformly translating V-states. The effect of the wall may be captured by the creation of an image patch of vorticity, of the same shape but containing vorticity of opposite sign. Thus in this problem the nodal velocities are calculated by integrating along two contours, bounding two regions of relative vorticity.

The results are shown in Figure 2.6. The aspect ratio of the initial semi-ellipse was taken first as 3, as shown in Figure 2.6(a). As the patch translates along the wall at y = 0 it is deformed as the upper part rotates in an anticlockwise direction. The patch remains attached to the wall at one point only and a lengthening thread joins this point to the main part of the patch which continues to rotate.

In Figure 2.6(b) the initial aspect ratio is 1/4 and a completely different development is shown. As the patch translates along the wall the fluid builds up in the front section. This shape of this section approaches that of the steady patch given by Pierrehumbert (1980),

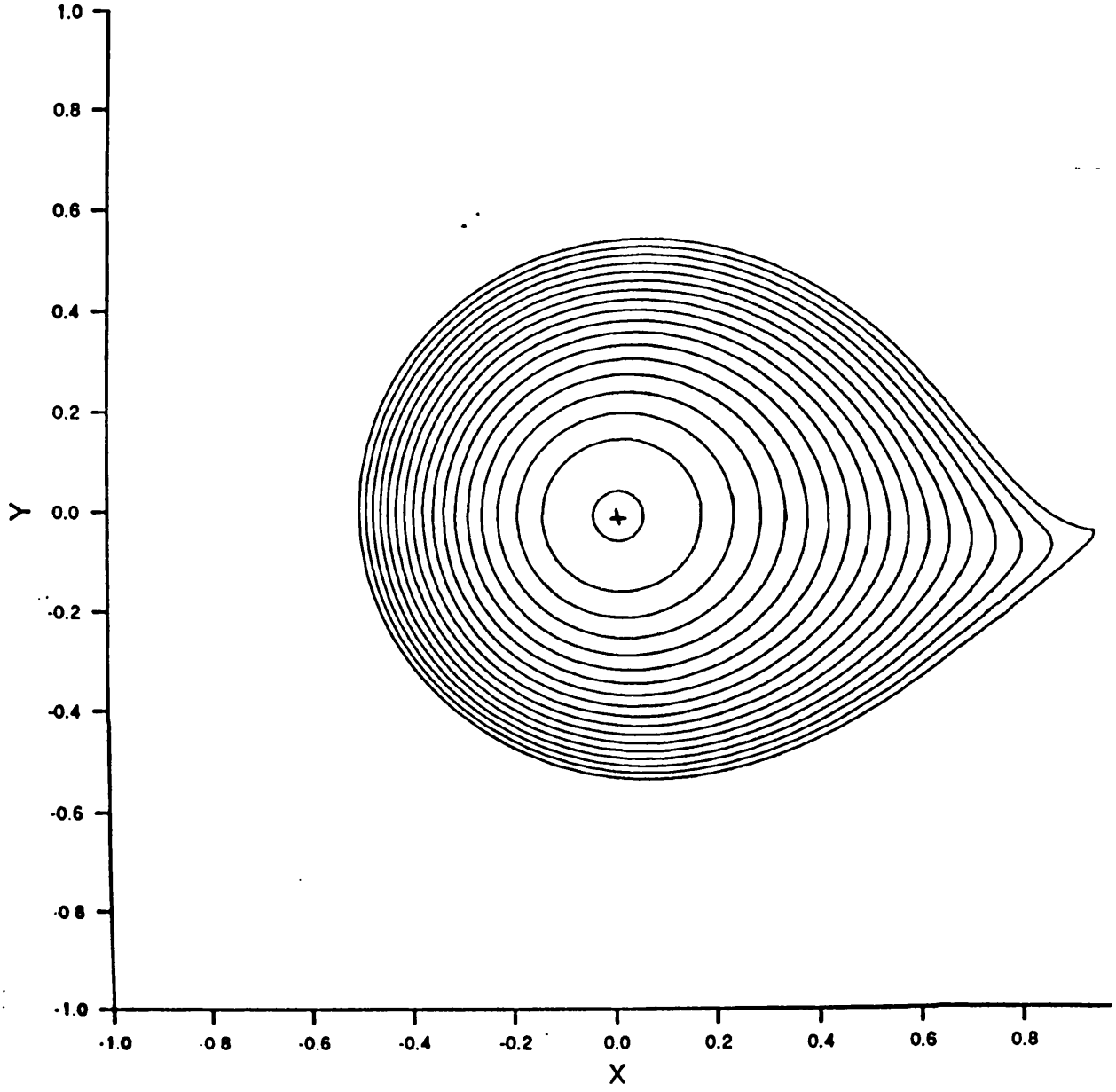

Figure 2.5

Ro = .1. The cusp no longer lies along the x-axis but is deflected by the clockwise rotation of the patch.

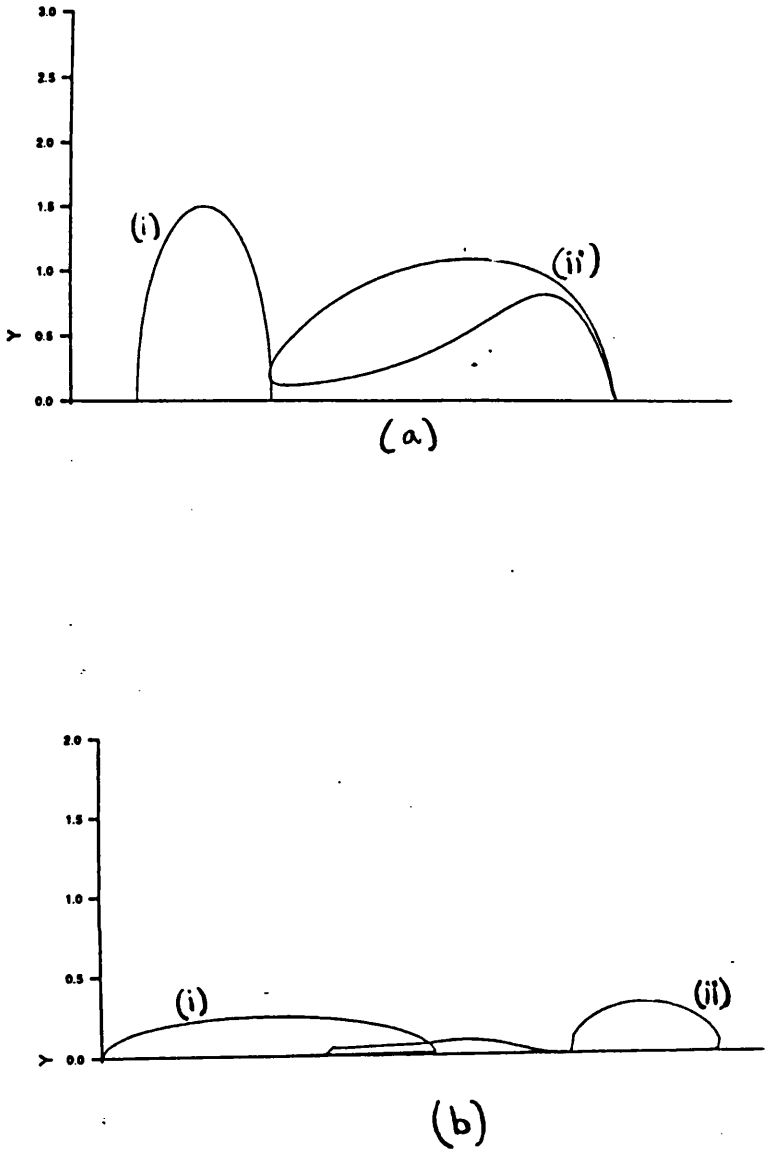

Figure 2.6

The results for a patch by a wall. (a) The initial aspect ratio is 3. The patch translates along the wall in the positive x-direction, rotating as it does so, and remaining attached to the wall by only a thinning thread. (b) The initial aspect ratio is .25. The front part of the patch develops into a shape close to that of the steadily translating patch, leaving a trail along the wall. This trail in turn builds up at the front.

leaving a narrow trail behind it. This trail in turn builds up at the front, suggesting that the patch divides itself into ever-smaller versions of the steadily translating case.

§2.3.3 A source at a wall.

The two previous examples are combined in this subsection. Here a flow containing a source at the origin (0,0) and a wall along the x-axis is modelled. As in §2.3.2 an image patch is created and the flow contribution due to the source is simply added as in §2.3.1. The result is shown in Figure 2.7. As the patch grows it begins to translate, in the negative x direction this time as the vorticity it contains is negative. Initially the patch is nearly semi-circular as the fluid first leaves the source. As it grows, however, an inward cusp develops towards the rear and the front forms into the steady shape given by Pierrehumbert (1980). At later times, as this shape moves off, a further build-up of fluid occurs and it appears that a stream of such steadily translating shapes is formed as the fluid continues to emanate from the source.

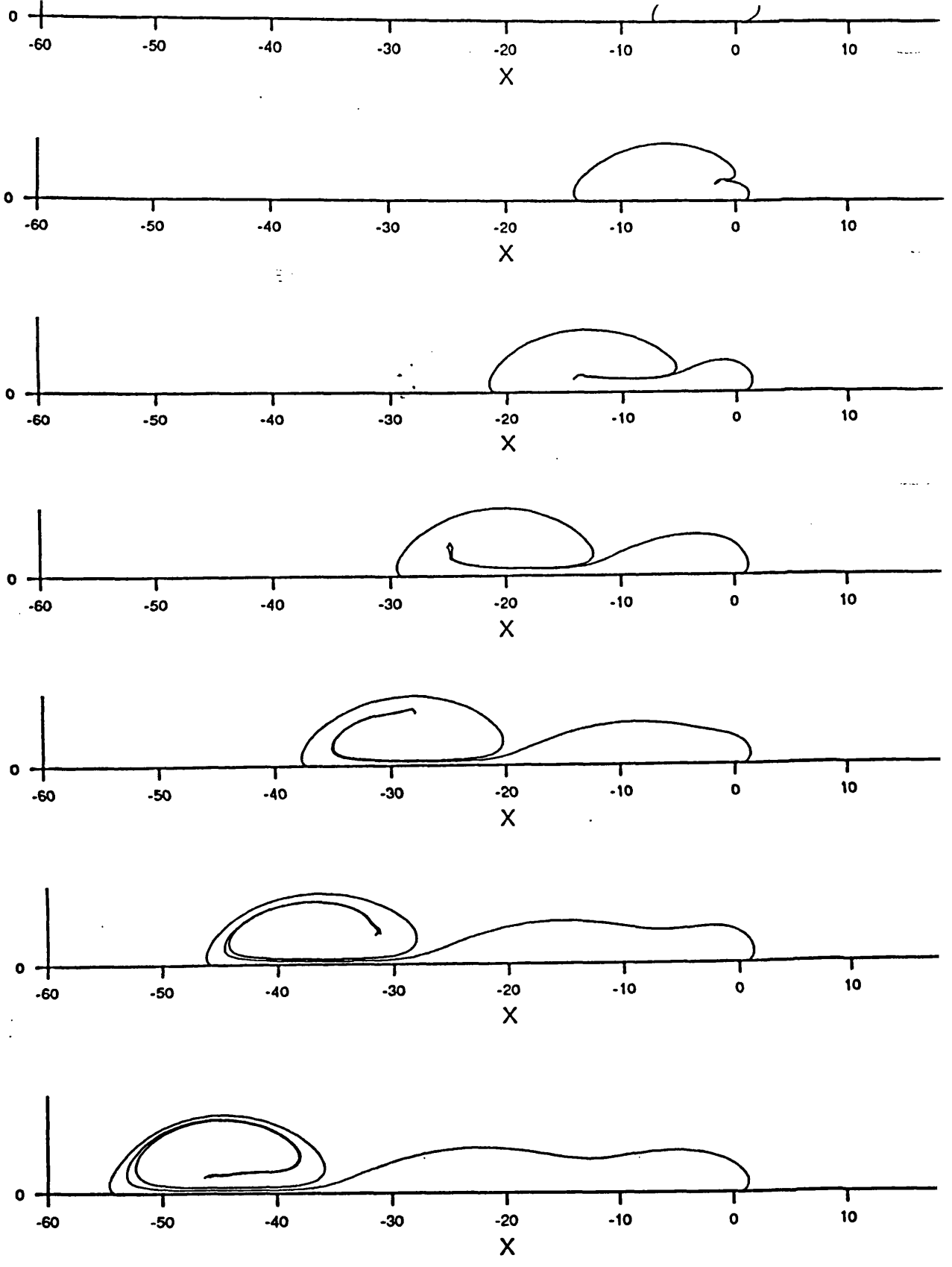

Figure 2.7

The source by a wall. The patch is initially semi-circular, but develops an inward cusp and separates into two regions, as it translates along the wall in the negative x-direction. The eddy to the left resembles the steadily translating shape, whilst behind this the fluid builds up again as more fluid leaves the source.

CHAPTER 3.

TOPOGRAPHIC GENERATION, TRAPPING AND CAPTURE OF FREE-SURFACE EDDIES

§3.1. Introduction.

In this chapter attention is focussed on the modifications to the uniform flow of a rapidly rotating fluid caused by an isolated, submerged, flat-topped cylindrical obstacle, with particular regard to free surface effects. As mentioned in Chapter 1, it was the experiments of Taylor (1923) which first demonstrated the "Taylor column", and thus initiated a great deal of investigation into this phenomenon. Jacobs (1964) gives a linear theory, in the limit of vanishing viscosity, necessary to obtain a unique steady solution, and finds the required stagnant region surrounded by two-dimensional flow. His results, however, do not show the asymmetry in the flow seen in the experiments of Hide & Ibbetson (1966). Ingersoll (1969) considers the nonlinear conservation of potential vorticity, obtaining a unique solution by formulating the problem with viscosity and then letting the viscosity tend to zero. He shows that fluid within a region of closed streamlines must be motionless due to Ekman pumping, and uses this extra condition to find steady solutions to the nonlinear problem in the geostrophic limit. He finds the shape and position of a stagnant region trapped above the cylinder and asymmetric flow outside this region, when the Hide parameter, $S = \delta/Ro$, exceeds some critical value. This value is found for arbitrary axisymmetric topography by Huppert (1975), for both the homogeneous and stratified cases, as a function of the shape of the topography.

The evolution of such a column from the starting flow is difficult to obtain due to the presence of the closed streamlines. Huppert & Bryan (1976) integrate numerically the nonlinear time-dependent equations of motion, for the stratified case, and find that for values of S exceeding the critical value the cyclonic vortex interacts with the anticyclonic vortex above the topography and remains in the vicinity of the obstacle. Possible steady positions

and shapes for such trapped cyclonic vortices are found by Johnson (1978a,b) by the use of both a variational principle and a gravitational analogy. The trapped vortex is considered further by James (1980), for a sloping axisymmetric obstacle. The nonlinear equations, including the effects of Ekman boundary layers, are integrated numerically and in particular the drag and lift forces found. It is shown that the drag force is initially larger for the case of the partially trapped vortex and that it oscillates as the highly deformed vortex cycles the topography, finally dying away as the trapped vortex is spun up by Ekman pumping.

Johnson (1984) considers the initial-value problem analytically by introducing the topographic vortex-stretching timescale, i.e. the time taken for a topographic wave (see Chapter 1) to cycle around the obstacle. The vortex-stretching time is taken to be long compared with the inertial period and short compared with the advection time. The resulting viscous equations are then solved for the case of axisymmetric obstacles, using the Laplace transform. The results for a right circular cylinder show a topographic Rossby wave cycling clockwise around the obstacle, decaying on the viscous spin-up time or continuing indefinitely in the absence of viscosity. The drag and lift show the decaying oscillations of the numerical computations of James (1980).

In this chapter we assume the ratio of the topographic to advective timescales, S, to be order unity. Information is carried through a combination of topographic wave propagation and particle advection, with the resulting effect that the region of fluid originally above the obstacle becomes deformed, in agreement with James (1980). In some cases part of this fluid remains trapped above the obstacle, pinched off from the rest which is advected away downstream.

An important aspect of this chapter is the inclusion of free surface effects. These effects become significant over scales greater than or of the order of the Rossby

radius of deformation, $a = (g'H)^{1/2}/f$, where H is the undisturbed depth of the fluid, f is twice the background rotation rate and g′ is gravitational acceleration. The fluid may be regarded as two-layered, in which case g′ is the modified gravitational acceleration, and we consider the evolution of the lower layer, with an infinitely deep, passive upper layer. This is in contrast to the "equivalent barotropic" case of Polvani, Zabusky & Flierl (1989), who consider an infinitely deep, passive lower layer. In both cases, however, the governing equation in the active layer is the Helmholtz equation and comparisons may be drawn in the results.

If the modified gravitational acceleration is used, the Rossby radius of deformation is greatly reduced, which leads to the basic difference in the flow, due to the free surface. This lies in the decay of vortex influence - algebraic in flows with the rigid lid approximation but exponential in the free surface case. Hence the influence of a patch of vorticity is far more localised in the free surface case.

The inviscid nonlinear problem is integrated numerically using contour dynamics. As mentioned in Chapter 2, the use of contour dynamics in an investigation of the generation of vortices in a uniform flow over a cylindrical underwater obstacle was first carried out by Kozlov (1983), who points out the possibility of some fluid remaining above the obstacle. His work is extended here to consider both sheared oncoming flow and the effect of a free surface, and hence the dependence of the flow evolution on the Rossby radius of deformation.

Section 3.2 gives the equations of motion and a brief description of the necessary modifications to the contour dynamics method. The computation was carried out for various parameter values and §3.3 discusses the resulting generation of vortices. Several figures are shown, illustrating the various regimes: the cyclonic vortex is shown in "fast" cases where it is swept downstream and

"slow" cases where it remains partially covering the topography, becoming highly stretched. It is shown that as the Rossby radius decreases the fluid is more likely to be swept downstream. This behaviour is investigated by examining the varying contribution to the flow from the topography as the Rossby radius is altered. An analytical approximation to the path of the shed vortex in the "fast" case is shown to agree well with the numerical results.

Section 3.4 considers first the trapping of fluid originally above the topography, which is shown to occur for sufficiently large values of S. Secondly, the possibility of the capture of fluid initially upstream of the topography is examined, under the assumption that all fluid initially over the topography has been swept off. The interaction of an initially upstream vortex with the topography is modelled and it is shown that fluid may be captured in this way, for sufficiently large values of S, provided that the upstream vortex is negative, i.e. has the same sign as the topographic vortex with which it interacts. If the upstream vortex is positive, the two vortices behave in a similar way to the translating vortex pairs of Deem & Zabusky (1978) and the free vortex is carried around the obstacle before being advected away downstream. The path of the oncoming vortex is again predicted analytically.

In §3.5 the problem is extended to examine the case of an oncoming shear flow. The method used is unchanged, and the main difference seen in the results is that two cyclonic vortices are now shed. The nonlinear steady problem is considered analytically by Johnson (1983) for both positive and negative oncoming shears, under the assumption that some fluid originating over the obstacle is retained there, an assumption which is shown here to be justified. The steady flow with negative shear is found by Johnson to be set up on the advective timescale, and consists of an elliptical stagnant Taylor column, elongated across the stream, partially covering the

topography, surrounded by constant potential vorticity flow. There are no closed streamlines outside the stagnant region, thus the Ingersoll (1969) criterion (that, in the limit of vanishing viscosity, fluid within closed streamlines is spun up by Ekman pumping) is not expected to alter the flow on the longer viscous timescale. For flows with positive shear the Taylor column is again found by Johnson to be elliptical, this time extended in the streamwise direction. In this case, however, there are closed streamlines outside the column and therefore it is expected that on the viscous timescale the flow would be significantly altered by Ekman pumping. For both positive and negative shears the current numerical results agree well with the steady solutions of Johnson (1983), thus in this case the contour dynamics method enables us to see the complete development of a flow from rest to its final steady state. The paths of the shed vortices are again calculated.

Section 3.6 summarises the results and suggests future work.

§3.2.The governing equations and modifications to the contour dynamics method.

The governing equation is the geostrophic equation for conservation of potential vorticity, equation (1.7), which may be linearised as in Chapter 2 to give equation (2.2.6).

For a flat-topped obstacle and initially irrotational flow the initial potential vorticity distribution is given by

$$\Omega = \begin{cases} S & \text{above the topography} \\ 0 & \text{away from the topography} \end{cases} . \qquad (3.2.1)$$

Consider a cylindrical obstacle, radius L (i.e. nondimensional radius 1) as shown (dashed) in Figure 3.1. When oncoming flow with zero potential vorticity is introduced each fluid particle is advected downstream and two non-zero vorticity areas are produced, as some fluid moves up onto the obstacle and some moves off. These areas are labelled A_1 and A_2 respectively in Figure 3.1(a). As δ, the fractional height of the obstacle, is small, the size of the two areas is the same, and they contain vorticity of equal magnitude but opposite sign. Neither the fluid contained in area A_3 nor that in area A_4 have gained or lost any vorticity. Thus the flow is determined by the contributions from A_1 and A_2 together with the uniform oncoming stream. The contribution from A_1 is given by :

$$\nabla^2\Psi - \Psi/a^2 = -S, \qquad (3.2.2)$$

where *a* is the nondimensional Rossby radius of deformation, scaled on L. Similarly the contribution from the second area is given by:

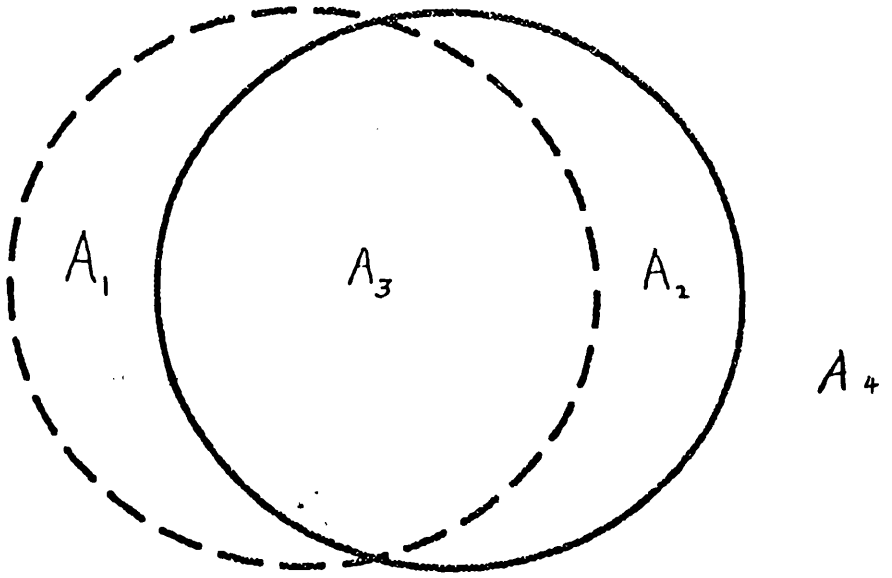

(a)

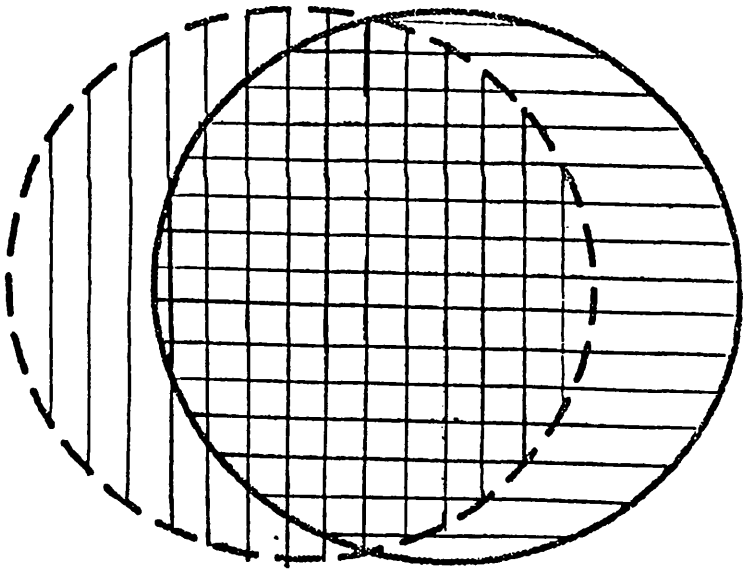

(b)

Figure 3.1.

(a)The various regions of the flow. In area A1 fluid has moved onto the obstacle, in area A2 fluid has moved off, in A3 it has remained on and in A4 it has remained off. (b)The topographic contour bounds the region of vertical shading and the advected contour bounds that of horizontal shading.

$$\nabla^2\Psi - \Psi/a^2 = S, \qquad (3.2.3)$$

Thus, as mentioned in Chapter 2, the stream function is given by:

$$\Psi(x,y)=\sum_{j=1,2}\frac{\Omega_j}{2\pi}\iint_{A_j} K_0\left[\frac{1}{a}\sqrt{(x-x_0)^2+(y-y_0)^2}\right]dx_0dy_0, \qquad (3.2.4)$$

where $\Omega_j = \pm S$ and K_0 is the zeroth order modified Bessel function, which is the Green's function for equations (3.2.2) and (3.2.3). Thus the effect of allowing a free surface, i.e. a finite Rossby radius, is to alter the Green's function from being logarithmic to being exponential. The velocities are given by:

$$u(x,y)=\sum_{j=1,2}\frac{\Omega_j}{2\pi}\int_{\partial A_j} K_0\left[\frac{1}{a}\sqrt{(x-x_0)^2+(y-y_0)^2}\right]dx_0, \qquad (3.2.5a)$$

$$v(x,y)=\sum_{j=1,2}\frac{\Omega_j}{2\pi}\int_{\partial A_j} K_0\left[\frac{1}{a}\sqrt{(x-x_0)^2+(y-y_0)^2}\right]dy_0, \qquad (3.2.5b)$$

where ∂A_j is the boundary of the region A_j. Thus the problem of determining the flow field is reduced to evaluating the line integrals (3.2.5). However, integrating around ∂A_1 and ∂A_2 and adding the result is equivalent to integrating around the edge of the topography, shaded vertically in Figure 3.1(b), and around the curve bounding the region of fluid originally over the topography, shaded horizontally. The first of these curves, the so-called "topographic contour", is fixed and the contribution from it can be calculated analytically. The second curve, the "advected contour", is a material line and its contribution must be computed numerically.

The topographic contribution follows from direct solution of (3.2.2) as:

$$\Psi(r) = S\begin{cases} a^2 - aI_0(r/a)K_1(1/a) & r < 1 \\ aI_1(1/a)K_0(r/a) & r > 1 \end{cases}, \qquad (3.2.6)$$

where r is the distance from the centre of the topography. Thus the velocity contribution from this contour is:

$$(u,v) = S/r\begin{cases} I_1(r/a)\ K_1(1/a)\ (-y,x) & r < 1 \\ I_1(1/a)\ K_1(r/a)\ (-y,x) & r > 1 \end{cases}. \qquad (3.2.7)$$

The contribution from the advected contour is found numerically by calculating the integrals given in equation (3.2.5). In this case, as described in Chapter 2, the integrand is evaluated using the Lobatto formula. Again the contour is split into small sections and the contributions from each section calculated separately. Renoding is used throughout to maintain resolution. The contribution to the velocity from the uniform stream is then added. The velocity at every node along the advected contour is calculated in this way. It is then moved accordingly and the new velocities calculated.

§3.3.Generation of eddies.

§3.3.1 The analytical solution for fast flows.

For sufficiently strong oncoming flows or sufficiently low obstacles, i.e. for small values of S, all fluid above the obstacle is swept off downstream. The resulting vorticity distribution is steady and given by equation (3.2.7). An anticyclonic vortex occurs above the obstacle, constantly being replenished by new fluid. The nondimensional surface displacement due to this topographic vortex is axisymmetric and given by

$$\eta(r) = S^{-1}\Psi(r)/a^2, \qquad (3.3.1)$$

where Ψ is given by equation (3.2.6). This is shown in Figure 3.2(a) for a = 0.1, 1.0 and 10.0. The latter is clearly similar to the rigid lid case, $a \to \infty$, where the surface cannot deform at all. Hence blocking is more likely in this case than in the other limit, $a \to 0$, in which the surface deforms to a shape very similar to the step profile, and fluid is not inhibited from passing over the topography. For sufficiently small a, $a \sim Ro \ll 1$, three-dimensional effects become important. As the vorticity produced by compression of the fluid filaments is determined entirely by the local depth, the topographically generated vorticity is uniform for the rigid lid case, but non-uniform for finite values of a when the amount by which the filaments are compressed varies with position. The relative vorticity, ζ, is given by

$$\zeta = v_x - u_y = S/a \begin{cases} I_0(r/a)\, K_1(1/a) & r < 1 \\ I_1(1/a)\, K_0(r/a) & r > 1 \end{cases}, \qquad (3.3.2)$$

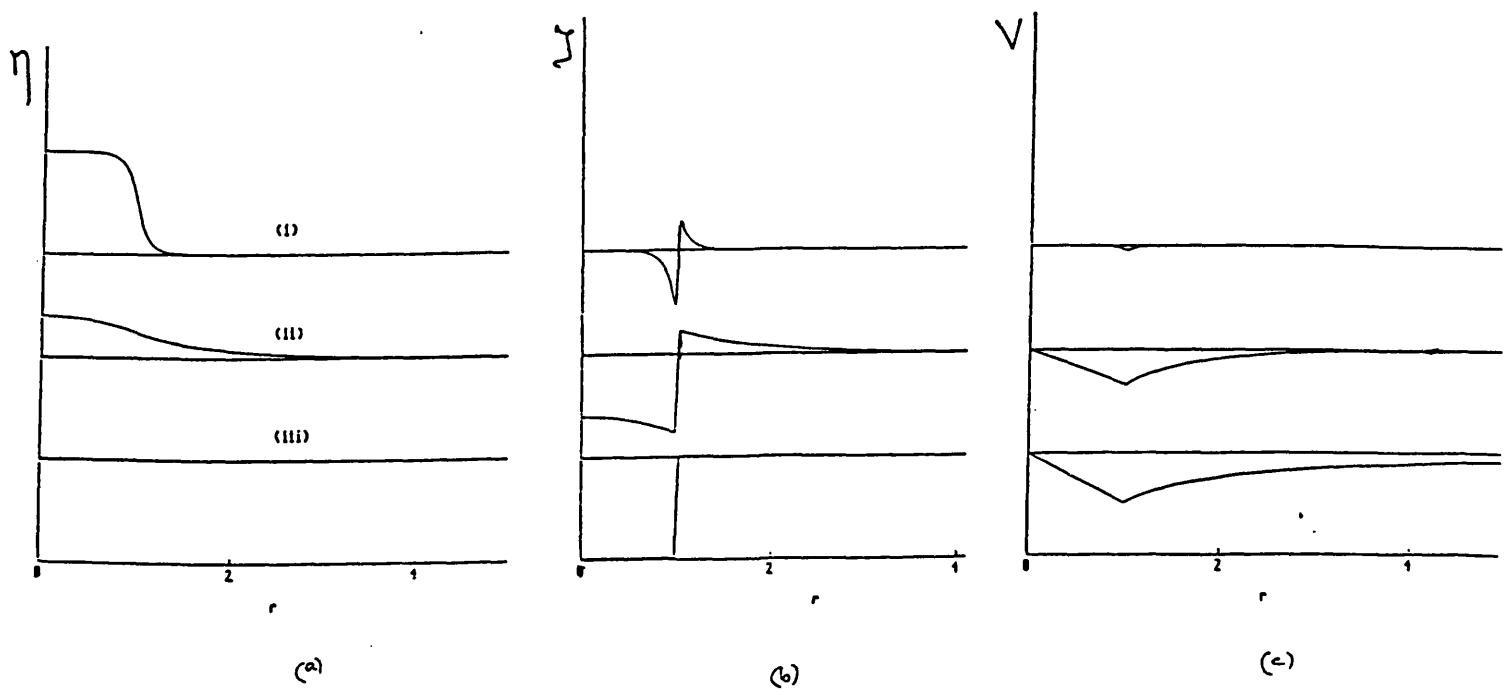

Figure 3.2.

The fast case. (a) The topographically-induced surface displacement, η, for (i) a = .1 (ii) a = 1. and (iii) a = 10. The surface deforms over the length a. (b) The topographically-induced vorticity, ζ, for values of a as in (a). For the rigid lid case the distribution is uniform , for finite values of a the vorticity is mainly at the edge of the step, i.e. at r = 1. (c) The topographically-induced velocity, V, for values of a as in (a). As a decreases the velocity is confined to an ever-thinning region at the edge.

and is shown in Figure 3.2(b). As a decreases the vorticity is confined to a thin region around the edge of the obstacle, where the initial compression takes place. The effect of this non-uniform vorticity distribution is seen in Figure 3.2(c), which shows the topographically-induced velocity in the azimuthal direction, given by equation (3.2.7) to be

$$V(r) = S\begin{cases} I_1(r/a)\, K_1(1/a) & r < 1 \\ I_1(1/a)\, K_1(r/a) & r > 1 \end{cases}. \qquad (3.3.3)$$

As $a \to \infty$ this becomes

$$V(r) = S\begin{cases} r/2 & r < 1 \\ 1/2r & r > 1 \end{cases}. \qquad (3.3.4)$$

Thus in the rigid lid case the fluid rotates as a solid body for $r < 1$, but decreasing the value of a causes the fluid to become virtually stagnant near the origin, the velocity being confined to a thin layer about $r = 1$, as is shown by considering equation (3.3.3) as $a \to 0$:

$$V(r) = S\ a/2\ e^{-|r-1|/a}\ r^{-1/2}. \qquad (3.3.5)$$

Far upstream the flow is taken to be parallel with zero potential vorticity. Thus the streamfunction upstream satisfies

$$\Psi_{yy} - \Psi/a^2 = 0, \qquad (3.3.6)$$

and hence the upstream velocity field can be written in general as

$$U_0 = -\Psi_y = U \cosh(y/a) + \beta a \sinh(y/a). \qquad (3.3.7)$$

The first term in (3.3.7) gives symmetric flow with centre-line velocity U, increasing exponentially on the scale of the Rossby radius. In the rigid lid limit this corresponds to a uniform stream. The second term in (3.3.7) gives antisymmetric flow with shear rate β on the centre-line. In the rigid lid limit this gives a linearly sheared flow. The present section discusses in detail symmetric flow with $\beta = 0$. Flow with $\beta \neq 0$ is discussed in §3.5.

Thus with U normalised to be unity, and $\beta = 0$, the total stream-function is given by

$$\Phi(r,\theta) = -a \sinh (r\sin\theta/a) + \Psi(r,\theta), \qquad (3.3.8)$$

where r, θ are polar coordinates centred on the topography. From equation (3.3.3) a stagnation point appears in symmetric flow first with increasing obstacle height at $r = 1$, $\theta = -\frac{\pi}{2}$, when S exceeds S_c, where

$$S_c = \frac{\cosh(1/a)}{I_1(1/a)\ K_1(1/a)}. \qquad (3.3.9)$$

Figure 3.3 includes S_c as a function of $1/a$. As the Rossby radius decreases the critical value for S increases towards $1/a\ e^{1/a}$. As the Rossby radius increases the critical value for S decreases towards 2. This is the value for the rigid lid, single-layer case given by Huppert (1975).

§3.3.2 Numerical results.

The numerical computation was carried out for both the rigid lid case and for two finite values of the Rossby radius, a=1 and a=1/2. The relevant points in parameter

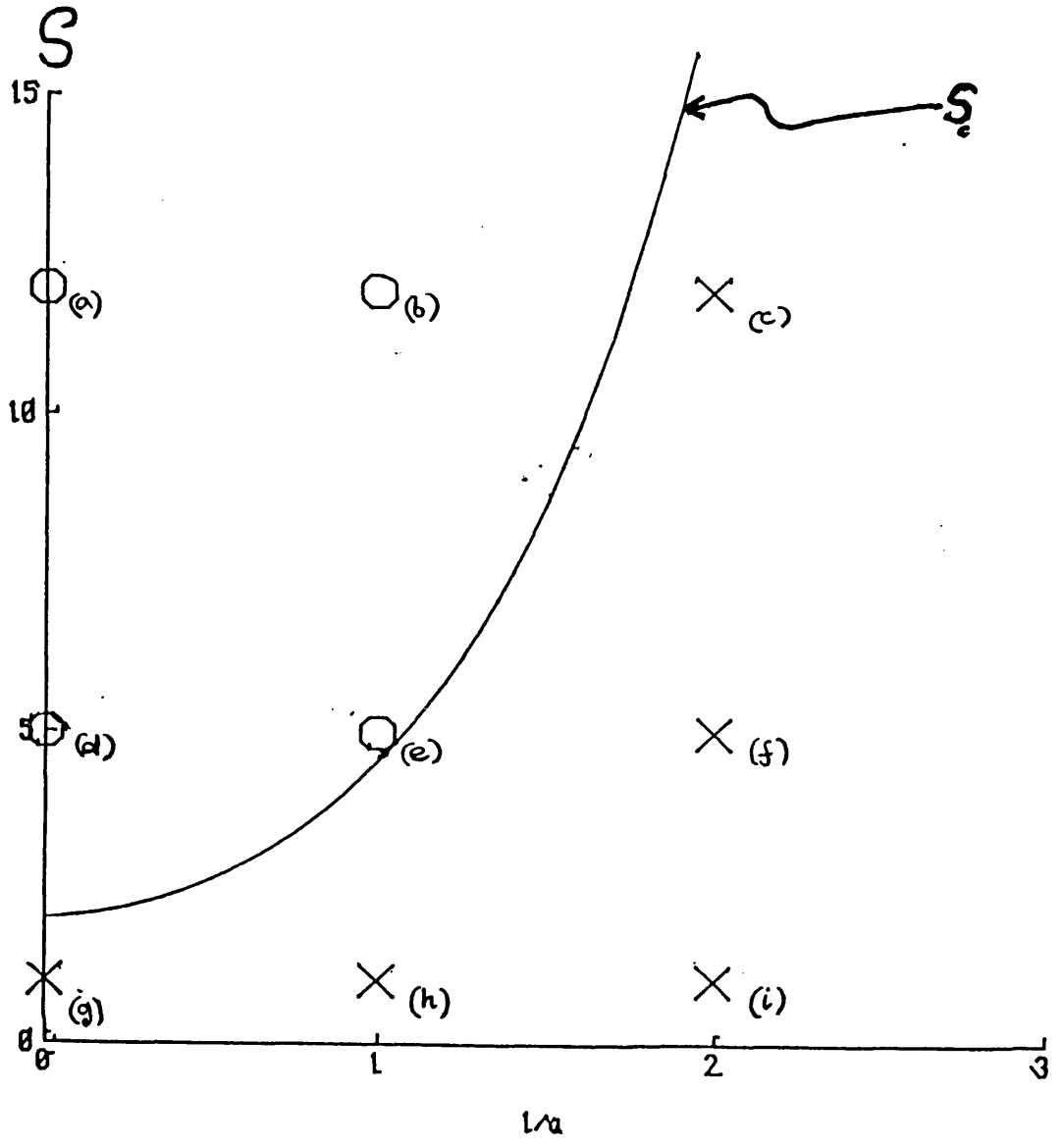

Figure 3.3.

The analytical critical curve for the parameter δ/Ro, as a function of the inverse Rossby radius, and the points in parameter space corresponding to the numerical experiments carried out. The circles are at (0,12);(1,12);(0,5);(1,5) and represent the cases in which trapping occurs. The crosses are at (2,12);(2,5);(0,1);(1,1);(2,1) and represent the cases in which trapping does not occur.

space are indicated on Figure 3.3 by circles (representing cases where fluid was trapped) and crosses (representing cases where no fluid was trapped), the values of S being 1, 5 and 12. The results are shown in Figure 3.4.

There several points of interest in this figure. Firstly, for values of S below the critical values given in Figure 3.3, all the fluid is swept downstream, with no stagnation points in the flow. Above the topography an anticyclonic vortex is formed, and a cyclonic vortex is advected downstream with a velocity tending to that of the uniform stream. The path of this shed vortex is considered in more detail later. For values of S above the critical value, some fluid remains over the obstacle. The stagnation point argument is no longer strictly valid, as there is no longer a completely circular vortex above the topography, and there is some cyclonic vorticity in the vicinity. However the pictures do indicate the presence of stagnation points and blocking and the earlier argument can be taken as an approximate guide to the evolution of the flow. As S is increased, the topographic effect is heightened, more fluid is held back over the obstacle and a larger blocked region formed. This region is considered in more detail in the next section.

Secondly, the effect of the Rossby radius is shown. For the same value of S, flows with a smaller Rossby radius are less likely to be blocked. For each value of S there is a critical value of the Rossby radius below which blocking will not occur. As seen in Figure 3.2(a), the adjustment of the free surface due to the step at r = 1 takes place over a length scale of the order of the Rossby radius. Thus as *a* decreases this adjustment occurs over a shorter distance, the surface deformation is greater and the fluid can pass more easily over the topography. Figure 3.4 clearly illustrates this: for smaller values of *a*, with S held constant, the topography is seen to have less effect on the advected contour. The

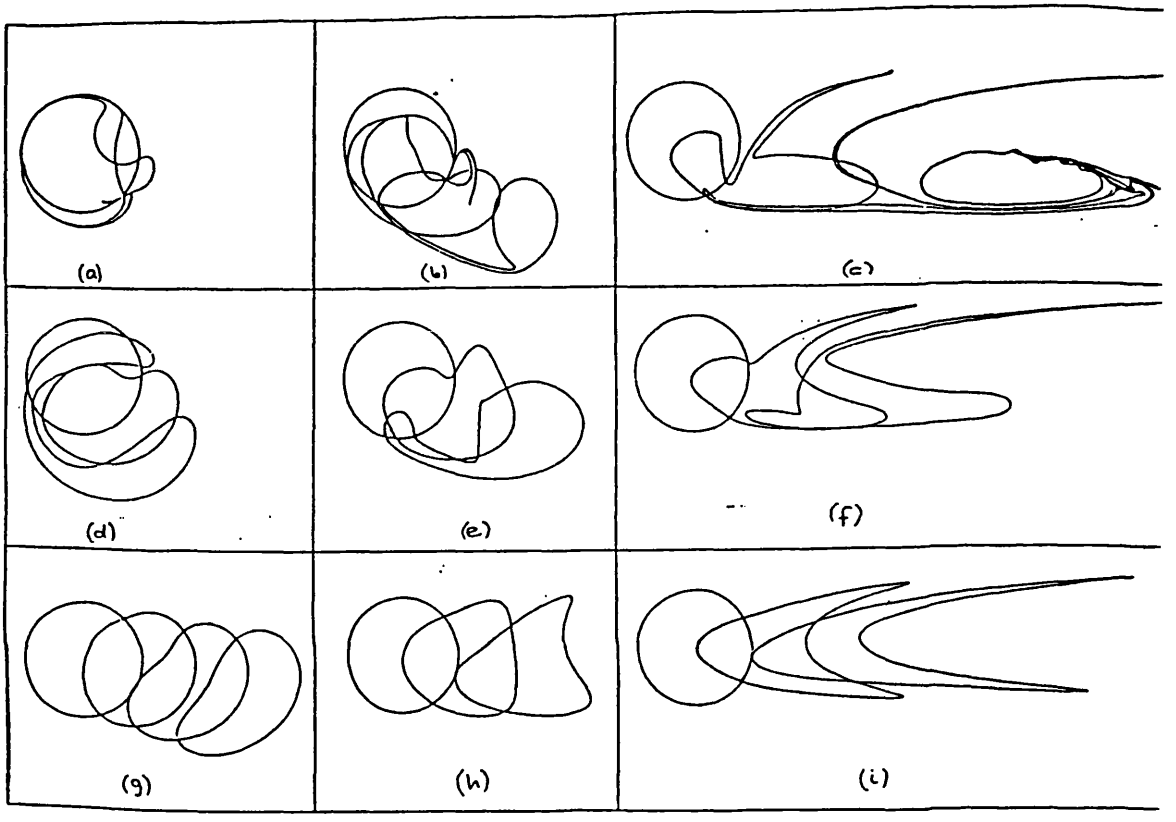

Figure 3.4.

The results for the parameter values marked in Figure 3.3. As δ/Ro increases the topographic effect increases as seen by comparing 3.4(g) and 3.4(a). As the Rossby radius decreases the topographic effect decreases as is seen by comparing 3.4(d) and 3.4(f). For values of δ/Ro above the critical curve in Figure 3.3, it is seen that fluid is trapped above the topography, while for values below the critical value the fluid is advected downstream. The time interval is 1., except in 3.4(c) which has t = 0, 1., 2.5.

restriction of the velocity to a thin layer around r = 1 for smaller values of *a* can also be seen in Figure 3.4: as *a* decreases the topographic wave front, where the boundary of the advected contour crosses the step (e.g. in Fig.3.4(b)), decays exponentially away from r = 1, while in the rigid lid case the decay is algebraic.

§3.3.3 The path of the shed vortex.

Now consider the path taken by the cyclonic vortex in the case where all the fluid originally over the topography is advected downstream. Huppert & Bryan (1976) approximate the path by representing the cyclonic vortex as a point, advected initially from the origin to the position (1,0), and the topographic vortex as a point at the origin. They consider the path of a such a region, shed in a similar way, for both the stratified and homogeneous cases with a rigid lid. The equivalent result for the free-surface case can be found in the same way. The path of the point is given by

$$2a\sinh(Y/a) - SK_0\left(\frac{1}{a}\sqrt{X^2 + Y^2}\right) = -SK_0(1/a). \qquad (3.3.10)$$

For the rigid lid case this reduces to

$$X^2 + Y^2 = e^{-4Y}, \qquad (3.3.11)$$

for S = 1, as found by Huppert & Bryan and this is plotted (dashed) in Figure 3.5(a), together with the contour dynamics results. The solution of equation (3.3.10), for *a* = 1 and again S = 1, is plotted in Figure 3.5(b) together with the relevant contour dynamics results. Again the more localised effect of the finite *a* case is seen: the topographically generated velocity decays exponentially away from the cylinder in contrast

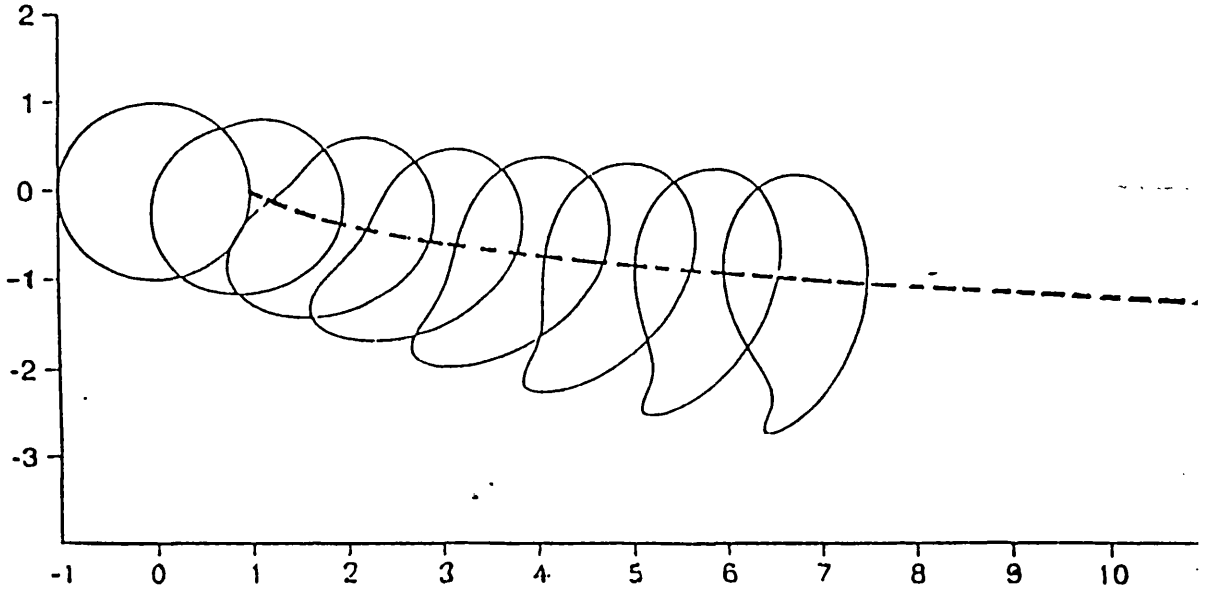

(a)

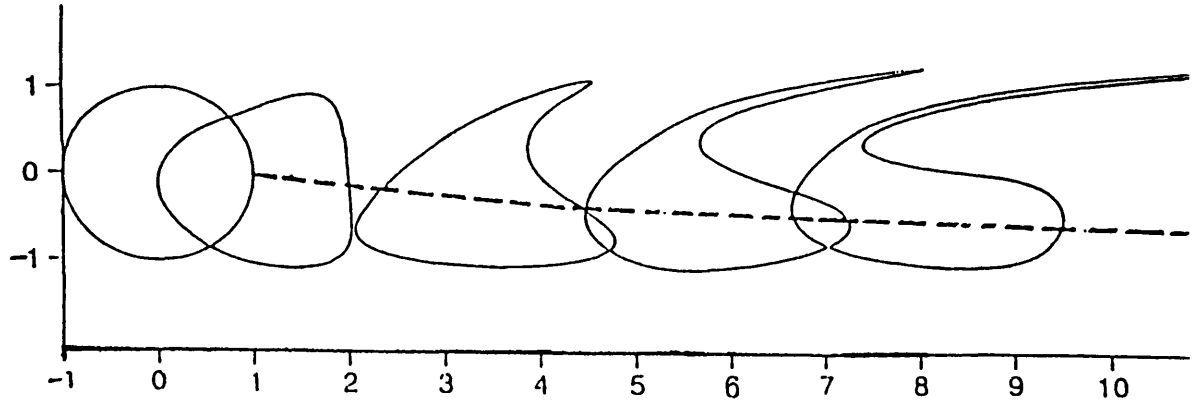

(b)

Figure 3.5.

The path of the advected contour in the fast case. The vortices are shown at times from 0 to 7.(a) The rigid lid case, as found by Huppert & Bryan (1976). Here $\delta/Ro = 1$ as in Figure 3.4(g). The path tends algebraically to that of the uniform stream. (b) a = 1, as in Figure 3.4(h). The path tends exponentially to that of the uniform stream.

with the algebriac decay in the rigid lid case.

§3.4.Trapping and capture.

§3.4.1 Trapping.

In considering the flow in the case where some fluid which is originally over the topography remains trapped there, it is helpful to look again at the flow due to a purely anticyclonic region above the topography together with the oncoming uniform stream. The streamlines for this zero potential vorticity flow are shown in Figure 3.6(a), for S = 5 and a = 1, i.e. the case shown in Figure 3.4(e). The region of closed streamlines indicates the expected position of any trapped fluid. If a small amount of fluid were trapped in this region the streamlines would be very similar to those shown and it is unlikely that the fluid would subsequently escape.

Figure 3.6(b) shows the flow of Figure 3.4(e) at longer times, i.e. at t = 3, 4, 5, and it is clear that, although most of the advected region is carried downstream, a fraction of it is trapped above the topography. By t = 5 the part which has moved off downstream is virtually unaffected by the topography due to the localisation effect of the finite Rossby radius and similarly this part has little effect on the flow over the topography. The remainder still lies trapped in the closed streamline region, with a shape and position similar to those found by Ingersoll (1969) for the rigid lid case.

§3.4.2 Capture.

In this section the possibility of originally upstream fluid being captured over the topography is considered. It is assumed that the fluid originally over the topography has been swept off already, by a previous episode of fast flow, so the flow is initially the zero

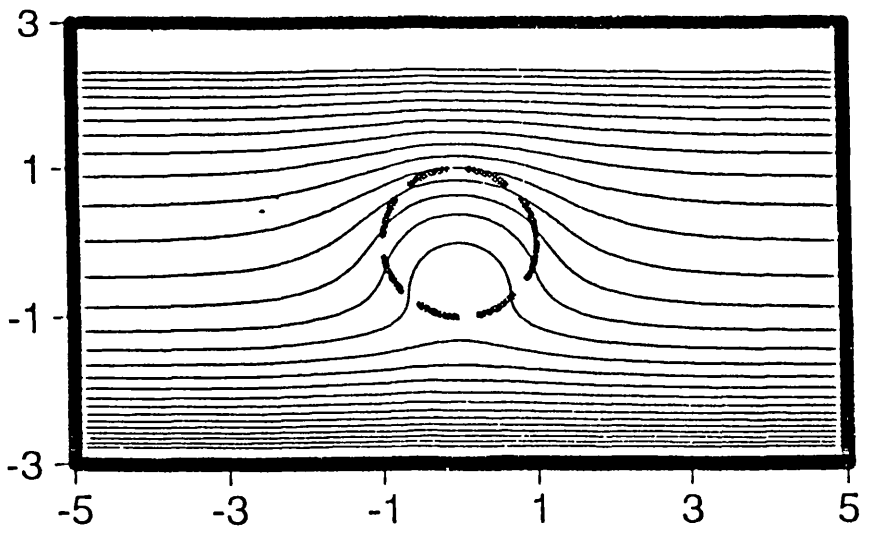

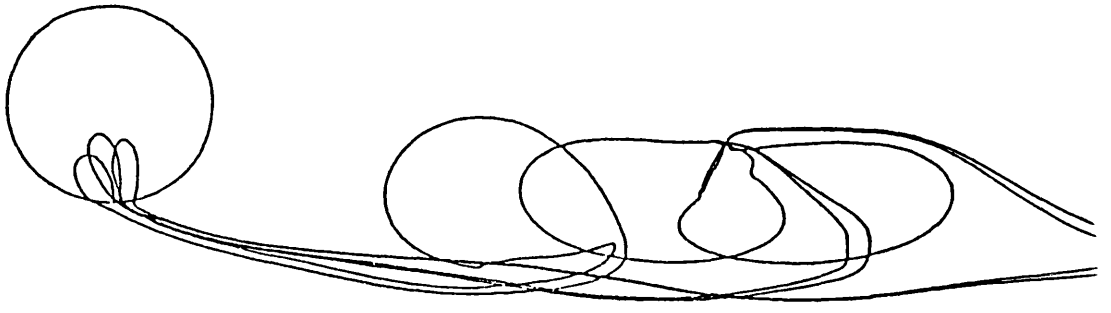

Figure 3.6.
The trapping of fluid originally over the obstacle. (a) The zero potential vorticity flow, which acts as a guide. Here $\delta/Ro = 5.$ and $a = 1$, i.e. the case shown in Figure 3.4(e). (b) The case in Figure 3.4(e) at $t = 3, 4, 5$.

potential vorticity flow considered in the previous section. This flow is further illustrated in Figure 3.7, for (a) the rigid lid case and (b) a = 1. In both cases S = 12. The more local effect of the finite Rossby radius case is immediately apparent. In both pictures there are regions of closed streamlines, within which fluid may be captured.

An upstream vortex is now introduced, of the same magnitude as the topographic vortex. In Figure 3.8 the rigid lid limit is used, the upstream vortex is positive and S is taken as (a) 12 and (b) 5. The dashed line indicates the path of the upstream vortex, which is predicted by the method used in the previous section. As the vortex is advected by the uniform stream the combined effect of the anticyclonic vortex above the obstacle and this moving vortex is to carry the latter around the topography, the overall deflection to its path being to the right looking downstream. This effect is quite easily understood: as the moving vortex approaches the topography the vortices act in a similar way to the vortex pairs considered by Deem and Zabusky (1978) and Pierrehumbert (1980), in which it is shown that a pair of vortices of equal magnitude and opposite sign will translate together along a straight line perpendicular to the line joining their centres. Steady shapes of such translating pairs are found and, as mentioned in §2.1, recent work by Polvani, Zabusky and Flierl (1989) shows that as the Rossby radius decreases these shapes become more circular, and the velocity with which they translate decreases, reflecting the fact that each vortex is influenced less by the other due to the finite Rossby radius localisation effect. In this instance, the topographic vortex is fixed, and so the moving vortex is constrained to describe an arc around the topography, until it is advected away by the oncoming stream. For a smaller value of S, the interaction between the two vortices is weaker and the free vortex is deflected less by the topography, as shown in Figure 3.8(b).

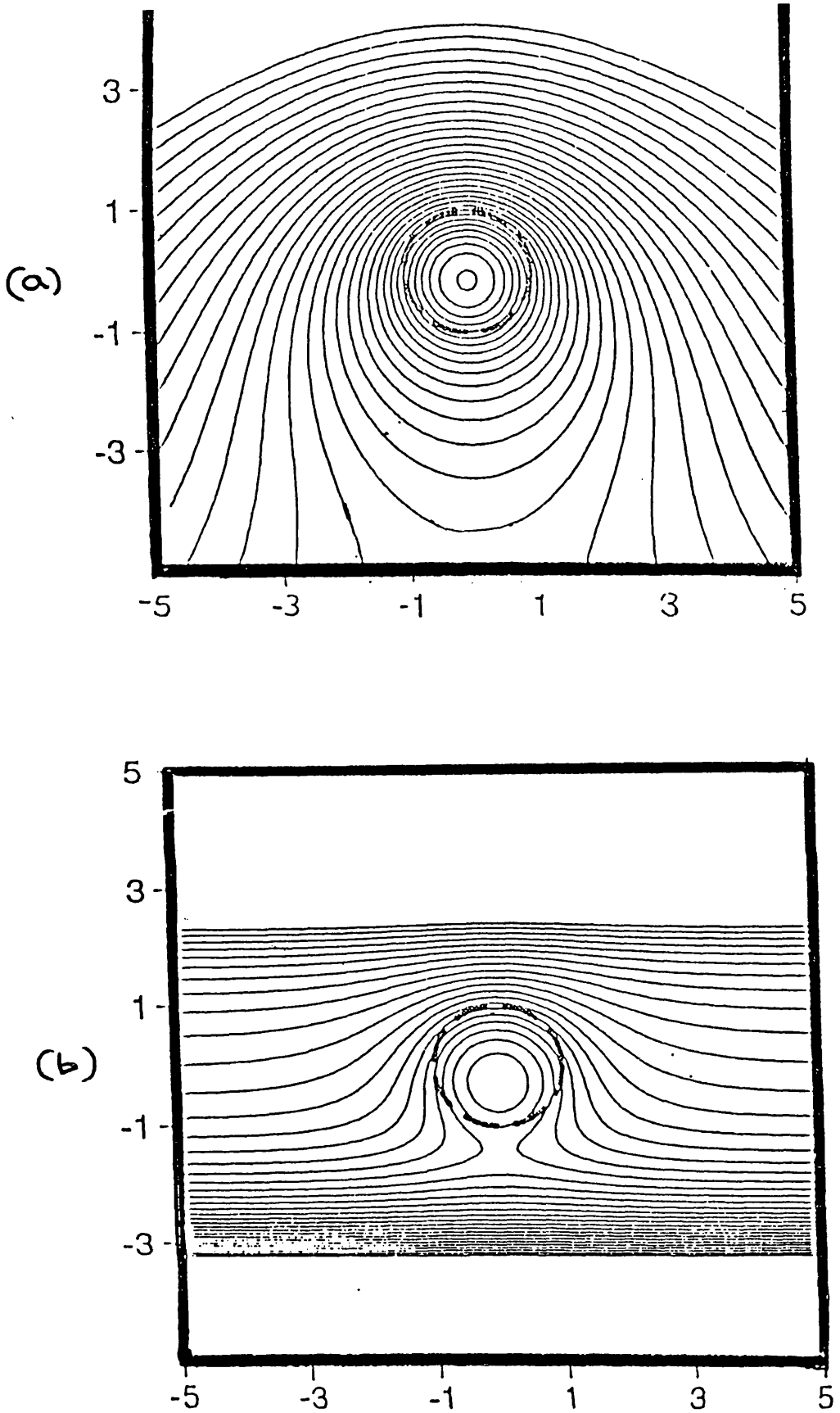

Figure 3.7.

The zero potential vorticity flow for (a) the rigid lid case and (b) $a = 1$. In both pictures $\delta/Ro = 12$. The region of closed streamlines is clear.

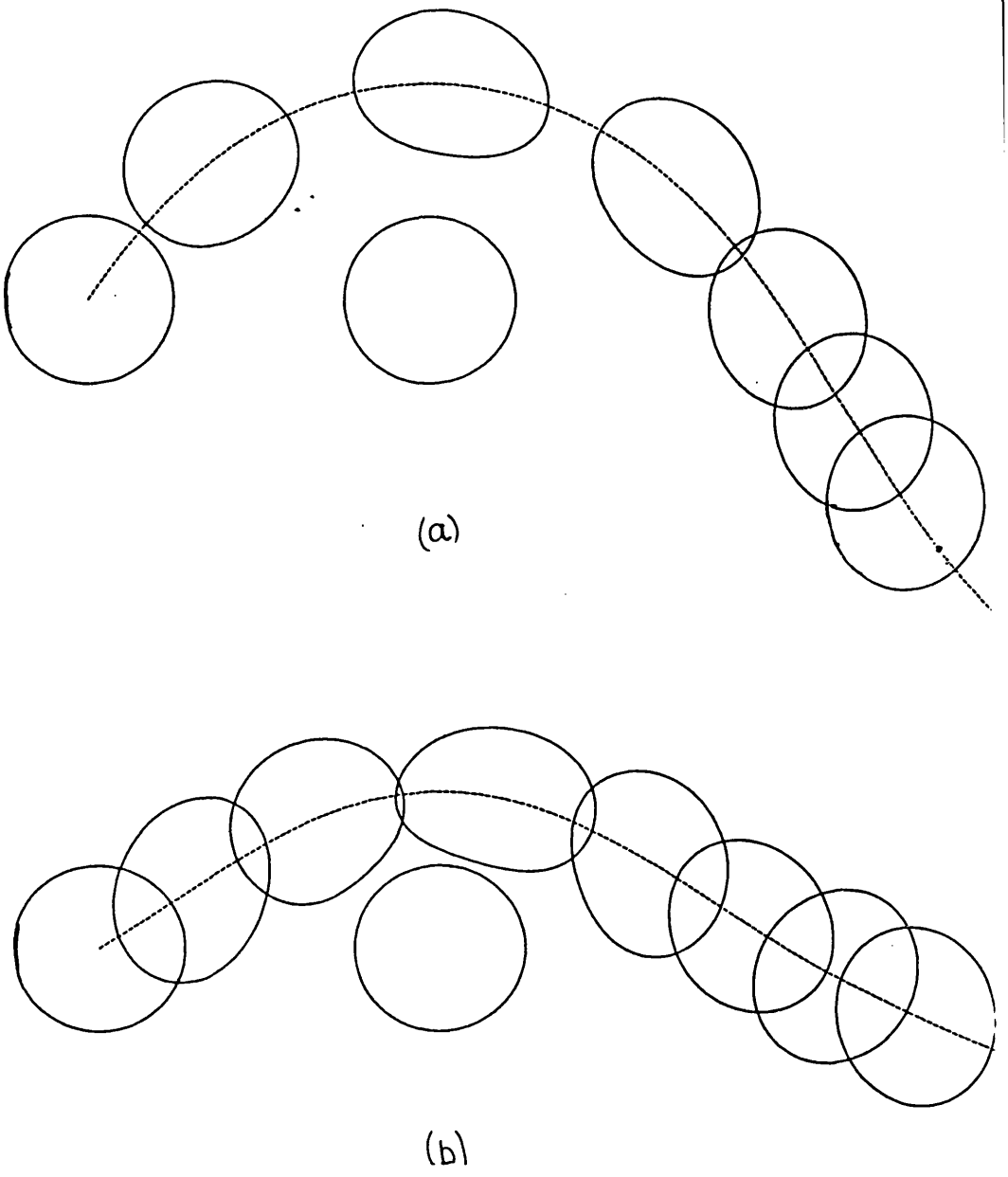

Figure 3.8.
The interaction between the zero potential vorticity flow and an upstream cyclone in the rigid lid case. (a) δ/Ro = 12. (b) δ/Ro = 5.

If the upstream vortex has the same sign as the topographic vortex, however, the result is quite different. This is illustrated in Figure 3.9, again using the rigid lid limit. In Figure 3.9(a) S = 12. The moving vortex is initially carried clockwise around the topography as in the previous case. Unlike the previous case, however, part of the anticyclonic moving vortex is drawn in over the obstacle, then quickly spirals in towards the centre, while the rest is advected away. Clearly in this case some fluid will be captured. A larger fraction of the oncoming vortex is captured for a lower value of S. In Figure 3.9(b) S = 5. The effect of the topography is weakened and the oncoming vortex is not pulled as rapidly around the obstacle as it is in the previous case. This allows more fluid to be pulled in onto the topography and captured.

Further experiments reveal that no fluid is captured by a topographic vortex of strength below S_c, irrespective of the strength of the oncoming vortex. This implies that a larger value of S is required to capture upstream fluid for finite values of *a*.

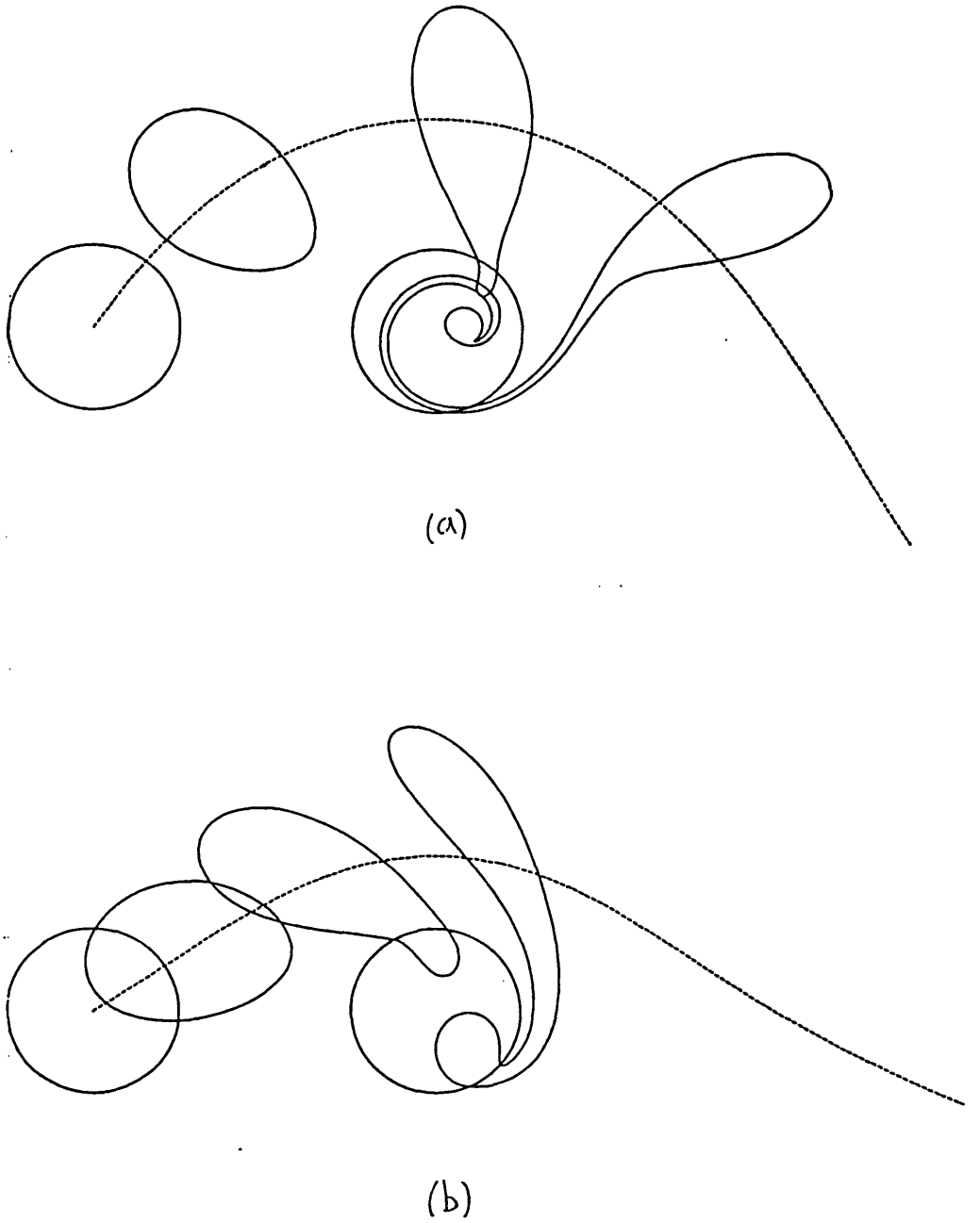

Figure 3.9.
The interaction between the zero potential vorticity flow and an upstream anticyclone in the rigid lid case. (a) $\delta/Ro = 12$. (b) $\delta/Ro = 5$.

§3.5. Oncoming shear flows.

Consider now the antisymmetric velocity profile so U = 0 in equation (3.3.7). Then the total stream-function can be written

$$\Phi(r,\theta) = -\beta a^2 \cosh(y/a) + \Psi(r,\theta), \qquad (3.5.1)$$

where S is taken to be unity. The flows for both positive and negative values for the shear parameter β are considered, for both the rigid lid limit and with finite values of a. The former results are compared with the steady states found by Johnson (1983).

In the rigid lid limit ($a \to \infty$), omitting the constant, equation (3.5.1) becomes

$$\Phi(r,\theta) = -\beta y^2/2 + \Psi(r,\theta). \qquad (3.5.2)$$

The computation was carried out first for this case, with negative shear, β = -.3, corresponding to the case in Figure 2(b) of Johnson (1983). In this case the background shear is opposing the shear induced by the topography. The results are shown in Figure 3.10. In Figure 3.10(a), at time t = 1, the flow is dominated by the shear. Two regions of positive vorticity are created by fluid being swept off the obstacle, and as this fluid is replaced two regions of negative vorticity are produced above the topography. In Figure 3.10(b), at t = 8, as these four regions grow their own influence increases, and the flow development depends on these four regions together with the background shear. Topographic wave fronts are visible, moving clockwise around the edge of the obstacle, and at t = 28, Figure 3.10(c), the shed regions are pinched off from the trapped fluid, connected by an ever-thinning thread. The influence of these shed

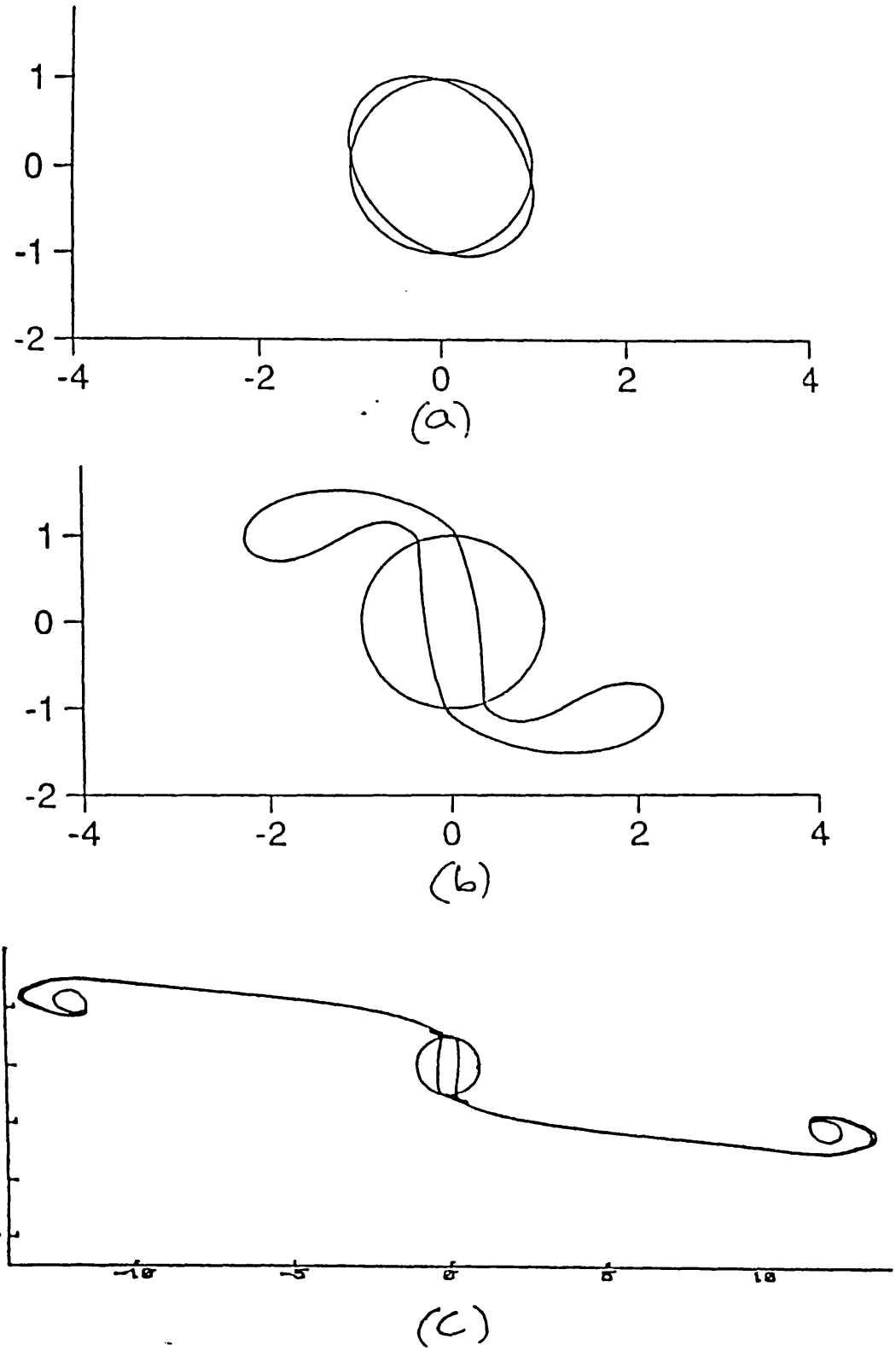

Figure 3.10.
Flow with negative shear, β = -.3, for the rigid lid case, for (a) t = 1 (b) t = 8 and (c)t = 28.

regions begins to fade as they are advected away by the shear, and another, much smaller pair is shed. The process is repeated, and it is clear that eventually a balance is reached between the shear and the anticyclonic vortex regions above the obstacle, the final position of the trapped region being that given by Johnson (1983).

The path of the shed vortices may be found by the method used in §3.3. The shed vortices are approximated by points, initially at $(0,\pm 1)$. In this case, contributions to their velocities come from the topography, the ellipse above the topography, the shear flow, and the other shed vortex. The problem is simplified by its symmetry: the shed vortices have position $(\pm x,\mp y)$, so the velocity contributions from each other can simply be added to that from the topography. Further, it is clearly only necessary to calculate the path of one of the vortices. The contribution from the ellipse is given by Johnson (1983), and the shear flow is simply added. The approximate paths are shown (dashed) in Figure 3.11, together with the contour dynamics results for $t = 30$. The paths become more accurate as $(x^2 + y^2) \to \infty$, and by $t = 30$ the vortices have begun to follow them.

The results for the free surface case are seen in Figure 3.12 at (a) $t = 1$, (b) $t = 3$, (c) $t = 8$. Here $\beta = -.3$ again but now $a = 1/3$. The topographic wave front is sharper than that of Figure 3.10, and the shear itself is stronger. The effect is that much less fluid is trapped over the obstacle than in the rigid lid case, and the paths of the shed regions again tend very quickly to the direction of the shear, as the influence of the topography dies away exponentially.

Next the computation was carried out for $\beta = .2$, corresponding to the case in Figure 3(c) in Johnson (1983). Now the background shear is in the same direction as that due to the topography. The rigid lid results are shown in Figure 3.13 at (a) $t = 1$, (b) $t = 8$, (c) $t = 24$. As in the negative shear case four regions of new vorticity are set up and some fluid is trapped above the

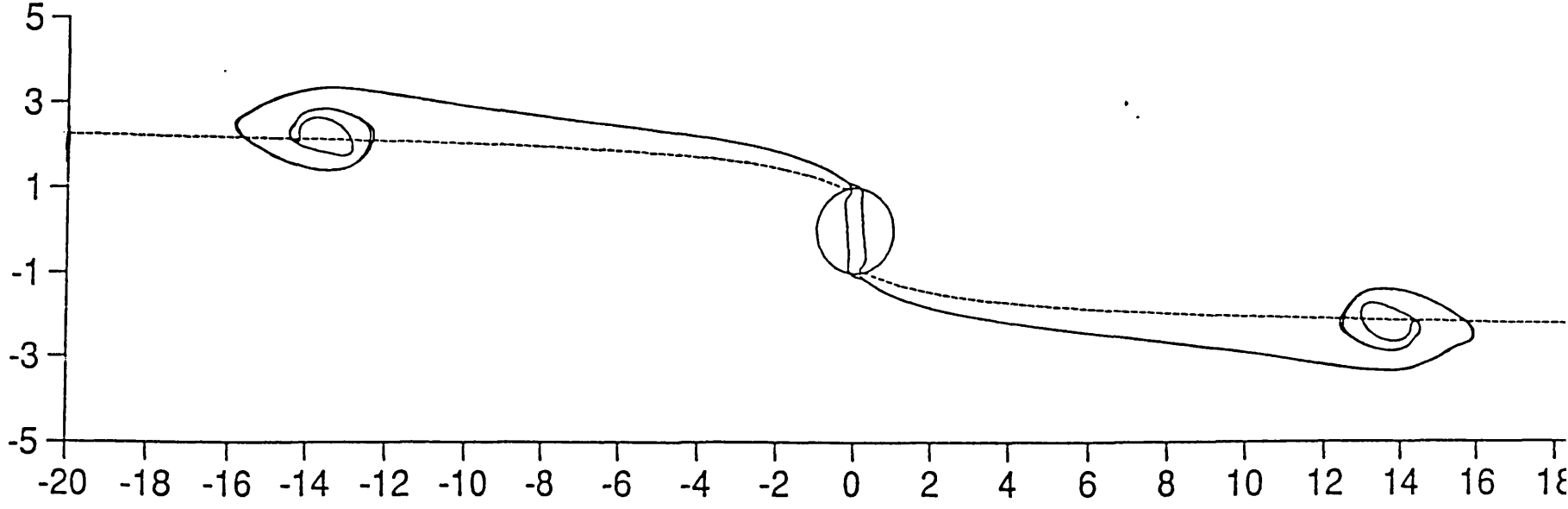

Figure 3.11.

The paths of the shed regions. The vortices are shown at t = 30.

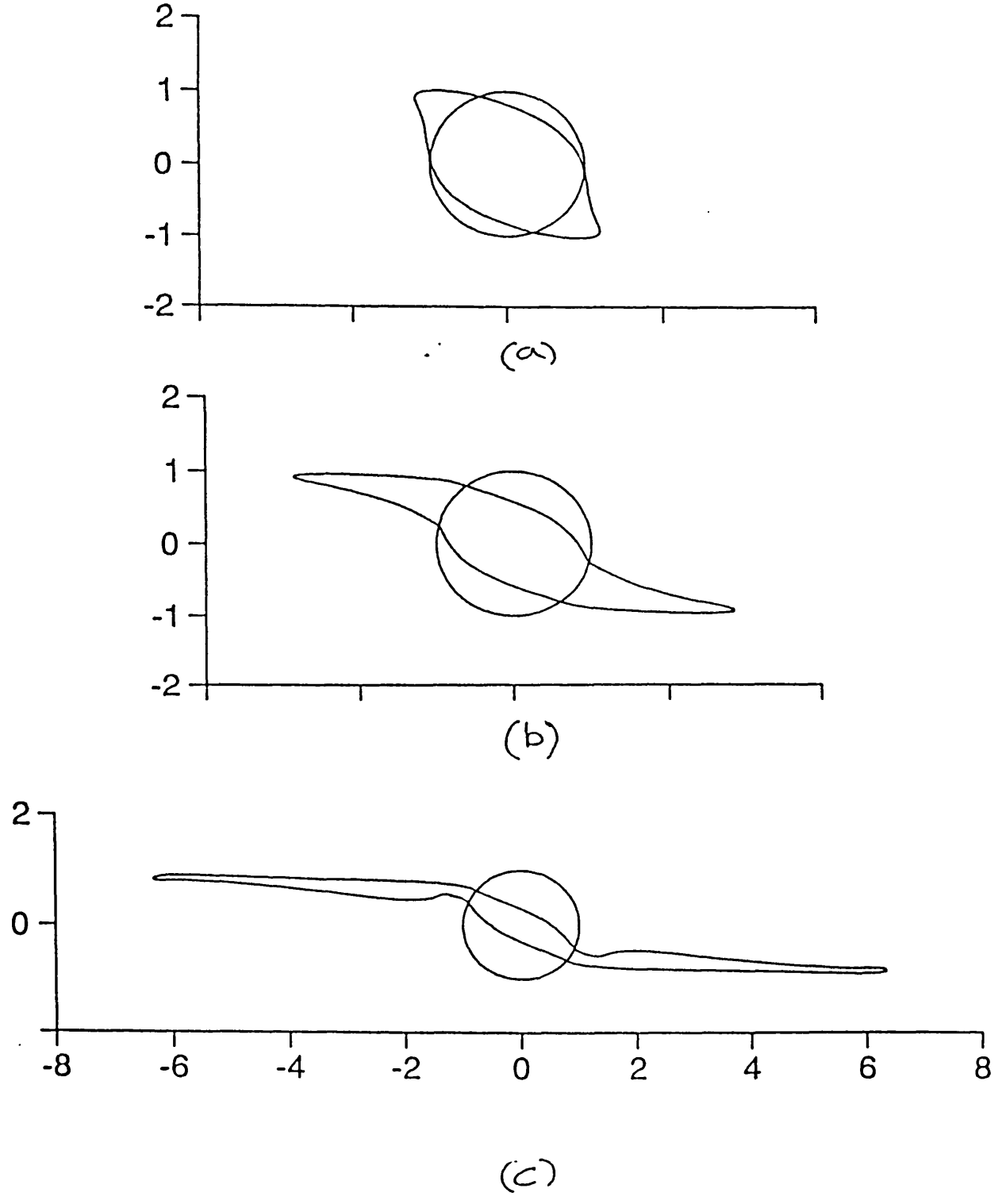

Figure 3.12.
The effect of a free surface on flow with negative shear, $\beta = -.3$, $a = 1/3$, for (a) $t = 1$ (b) $t = 3$ (c) $t = 8$.

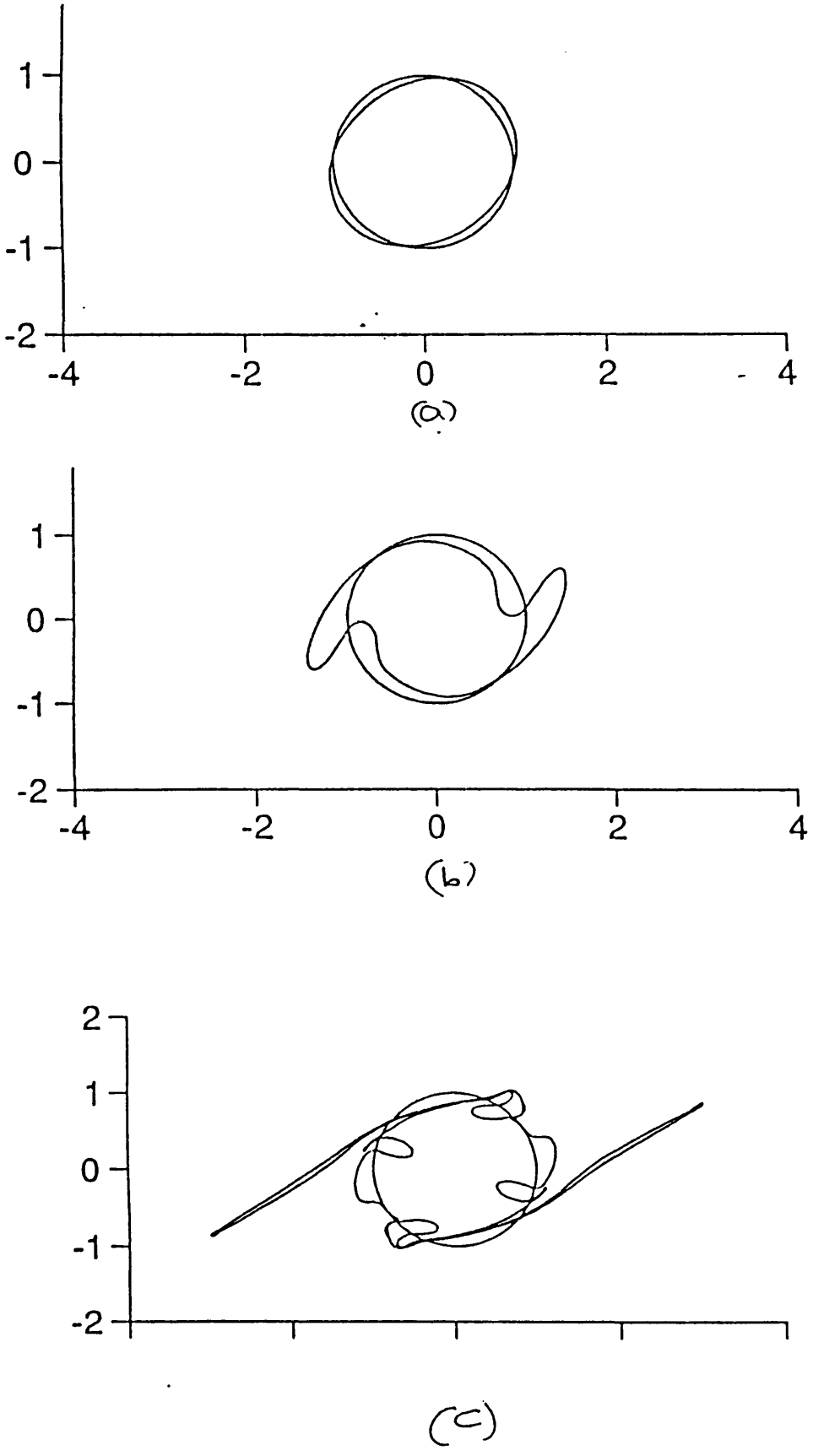

Figure 3.13.

Flow with positive shear, β = 2., for the rigid lid case. (a) t = 1 (b) t = 8 (c) t = 24.

obstacle. In this case however the shed regions are not borne away so rapidly, and new regions are shed, the boundary becoming extremely convoluted. On the longer viscous timescale those filaments which have been off the obstacle for a long time will be spun up by Ekman pumping. The amount of fluid shed in these filaments decreases, and thus eventually the steady state is set up. In this steady state, although there are closed streamlines surrounding the column and obstacle, there is still a generation and decay of vorticity, as fluid continues to move up onto the topography, gaining negative vorticity, which then decays due to Ekman pumping, so that when the fluid is carried off the topography it has a net positive vorticity, which decays in turn.

Figure 3.14 shows the flow for β = .2 and a = 1/3, for (a) t = 1, (b) t = 3, (c) t = 8. Again the more localised effect of the topography in the free surface case is seen. In this case the stronger shear carries the filaments away from the obstacle before the trapped region has rotated as far as in the rigid lid case, so the contour does not become so convoluted. The effects from the filaments are weaker as they are carried away, and the final steady shape is more clearly visible throughout.

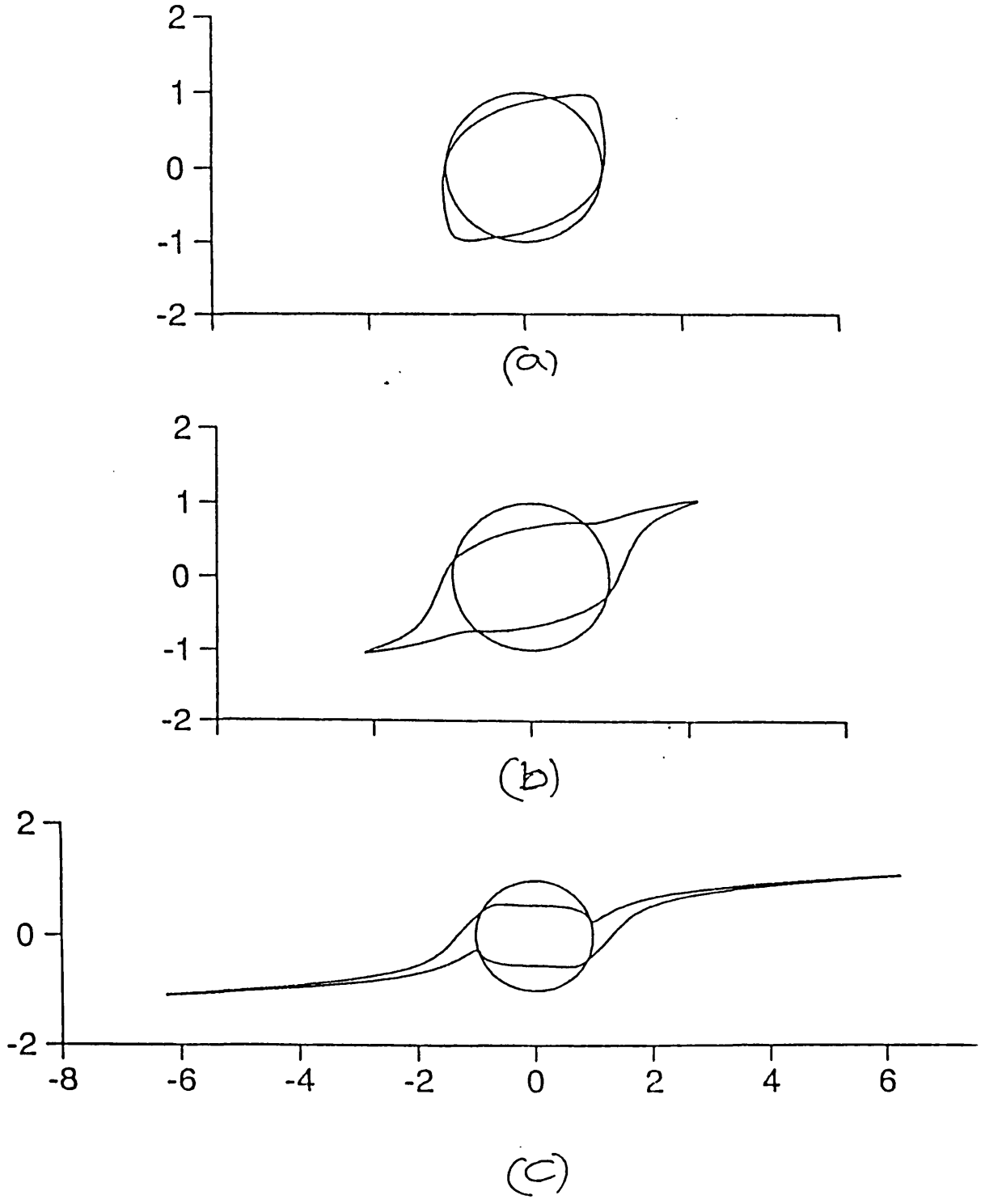

Figure 3.14.
The effect of a free surface on positively sheared flow, $\beta = 2.$, $a = 1/3$, for (a) $t = 1$ (b) $t = 3$ (c) $t = 8$.

§3.6. Discussion.

The initial-value problem of the uniform flow of an inviscid fluid forced over a cylindrical obstacle has been investigated using the contour dynamics method. It is found that the starting flow produces a topographic wave, travelling in a clockwise direction around the obstacle, in agreement with Johnson (1984). The ratio of this topographic effect to the effect of advection is measured by the parameter S. It is shown that a critical value exists for this parameter, depending on the Rossby radius of deformation. As this surface adjustment length tends to infinity, the rigid lid limit, the critical value for S tends to that given by Huppert (1975). As the Rossby radius decreases, the critical value increases without bound.

For values of S below the critical value, the fluid originally above the topography is carried downstream, forming a cyclonic vortex, due to the stretching of fluid filaments, and leaving an anticyclonic vortex above the obstacle. The approximate path of this cyclonic vortex is found analytically as a function of the Rossby radius, and is in agreement with the result of Huppert & Bryan (1976) in the rigid lid limit. The velocity of this advected vortex tends to that of the uniform stream, algebraically in the rigid lid limit and exponentially for a finite Rossby radius. This is shown to be a result of the localisation effect of a small Rossby radius, an effect which is examined by considering an isolated vortex for various values of the Rossby radius. It is found that as the surface can adjust faster for smaller values of a, vorticity is increasingly produced only at the edge of the topography, leading to a restriction of the velocity to a thin region at the boundary, decaying exponentially on both sides of this region, the central area of the vortex becoming virtually stagnant. Hence the topographic effect is smaller for finite values of the

Rossby radius, blocking is less likely to occur, and the effect on the downstream fluid diminished.

For values of S above the critical value, some of the fluid originally above the topography is held there, initially carried around by the topographic wave, during which stage more of the fluid may be carried off downstream, until finally the remaining fraction is caught over the obstacle within the closed streamline region of the zero potential vorticity flow, on the right-hand side of the obstacle looking downstream, eventually forming all or part of a stagnant Taylor column. It is shown that the trapped fluid forming this Taylor column may not all have originated over the obstacle, as upstream fluid can also be captured, provided that S is sufficiently large, and would then be spun up by Ekman pumping. Upstream anticyclonic fluid is easily caught and held, while upstream cyclonic fluid is carried past the obstacle in the manner of the translating vortex pairs of Deem & Zabusky (1978).

The method of contour dynamics allows the extension of this work to other oncoming flows, and in particular a shear flow is considered, for both positive and negative shears. For a negatively sheared oncoming flow, the results show the generation of two cyclonic eddies, whose paths are calculated. Meanwhile ever-smaller filaments of vorticity are shed from the obstacle, and as their size decreases a Taylor column forms over the topography, whose shape and position agrees with the steady results of Johnson (1983). The effect of a free surface is that more fluid is swept off the obstacle, thus decreasing the size of the Taylor column.

For a positively sheared oncoming flow the shed fluid remains in the vicinity of the obstacle for longer, and the structure of the contour becomes highly complex. The effect of the free surface, however, is that filaments which form around the obstacle are carried away, and therefore have less influence on the trapped fluid. Thus the Taylor column in this case is set up on this

filamentation timescale, as in the negatively sheared flow, rather than the longer viscous timescale over which the filaments remaining in the vicinity of the obstacle decay due to Ekman pumping.

On the whole it is not possible to model effects of viscosity using this contour dynamics method. However, the effect of Ekman pumping on a region of vorticity which remains otherwise constant, i.e. does not pass over any topography, may be modelled by allowing a time-dependent vorticity parameter. In Figure 3.15 the advected contour has been split into three contours, in order that the shed vortices may have exponentially decaying vorticity. The split takes place at t = 10, Figure 3.15 (a), and the vorticity in the shed contours is taken to be $\exp(-\gamma\tau)$ where γ is $E^{1/2}/Ro$, here taken to be .25. Here E is the Ekman number and $\tau = t - 10$. Clearly the vorticity which is constantly being produced at the obstacle as more fluid is shed will also decay but this is not modelled, the aim being to observe the decay of the shed vortices. Figure 3.15(b) shows the effect of this exponential decay in the vorticity, which is obviously to weaken the shed vortex, and it no longer rotates as rapidly as in the wholly inviscid case as it moves off.

One extension to this work lies in the number of density layers of the fluid. This number may be increased, provided that the depth of the lower layer is greater than the height of the obstacle.

The work in this chapter was carried out jointly by myself, Dr. E.R. Johnson and Dr. M.K. Davey and may be found in Hurst, Johnson & Davey (1990).

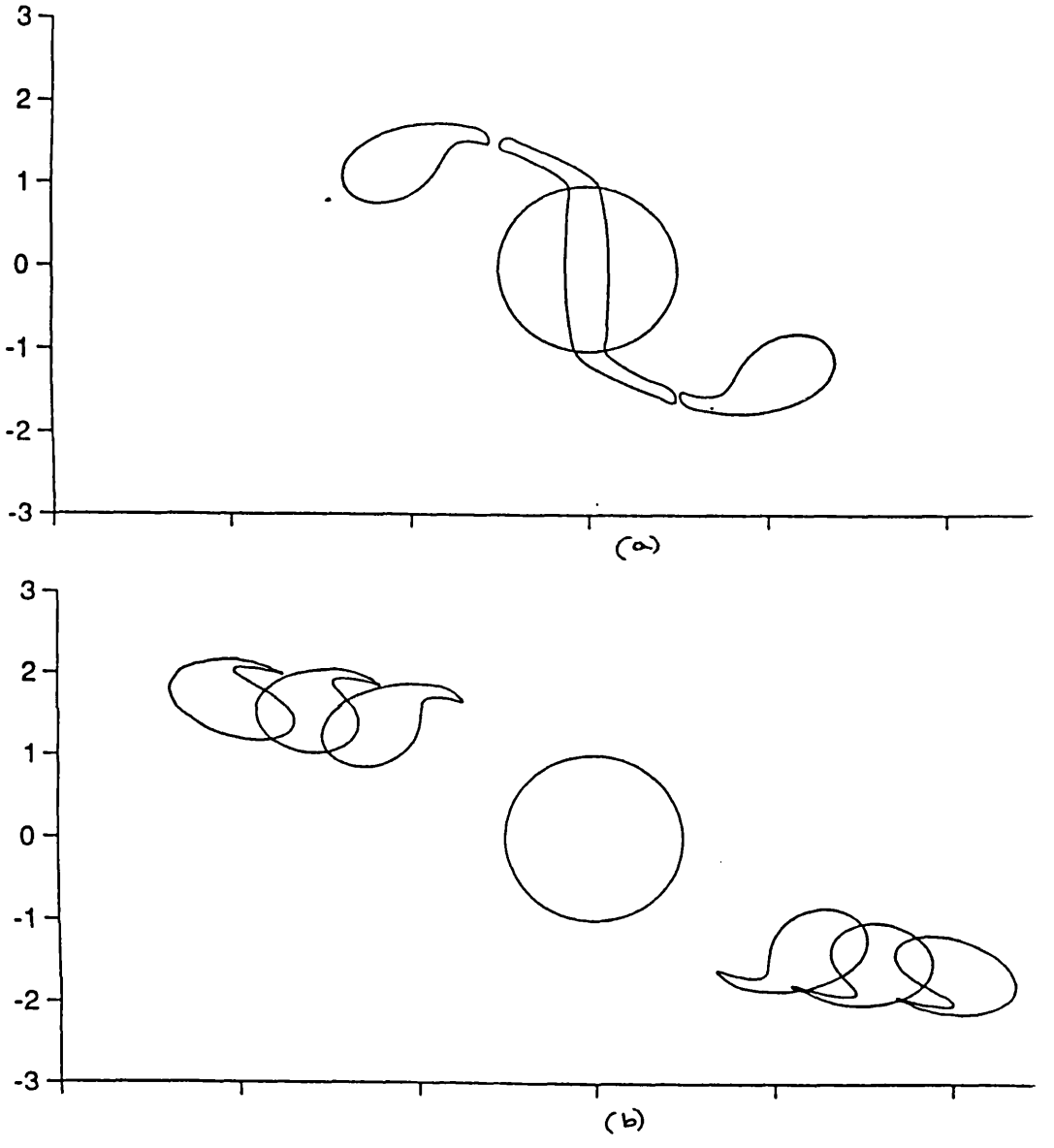

Figure 3.15.

The effect of Ekman pumping on the shed vortices. (a) The split made at t = 10. (b) The vortices at t = 11, 13, 15. As their vorticity decays exponentially they translate without rotating.

CHAPTER 4.

RAPID FORMATION OF TAYLOR COLUMNS: OBSTACLES AGAINST SIDEWALLS.

§4.1. Introduction.

In this chapter the behaviour of topographic waves such as those in Chapter 3 is examined more closely by considering the problem of topographic forcing by an obstacle against the boundary of a rotating flow in various parameter regimes. The timescale for the motion is the topographic vortex-stretching time, which, in §§4.3 and 4.4, is taken to be short compared with the advection time. This is in contrast to the system in the previous chapter, in which the effects of advection and topography combined to determine the development of the flow. In this case there is no advection over the timescale considered, so the flow is governed purely by the effects of the topography. It is shown that the presence of the sidewall causes a stagnant Taylor column to be set up far more rapidly than in cases with no sidewall.

Initial-value problems for slow flows in this limit have been considered previously in different geometries. For topography with closed isobaths, flow started from rest settles down asymptotically to almost periodic motion (Johnson 1984). For stepped topography with isobaths ending abruptly on sidewalls the almost periodic solutions are absent and the flow adjusts to become steady over a time of order the vortex-stretching time (Johnson 1985). The present geometry has the abruptly terminated isobaths of the latter geometry but the finite topographic extent of the former. It is shown that on a time of order the vortex-stretching time the flow becomes stagnant above the topography, giving a stagnant Taylor column. The column forms in the time taken for a long topographic wave to propagate along the obstacle, a time far shorter in this limit than the time required for a particle to be swept past the obstacle or for the column to spin down due to Ekman pumping.

Section 4.2 describes the equations of motion for this

flow, which contain the nondimensional parameters whose relative magnitudes determine the final state: again we find the Hide parameter, S; and in this case an Ekman number, μ. Sections 4.3 and 4.4 consider the limit of slow flow, Ro << 1, so topographic wave adjustment occurs before advection can become important. Section 4.3 discusses first the free modes, showing that waves approaching the wall decelerate and decrease in wavelength, whilst waves leaving the the wall, at the other end of the obstacle, accelerate and increase in wavelength. These free modes are superposed to solve the initial-value problem for an impulsively started flow. A steady final state is set up on the topographic timescale: stagnant Taylor columns are set up more rapidly when a sidewall is present. Section 4.4 discusses the effects of Ekman pumping on these solutions. Section 4.5 considers nonlinear effects, in seeking the final steady state. Section 4.6 summarises the results.

§4.2.The governing equations.

Throughout this chapter, unlike in Chapter 3, the fluid is assumed to be bounded by a rigid lid. The equation of continuity (1.4) allows the introduction of a volume flux stream-function, Ψ, defined by

$$hu = -\Psi_y \quad , \quad hv = \Psi_x . \tag{4.2.1}$$

Thus the relative vorticity, ζ, is given by

$$\zeta = v_x - u_y = \nabla.(h^{-1}\nabla\Psi). \tag{4.2.2}$$

The equation for the conservation of potential vorticity, i.e. equation (1.7), becomes

$$\zeta_t + k.\left\{\nabla\Psi \times \nabla\left[\frac{\zeta + f}{h}\right]\right\} = -\mu\zeta, \tag{4.2.3}$$

where a simple dissipation term has been included on the right hand side. In the limit of small Rossby number this reduces precisely to an Ekman pumping term (Johnson 1984) and is proportional to $\nu^{1/2}$ for kinematic viscosity ν.

Sections 4.3 and 4.4 discuss equation (4.2.3) in the limit of slow flow where topographic effects dominate and advective effects are negligible. In this limit, scaling μ with f, and using the inertial timescale, the nondimensional form of equation (4.2.3) becomes

$$\nabla.\left(\frac{1}{h}\nabla\Psi_t\right) + \partial(\Psi,\frac{1}{h}) = -\mu\nabla.\left(\frac{1}{h}\nabla\Psi\right), \tag{4.2.4}$$

where $\partial(\Psi, \ ) = \Psi_x\partial_y - \Psi_y\partial_x$.

We consider the particular case of a semi-cylindrical

obstacle, against the vertical sidewall of the rotating system. Take Cartesian axes Oxy with the x-coordinate along the wall and let the radius of the cylinder be unity. Transform the coordinates using the conformal mapping:

$$\xi + i\theta = 2\tanh^{-1}(x+iy). \qquad (4.2.5)$$

This introduces the bipolar coordinates (ξ,θ), with

$$x = \frac{\sinh\xi}{\cosh\xi + \cos\theta} \quad , \quad y = \frac{\sin\theta}{\cosh\xi + \cos\theta}, \qquad (4.2.6)$$

as shown in Figure 4.1. Equation (4.2.4) reduces to Laplace's equation away from the edge of the obstacle, with the dynamics contained in a jump condition at the step, Johnson (1985), Jansons and Johnson (1988), i.e.

$$\Psi_{\xi\xi} + \Psi_{\theta\theta} = 0, \quad (-\infty < \xi < \infty) \begin{pmatrix} 0\le\theta<\frac{1}{2}\pi \\ \frac{1}{2}\pi<\theta\le\pi \end{pmatrix}, \qquad (4.2.7a)$$

$$\left[\frac{1}{h}\Psi_{\theta t} + \frac{\mu}{h}\Psi_{\theta} + \frac{1}{h}\Psi_{\xi}\right] = 0, \ (-\infty < \xi < \infty) \ (\theta = \tfrac{1}{2}\pi), \qquad (4.2.7b)$$

$$\Psi = 0, \quad (-\infty < \xi < \infty) \ (\theta = 0,\pi), \qquad (4.2.7c)$$

where $\left[\ \right]$ represents the jump in the enclosed quantity at $\theta = \pi/2$ and h is the local depth, i.e. $h = h_1$ away from the obstacle and h_2 above it. Equation (4.2.7b) guarantees continuity of pressure at the step. Four timescales are relevant to the motion. These are the inertial period 1/f, where f is twice the rotation rate; the topographic vortex stretching time $f^{-1}h_1/(h_1 - h_2)$; the viscous spin-down time $[2h_1^2/(f\nu)]^{1/2}$ and the advection time L/U. There are thus three non-dimensional

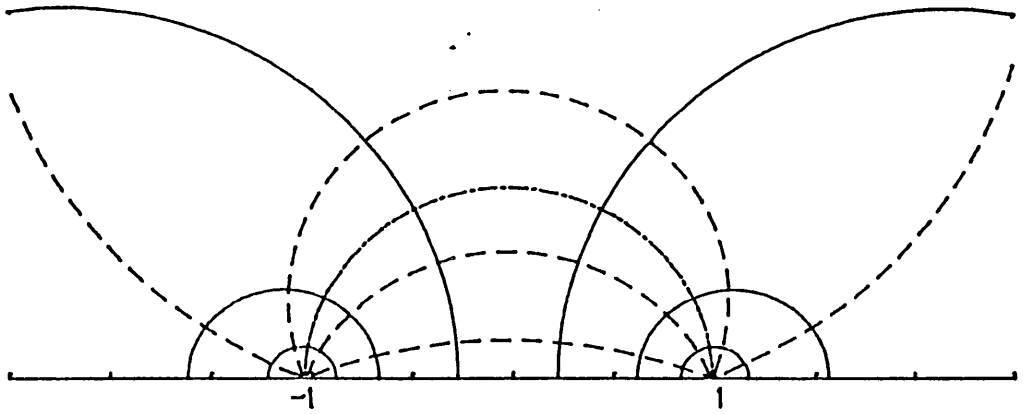

Figure 4.1

Coordinate lines of the bipolar coordinates, (ξ,θ). Lines of constant ξ are circles, centre $(\coth\xi,0)$, radius $\operatorname{cosech}\xi$. Lines of constant θ, shown dashed, are circles passing through $(\pm1,0)$, with ξ increasing from $-\infty$ to $+\infty$ on passing round the curved edge of the step, $\theta = \frac{\pi}{2}$, shown chained.

parameters in the problem. These can be taken to be the Rossby number, Ro = U/fL, comparing the timescales of the inertial to the advective effects; the Hide parameter, $S = (h_1 - h_2)/(h_1 Ro)$, measuring the relative importance of topographic to advective effects and an Ekman number, $\mu = [.5\nu f^{-1}/(h_1 - h_2)^2]^{1/2}$, which is the ratio of the viscous spin-down timescale to the topographic timescale and can also be regarded as the ratio of the thickness of the Ekman layer to the step height. In the topographic regime of §§4.3 and 4.4 the Rossby number is small, and the Hide parameter large: topographic effects are felt on a much shorter timescale than advective effects.

When the fluid is set impulsively in motion the pressure field instantaneously sets up an irrotational motion. If the fractional depth is not small this flow is not geostrophic and evolves to geostrophy over a time of order the inertial or topographic timescales, which coincide for order unity fractional depth. If the fractional depth is small as in Johnson (1985) the initial flow is uniform and geostrophic but not steady and evolves to a steady state over the topographic time which is then long compared to the inertial period.

§4.3.The linear inviscid case.

Consider the inviscid ($\mu = 0$) limit of (4.2.7). Then

$$\nabla^2\Psi = 0, \tag{4.3.1}$$

$$\left[\frac{1}{h}\Psi_{\theta t}\right] + \left\{\frac{h_2-h_1}{h_1h_2}\right\}\Psi_\xi = 0, \qquad (\theta = \frac{\pi}{2}). \tag{4.3.2}$$

§4.3.1 Free modes.

System (4.3.1)-(4.3.2) has solutions of the form:

$$\Psi = g(\theta)\exp\left\{ik\xi - i\omega t\right\}, \tag{4.3.3}$$

provided $g(0) = g(\pi) = 0$, and

$$\left[\frac{-i}{h}\omega g'(\theta)\right] + ik\left\{\frac{h_2-h_1}{h_1h_2}\right\}g(\theta) = 0, \qquad (\theta = \frac{\pi}{2}). \tag{4.3.4}$$

Thus g is given to within a multiplicative constant by

$$g(\theta) = \begin{cases} \sinh k\theta & (\theta < \frac{\pi}{2}) \\ \sinh k(\pi-\theta) & (\theta > \frac{\pi}{2}) \end{cases}, \tag{4.3.5}$$

where the jump condition gives the dispersion relation:

$$\omega = \Delta \tanh\frac{\pi}{2}k, \tag{4.3.6}$$

with $\Delta = (h_1 - h_2)/(h_1 + h_2)$. The phase and group speeds

are given by:

$$c_p = \frac{\Delta}{k}\tanh\tfrac{1}{2}\pi k \quad , \quad c_g = \frac{\Delta\pi}{2}\mathrm{sech}^2\tfrac{1}{2}\pi k. \qquad (4.3.7)$$

The waves are uni-directional, propagating with shallow water to their right for anticlockwise rotation and to their left for clockwise rotation. Interchanging h_1 and h_2, i.e. considering the case of a hollow of depth h_1 in a flow of depth h_2, is equivalent to reversing the direction of rotation.

Figure 4.2 shows the eddies moving around the step in the original coordinates, for the particular wavelength $k = 4$. The eddies are uni-directional, travelling clockwise around the step for anticlockwise background rotation. In the transformed plane waves propagate with no change of amplitude or wavelength. Long waves travel fastest, with group and phase speeds both $\frac{1}{2}\pi\Delta$ and both speeds decrease monotonically to zero with decreasing wavelength. Let ϕ be the usual polar angle in the original coordinates. Then $\cos\phi = \tanh\xi$. The wavelength, which is constant in ξ, becomes proportional to the distance from the wall, near the wall-step junctions. Similarly, the phase and group speeds, constant in ξ, vanish in the x-y plane as the points $(\pm1,0)$ are approached. Unlike the geometries of Johnson (1985), which similarly have either a source or a sink of eddies, the present geometry prevents the waves from growing arbitrarily.

§4.3.2 An initial-value problem.

Let the fluid be set into motion impulsively. Then the initial flow is irrotational and remains uniform at sufficiently large distance. In the transformed plane the effect is that of a dipole at the point $(0,\pi)$. The system to be solved is changed only in the boundary conditions. Now

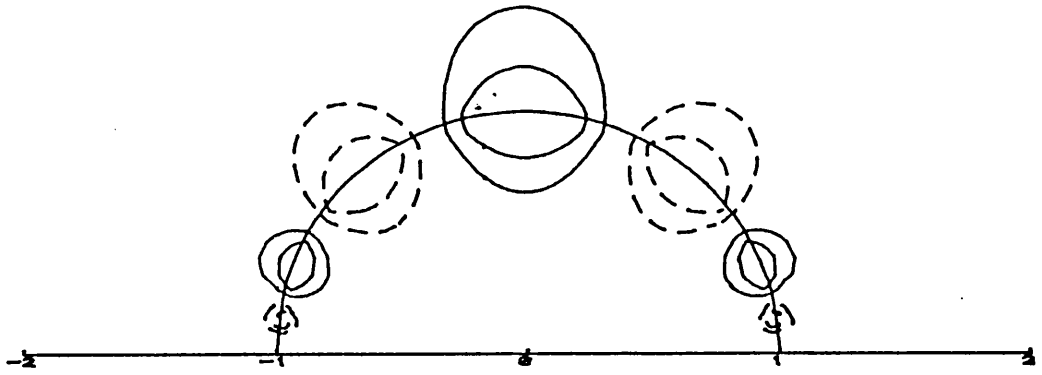

Figure 4.2

Eddies moving around the step in the original coordinates. In the transformed plane waves travel along the step, the amplitude decreases exponentially away from this line. In the original plane eddies created at (-1,0) move around the step ($h_1 > h_2$) and disappear at (1,0). Here k = 4 and the contours are drawn for amplitudes of -.25, -.5 (dashed) and .25, .5 (solid).

$$\Psi = 0 \qquad (\theta = 0), \tag{4.3.8a}$$

$$\Psi = -\delta(\xi) \quad (\theta = \pi), \tag{4.3.8b}$$

where $\delta(\xi)$ is the Dirac δ-function.

The new system has a Fourier integral solution:

$$\Psi(\xi,\theta,t) = \int_{-\infty}^{\infty} \hat{\Psi}(k,\theta,t)e^{ik\xi}dk, \tag{4.3.9}$$

provided

$$\hat{\Psi}_{\theta\theta} - k^2\hat{\Psi} = 0, \tag{4.3.10}$$

$$\hat{\Psi} = 0 \quad (\theta = 0), \quad \hat{\Psi} = -1 \quad (\theta = \pi), \tag{4.3.11a,b}$$

$$\left[\frac{1}{h}\hat{\Psi}_{\theta t}\right] + ik\left\{\frac{h_2 - h_1}{h_1 h_2}\right\}\hat{\Psi} = 0 \qquad (\theta = \frac{\pi}{2}). \tag{4.3.12}$$

At t = 0 the irrotational flow is given by

$$\Psi_0 = \begin{cases} -y(1-\Delta) & r < 1 \\ -y(1-\Delta/r^2) & r > 1 \end{cases}, \tag{4.3.13}$$

$$\hat{\Psi}_0 = \begin{cases} -(1-\Delta)\dfrac{\sinh k\theta}{\sinh k\pi} & \theta < \dfrac{\pi}{2} \\ -\dfrac{\sinh k\theta}{\sinh k\pi} + \Delta\,\dfrac{\sinh k(\pi-\theta)}{\sinh k\pi} & \theta > \dfrac{\pi}{2} \end{cases},$$

where r is the usual polar radial coordinate.

Write $\hat{\Psi} = \hat{\Psi}_0 + \hat{\Psi}_1(k,\theta,t)$. The jump condition provides the equation for time-dependence and the solution for Ψ is:

$$\Psi = \begin{cases} \displaystyle\int_{-\infty}^{\infty} \frac{-(1-\Delta)\sinh k\theta}{\sinh k\pi}\exp\left[ik\xi - i\omega t\right]dk & (0 \le \theta \le \pi/2) \\ \displaystyle\int_{-\infty}^{\infty}\left\{\frac{-\sinh k\theta}{\sinh k\pi} - \frac{\sinh k(\pi-\theta)}{\sinh k\pi}\left[(1-\Delta)\exp(-i\omega t) - 1\right]\right\}e^{ik\xi}dk & (\pi/2 \le \theta \le \pi) \end{cases}$$

$$= \Psi_\infty + \begin{cases} \int_{-\infty}^{\infty} -\frac{(1-\Delta)\sinh k\theta}{\sinh k\pi} \exp\left[ik\xi - i\omega t\right] dk & \theta \le \frac{\pi}{2} \\ \int_{-\infty}^{\infty} -\frac{(1-\Delta)\sinh k(\pi-\theta)}{\sinh k\pi} \exp\left[ik\xi - i\omega t\right] dk & \theta \ge \frac{\pi}{2} \end{cases}, \quad (4.3.14)$$

where

$$\Psi_\infty = \begin{cases} 0 & \theta \le \frac{\pi}{2} \\ \int_{-\infty}^{\infty} \frac{\sinh(\frac{\pi}{2}-\theta)k}{\sinh \frac{1}{2}\pi k} \exp(ik\xi) dk & \theta \ge \frac{\pi}{2} \end{cases}, \quad (4.3.15)$$

the two-dimensional irrotational flow past a right circular cylinder, stretching the whole depth of the fluid. Note Ψ_0 depends on Δ but Ψ_∞ is independent of Δ.

Expression (4.3.14) is readily evaluated using fast Fourier transforms. Figure 4.3 shows the streamlines in both the transformed and original planes for $\Delta = 1/2$. Eddies form just behind the point (0,1) and move clockwise around the step. The streamlines are deflected around the obstacle, and cross it in an exponentially thinning region near the step-wall junction at (1,0). Figure 4.4 shows the flow development with a hollow, $\Delta = -1/2$, rather than an obstacle. Comparing Figure 4.3(a) with Figure 4.4(a) shows the difference in the initial flows: the flow over the obstacle is only about 40% as strong as that away from it and hence the flow in Figure 4.3(d) above the obstacle is dominated by free waves, whereas over the hollow the initial flow is strong. The streamfunction along the step at times t=0 and t=100 is shown in Figure 4.5. Here the formation of eddies just before ξ=0 is clear. The wave front is seen to move around the step, leaving behind a wave-train. Consider first the point $\xi = 0$. At this point the integral form of the stream-function can be evaluated directly to give $\Psi(0,1) = -J_0(t)$, where $J_0(t)$ is the zeroth order Bessel function. The streamfunction

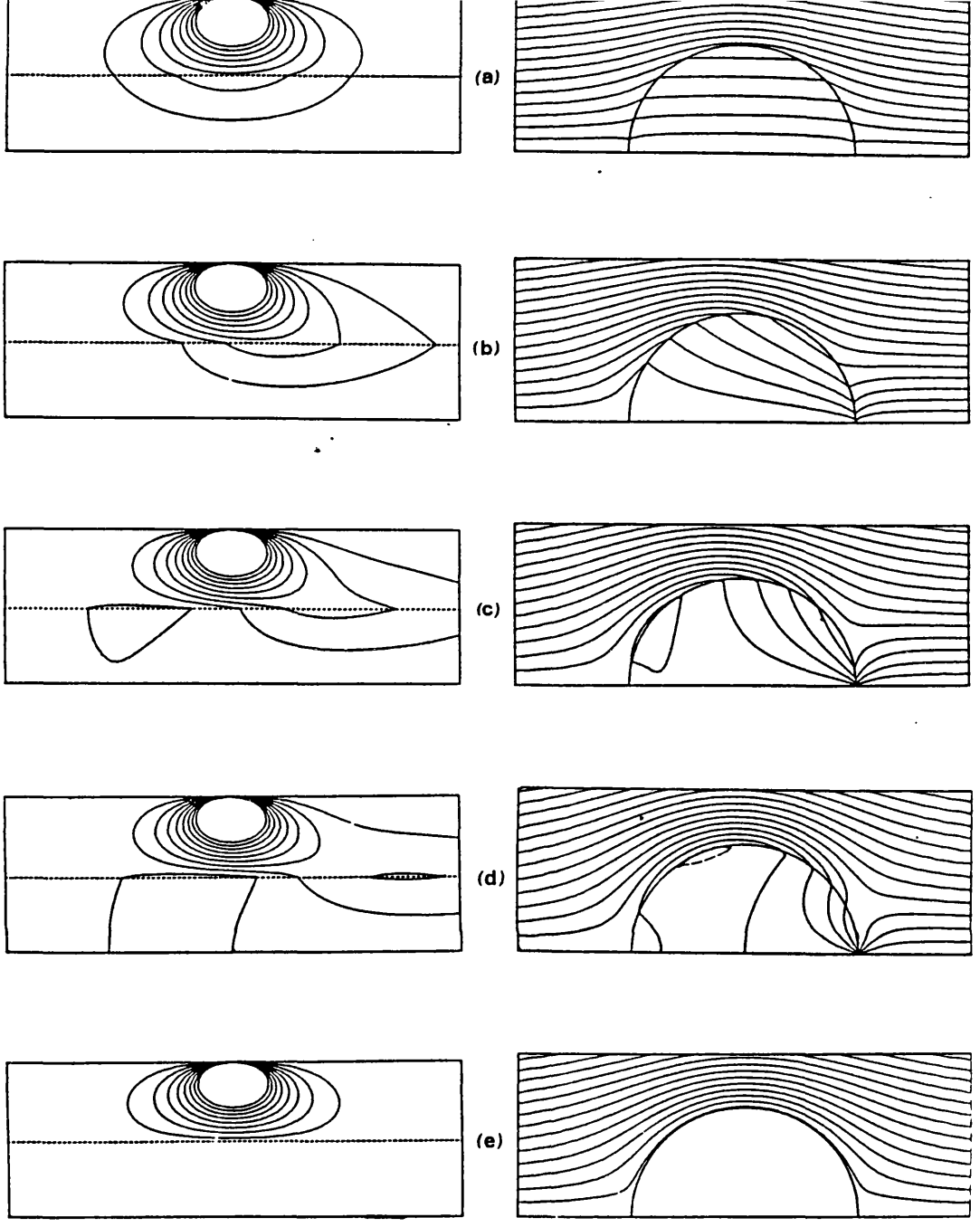

Figure 4.3

The development of the inviscid flow for $\Delta = 1/2$, in the transformed coordinates on the left and the original coordinates on the right. The streamlines are shown for (a) t=0, (b) t=2, (c) t=4, (d) t=6, (e) the steady state. In the transformed plane the contours are swept off to the right as expected from the free modes characteristics. In the original coordinates the streamlines are deflected around the obstacle and cross in an exponentially thinning region at the front. The contour interval is 0.2 in the ξ-θ plane and 0.1 in the x-y plane.

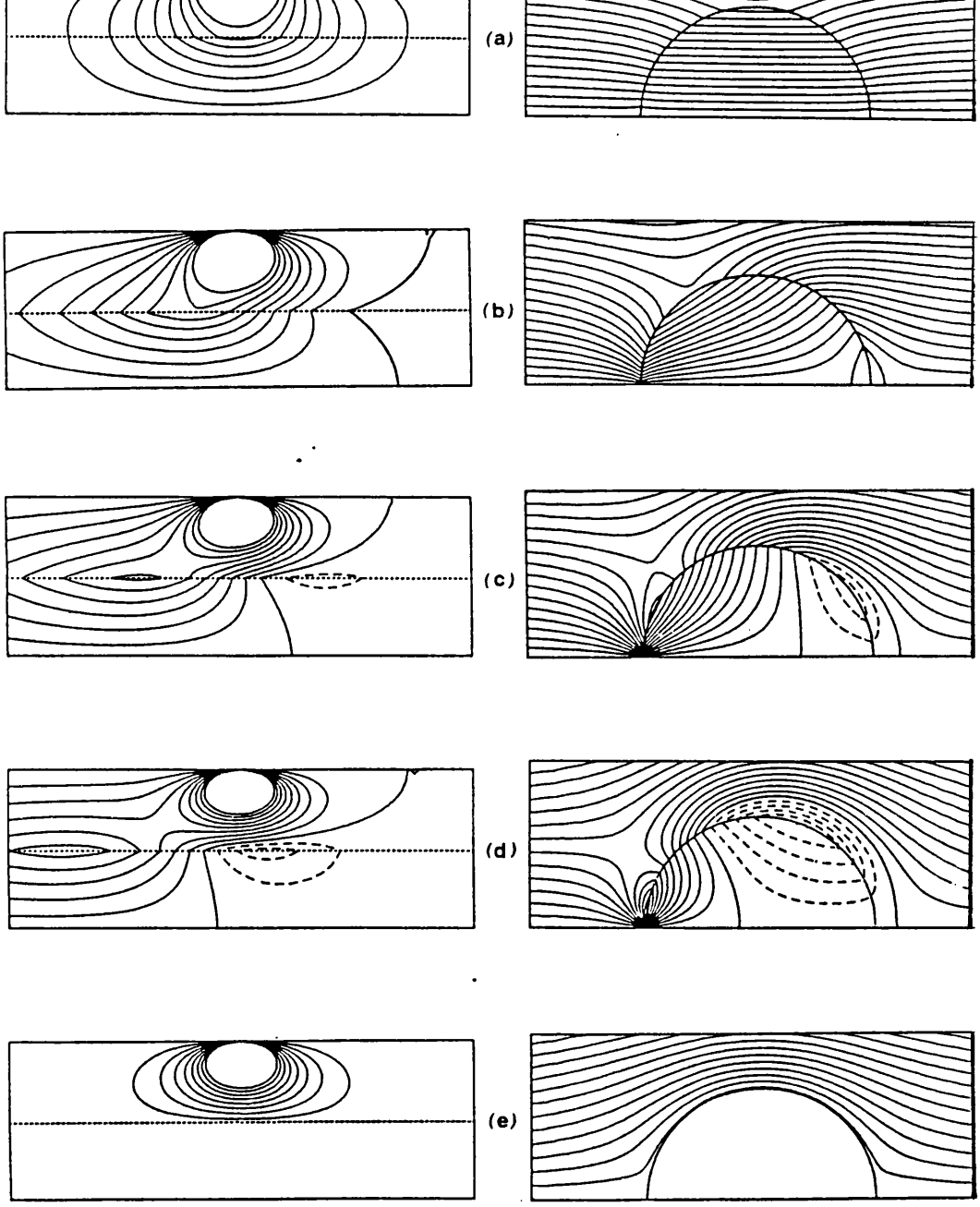

Figure 4.4

The development of the flow over a hollow with $\Delta = -1/2$, rather than an obstacle. The times and contour intervals are as in Figure 4.3.

oscillates with zero mean, and amplitude decaying as $t^{-1/2}$. For other values of ξ the long-time behaviour of the streamfunction can be obtained from the method of stationary phase. The dominant contribution to the integral comes from those values of k for which $\frac{\xi}{t} = c_g(k)$. The wave front moves along at the long-wave speed, i.e. the maximum group velocity, $\frac{\Delta\pi}{2}$. The stationary phase formula yields:

$$\Psi \sim -(\Delta\pi t)^{-1/2}\left[1-\frac{2\xi}{\Delta\pi t}\right]^{-1/4}\cos\left\{k_0\xi-\Delta t\left[1-\frac{2\xi}{\Delta\pi t}\right]^{-1/2}-\frac{\pi}{4}\right\}, \qquad (4.3.16)$$

where $k_0 = \frac{2}{\pi}$ arcsech $[2\xi/(\Delta\pi t)]^{1/2}$. Except at $\xi = \Delta\pi t/2$, where the singularity corresponds to the position of the wavefront, the streamfunction decays like $t^{-1/2}$. Near the front considering terms to third order gives:

$$\Psi \sim -(\Delta t)^{-1/3}\mathrm{Ai}\left\{\frac{2}{\pi}(\Delta t)^{-1/3}\left[\xi-\frac{\Delta\pi t}{2}\right]\right\}, \qquad (4.3.17)$$

where Ai is the Airy function.

In a widening region of thickness $t^{1/3}$ about the front, the disturbance decays like $t^{-1/3}$. This slower decay shows in the larger amplitude at the front in Figure 4.5.

There is no flow across the obstacle in the steady state: all streamlines are deflected around it. As the wavefront given by (4.3.16) moves from $\xi = -1$ to $\xi = 1$ in a time t of order unity, information in the untransformed plane moves from being an exponentially small distance from (-1,0) to being an exponentially small distance from (1,0) in a time of order unity. The steady pattern is set up almost everywhere on the topographic timescale, which is short compared to the advection timescale, provided $S >> 1$. In this respect the results differ markedly from those for flow unbounded by a sidewall. Ingersoll (1969) shows stagnant regions being set up on the longer, spin-down timescale. Similarly in Johnson (1984), for a cylindrical obstacle, the topographic waves produced when

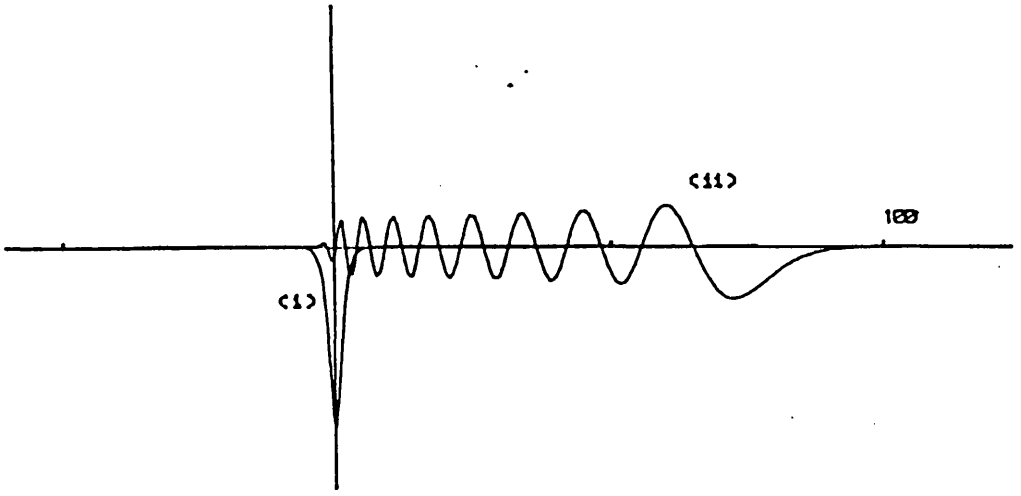

Figure 4.5

The stream function along the step at (i) t=0, (ii) t=100. $\Delta=1/2$. Initially the streamfunction is $-\mathrm{sech}\xi$. As the disturbance disperses, its amplitude decays as $t^{-1/2}$, except near the front which travels at speed $\pi/4$ and has amplitude decaying as $t^{-1/3}$.

the obstacle is set impulsively in motion cycle clockwise round closed isobaths in times of order the topographic timescale, continuing indefinitely in the absence of dissipation. It is the absence of closed geostrophic contours supporting free waves that accelerates the formation of a Taylor column against a sidewall.

§4.4.The linear viscous case.

Consider the effect of a bottom frictional force proportional to the velocity, thus corresponding to Ekman pumping for shallow topography. From §4.2 the equation of motion is:

$$\nabla.\left(\frac{1}{h}\,\nabla\Psi_t\right) + \mu\nabla.\left(\frac{1}{h}\,\nabla\Psi\right) + \partial\left(\Psi,\frac{1}{h}\right) = 0, \qquad (4.4.1)$$

where $\mu = [.5\nu f^{-1}/(h_1 - h_2)^2]^{1/2}$. As in §4.3, the dynamics are contained in a jump condition at the step, and elsewhere the flow is irrotational. The viscous term alters the jump condition to:

$$\left[\frac{1}{h}\,\Psi_{\theta t} + \frac{\mu}{h}\,\Psi_\theta\right] + \left\{\frac{h_2-h_1}{h_2h_1}\right\}\Psi_\xi = 0 \qquad \left(\theta = \frac{\pi}{2}\right). \qquad (4.4.2)$$

The solution is now

$$\Psi = \int_{-\infty}^{\infty}\left\{ -\frac{\sinh k\theta}{\sinh k\pi} - \frac{\sinh k\theta}{\sinh k\pi}\left[(\Gamma-\Delta)\exp(-\mu-i\omega)t-\Gamma\right]\right\}e^{ik\xi}dk$$

$$\left(\theta \le \frac{\pi}{2}\right)$$

$$(4.4.3)$$

$$\Psi = \int_{\infty}^{\infty}\left\{-\frac{\sinh k\theta}{\sinh k\pi} - \frac{\sinh k(\pi-\theta)}{\sinh k\pi}\left[(\Gamma-\Delta)\exp(-\mu-i\omega)t-\Gamma\right]\right\}e^{ik\xi}dk$$

$$\left(\theta \ge \frac{\pi}{2}\right)$$

where $\Gamma = i\omega/(\mu+i\omega)$. For flow started from rest the pattern initially evolves like the inviscid flow of §4.3

but quickly reaches the steady state

$$\Psi = \begin{cases} \displaystyle\int_{-\infty}^{\infty} -\frac{\sinh k\theta}{\sinh k\pi}\left[1 - \Gamma\right]e^{ik\xi}dk & (\theta \le \frac{\pi}{2}) \\ \displaystyle\int_{-\infty}^{\infty} \left\{ -\frac{\sinh k\theta}{\sinh k\pi} + \Gamma\,\frac{\sinh k(\pi-\theta)}{\sinh k\pi} \right\}e^{ik\xi}dk & (\theta \ge \frac{\pi}{2}) \end{cases} . \quad (4.4.4)$$

If $\mu = 0$, $\Gamma = 1$ and (4.4.4) reduces to (4.3.15). The flow becomes steady in an e-folding time of order μ. Comparing the results of the viscous and inviscid cases shows that viscosity arrests the flow at a stage of the inviscid development, intermediate between uniform flow and the final state of irrotational flow about a cylinder, as viscous dissipation destroys vorticity generated by vortex-stretching. The more viscous the fluid the earlier this arrest occurs: if the fluid were sufficiently viscous the irrotational flow of Figure 4.3(a) would be its steady state. This freeze is shown in Figure 4.6. In Figure 4.6(a) (μ=0.5, Δ=1/2) viscous effects are strong and the flow deviates little from uniform flow. In Figure 4.6(b) (μ=0.1, Δ=1/2) the viscous effects are weaker and the flow is closer to the two-dimensional irrotational flow. In Figure 4.6(c) ($\mu \approx 0.01$, Δ=1/7) parameter values corresponding to Figure 5(a) of Griffiths and Linden (1983) are used. Taking into account the difference expected due to the differing obstacle shapes the results agree well.

Changing the sign of f reflects the pattern about x=0. Altering the direction of the oncoming flow leaves the streamline pattern unchanged.

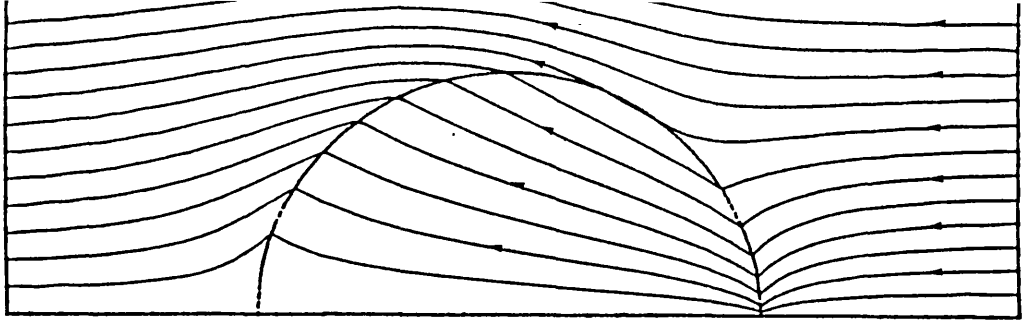

(a)

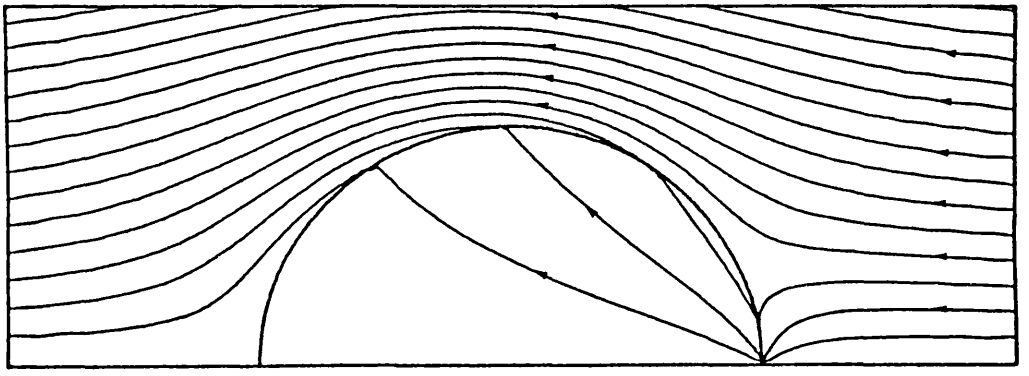

(b)

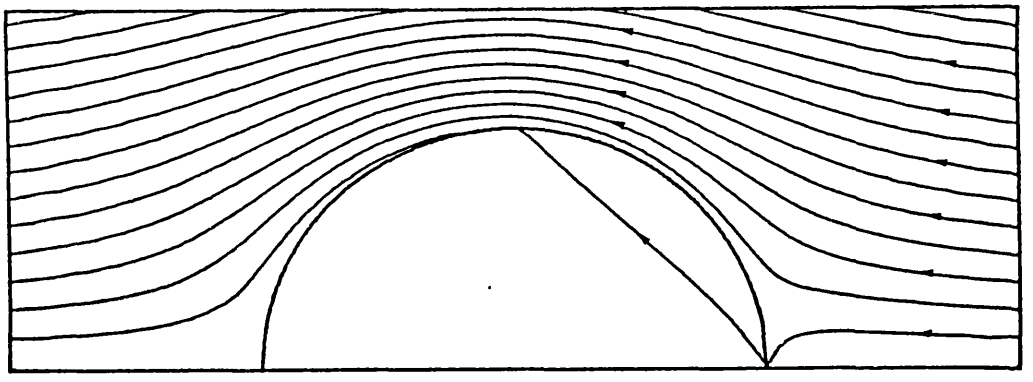

(c)

Figure 4.6

Steady viscous flows. Viscosity freezes the inviscid development. (a) $\mu = 0.5$, $\Delta = 1/2$, (b) $\mu = 0.1$, $\Delta = 1/2$, (c) the experimental regime of Griffiths and Linden ($\mu \approx 0.01$, $\Delta = 1/7$). Unlike the inviscid flows, some fluid passes over the obstacle. The more viscous the fluid is, the more fluid crosses the step.

§4.5.The nonlinear inviscid case.

For Rossby numbers of order unity, steady solutions can be found to the nonlinear equation, under the assumption that the imposed velocity is sufficiently large to sweep downstream all fluid initially above the obstacle. Conservation of potential vorticity then gives, above the obstacle, the nondimensional equation

$$1 = \frac{Ro\zeta + 1}{1-D}, \tag{4.5.1}$$

where D is the fractional height of the obstacle. It follows that

$$\nabla^2\Psi = \begin{cases} \dfrac{D(D-1)}{Ro} & \text{above the obstacle} \\ 0 & \text{elsewhere} \end{cases} . \tag{4.5.2}$$

Write $\Psi = -y + A\Phi$, where $A = \dfrac{D(D-1)}{Ro}$, and introduce polar coordinates (r,θ). Then

$$\nabla^2\Phi = \begin{cases} 1 & (r<1) \\ 0 & (r>1), \end{cases} \tag{4.5.3}$$

with the impermeability and boundary conditions

$$\Phi = 0 \quad \text{on } \theta = 0,\pi, \tag{4.5.4a}$$

$$\Phi \text{ bounded as } r \longrightarrow 0, \tag{4.5.4b}$$

$$\text{with } \Phi \text{ and } \frac{\Phi_r}{h} \text{ continuous at } r = 1. \tag{4.5.4c}$$

The solution of (4.5.3), (4.5.4) can be written:

$$\Phi = \begin{cases} \sum_{m=1}^{\infty} C_m \, r^{-(2m-1)} \sin\,(2m-1)\theta & r>1 \\ \sum_{m=1}^{\infty} C_m r^{2m-1} \sin(2m-1)\theta + D_m (r^2 - r^{2m-1}) \sin(2m-1)\theta & r<1 \end{cases} \qquad (4.5.5)$$

where

$$C_m = \frac{4(2m-3)}{(2-D)(2m-1)^2 \pi \left[4 - (2m-1)^2\right]} \qquad (4.5.6)$$

$$D_m = \frac{4}{(2m-1)\pi \left[4 - (2m-1)^2\right]}$$

Ingersoll (1969) shows that closed streamline regions become stagnant due to Ekman pumping destruction of vorticity over a timescale of order the viscous spin-up time. The solutions presented here have no closed streamlines provided the flow is sufficiently fast. For slower flow, closed streamlines are present in the solution and it is expected that they will evolve slowly to stagnant Taylor columns. The velocity component in the x-direction, $u = -\frac{1}{h}\Psi_y$, satisfies Laplace's equation above the obstacle and so, by the maximum principle, takes its extreme values on the boundary of the obstacle or against the wall. By symmetry these values occur on x=0. Thus stagnation in the flow occurs first with decreasing velocity at either the origin or at the point (x,y)=(0,1). Since $\Psi = -y + A\Phi$, a stagnation point will occur at the wall if $A < -1/u_1(0)$, where $u_1(0)$ is the topographically induced velocity at the origin. Similarly the critical value of A for the occurrence of a stagnation point at the step is $1/u_1(1)$, where $u_1(1)$ is the topographically induced velocity at the point (x,y) =

(0,1). Thus the case when A < 0, i.e. anticlockwise flow, can produce stagnation points only at the wall, while only clockwise rotation can lead to stagnation points on the step. The latter case requires a larger magnitude of A.

The figures have been presented for values just larger than those required to produce stagnation to illustrate the position of first stagnation and the nature of the flow. Figure 4.7(a) shows the case with closed streamlines forming at the wall. The streamlines are deflected away from the wall by the presence of the step. In Figure 4.7(b) the direction of rotation is reversed and the streamlines are pulled in towards the wall, closed streamlines beginning to form at the edge of the step.

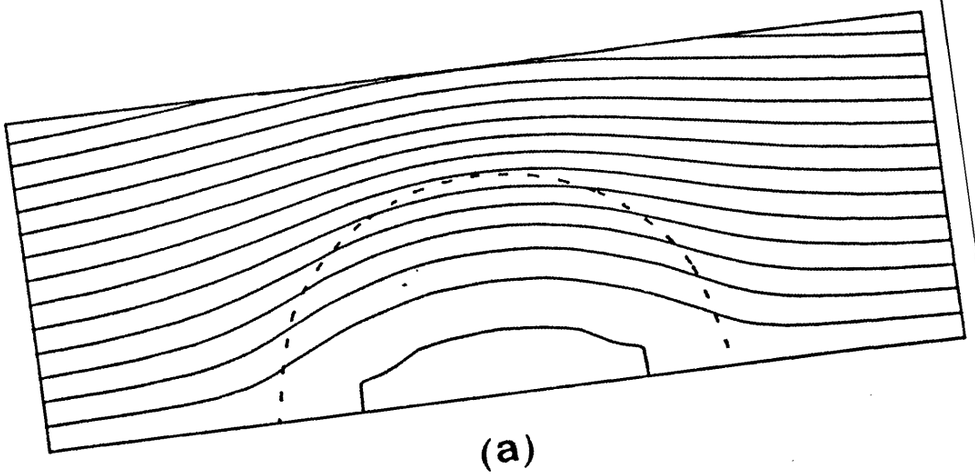

(a)

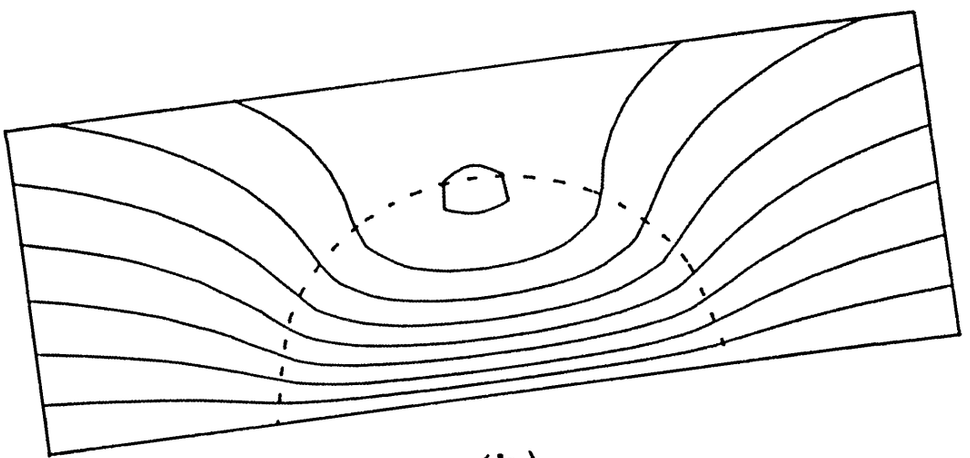

(b)

Figure 4.7

Contours of ψ for the nonlinear case.(a) A = -2, S = 2.7 and (b) A = 8, S = 8.9. The closed streamlines appear at the wall for case (a) and at the step for case (b).

§4.6.Discussion.

The problem of flow over an obstacle against a sidewall of a rapidly rotating container has been considered for various parameter regimes. In the inviscid limit and with a linear approximation to the governing conservation equation the flow is deflected by the obstacle, blocking occurs over it and eventually, in the steady state, there is no flow over it at all. This stagnant Taylor column is set up on the time taken for a topographic wave to travel along the semi-cylindrical boundary. As there are no closed isobaths the flow becomes almost steady far more rapidly than for flow over an isolated truncated cylinder where topographic waves can cycle the closed isobaths indefinitely (Johnson 1984). Introducing viscosity arrests the flow at some stage in this process, when the viscous dissipation destroys the vorticity created by vortex stretching. Even in the steady state some streamlines still cross the obstacle; the less viscous the flow the thinner the region in which they cross.

On reversing the direction of rotation the pattern is reflected about $x = 0$ for this linear approximation, where advective effects are assumed to be unimportant, but if the full nonlinear equation is used, different patterns are shown. The departure of the flow from the uniform stream changes sign and so the streamlines are either pushed away from the wall or pulled towards it.

Griffiths and Linden (1983) present experimental results for flow in a similar geometry, but over a quarter-sphere instead of a semi-cylinder. Again the presence of the sidewall is shown to have a large effect, and for the same parameter values the flow is effectively independent of depth. Figure 4.6(c) shows the streamlines computed for the parameter values corresponding to the experiments. Figure 5(a) in Griffiths and Linden (1983) is the most relevant: inertial waves are present in the others. Much of the difference in flow patterns can be

ascribed to the differing obstacle shapes. The depth change over the quarter-sphere is smooth whereas that over the semi-cylinder has a sharp discontinuity. From Johnson (1984), Figure 3(b), it can be seen that streamlines curve back on themselves for a smooth slope.

The rigid lid approximation has been made throughout this chapter. However, from the results of Chapter 3, it can be seen that the effect of a free-surface would be to localise the topographic wave influence to a thinner region along the edge of the topography.

Griffiths and Linden also present extensive results on separation. In the limit of small Rossby number the boundary layer structure for the flows in Figure 4.6 can be divided into three. A depth-independent layer of thickness of order $\nu^{1/4}$ brings the outer tangential velocity to zero at $r = 1^+$ and a similar $\nu^{1/4}$ layer brings the inner tangential velocity to zero at $r = 1^-$. Within these layers a vertically varying $\nu^{1/3}$ layer matches the derivatives of the tangential velocity and balances the Ekman fluxes. As the Rossby number increases separation occurs first in the $\nu^{1/4}$ layer. The dynamics of the depth-independent layers have been discussed by Walker and Stewartson (1972), Merkine and Solan (1979), Page (1987) and Page and Cowley (1988). Page (1987) shows that the dynamics are governed by a boundary layer equation of exactly the classical boundary layer form with an extra term giving the effect of rotation that delays separation. He points out that many features of the flow do not require detailed calculation of the profiles in the layer. He calculates separated flow solutions showing that the further the separation point migrates towards the rear stagnation point the narrower is the separated region.

In the present geometry for $r > 1$ the dynamics is precisely that considered by Page (1987). The sole difference is that, due to the combined effect of Ekman pumping and topography, there is a normal velocity at $r = 1^+$. Classical analyses of boundary layers with normal

velocities (Rosenhead, Ch.VI) show that separation is inhibited when fluid is sucked through the boundary and occurs almost immediately when fluid is blown through the boundary. Figure 4.8 gives the normal velocity across r=1 for the present geometry. For anticlockwise rotation, line (i) in Figure 4.8, fluid is sucked into the boundary layer in a region of favourable pressure gradient to be expelled in a region of adverse pressure gradient. The additional topographically generated velocities thus act to enhance separation which occurs then almost immediately after the zero of the normal velocity. For less viscous flow, line (iii), the zero of the velocity migrates towards the front stagnation point. From the results in Page (1987) this points to a wider separated region. For clockwise rotation fluid is blown from the boundary in a region of favourable pressure gradient but sucked into the boundary in a region of flow deceleration where separation would otherwise be likely. Hence the topographically generated velocities act to delay separation in this case. Any separation point will be closer to the rear stagnation point than if the cylinder extended throughout the depth of the fluid and from Page (1987) any separation bubble would be narrower. This description accords with the observations of Griffiths and Linden who show a wide separated region for anticlockwise rotation but little downstream influence for clockwise rotation.

The work in this chapter was carried out jointly by myself and Dr. E.R. Johnson and may be found in Hurst & Johnson (1990).

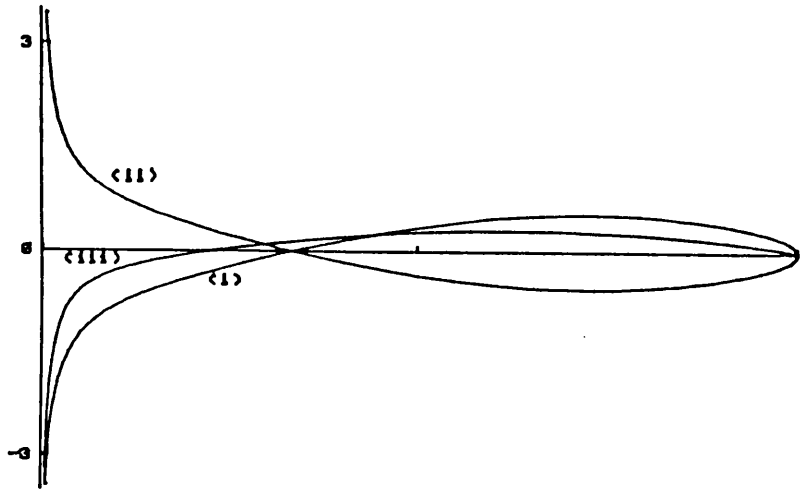

Figure 4.8

The radially-outward cross-step velocity in steady viscous flow for $0 \leq \phi \leq \Pi$ where ϕ is the usual polar angle. (i) μ = .5, with anticlockwise rotation flow passes onto the obstacle at the front and off at the rear, (ii) μ = .5, with clockwise rotation the flow directions are reversed, (iii) μ =.2, with anticlockwise rotation. In less viscous flow the region of entrainment is progressively moved towards the front stagnation point.

CHAPTER 5.

CHANNEL FLOW OVER TOPOGRAPHY.

§5.1 Introduction.

We return to the method of contour dynamics in this chapter, to examine the effects of topography on rotating flow in a channel. The physical system considered is illustrated in Figure 5.1. A rapidly rotating channel of uniform width, normalised to be π, contains fluid moving from right to left with uniform speed U. The bottom topography of the channel consists of a longitudinal step whose position is given by $y = Y_{TOP}(x)$ where $Y_{TOP}(x) \to \pi/2$ as $|x| \to \infty$, with deeper fluid lying to the right of the step, looking downstream. At some point along the channel there is an irregularity in the position of this step, here the flow may no longer be uniform and vorticity-free. The cross-stream width of this perturbation to the step is given by B and the perturbation length by 2A. This chapter tackles the initial-value problem of determining the evolution of the flow from an initial state of impulsively started uniform flow to its final steady state.

As was the case in previous chapters, the bathymetric variation leads to the generation of topographic waves, the effects of which combine with the advective effect of the oncoming flow. The relative strengths of these effects is again measured by the Hide parameter, S=U/fL, which is the ratio of the advective to topographic effects. If the oncoming flow is sufficiently fast, i.e. S is small, all the fluid is swept downstream, leaving a region of positive relative vorticity at the position of the topographic perturbation, constantly replenished by upstream fluid, in a similar fashion to the "fast" case of Chapter 3. For larger values of S, the topographic effects are stronger and, as in Chapter 3, the vorticity distribution grows more complicated.

The governing equations are discussed in §5.2 and the necessary modifications to the contour dynamics method are described. The method is basically that detailed in

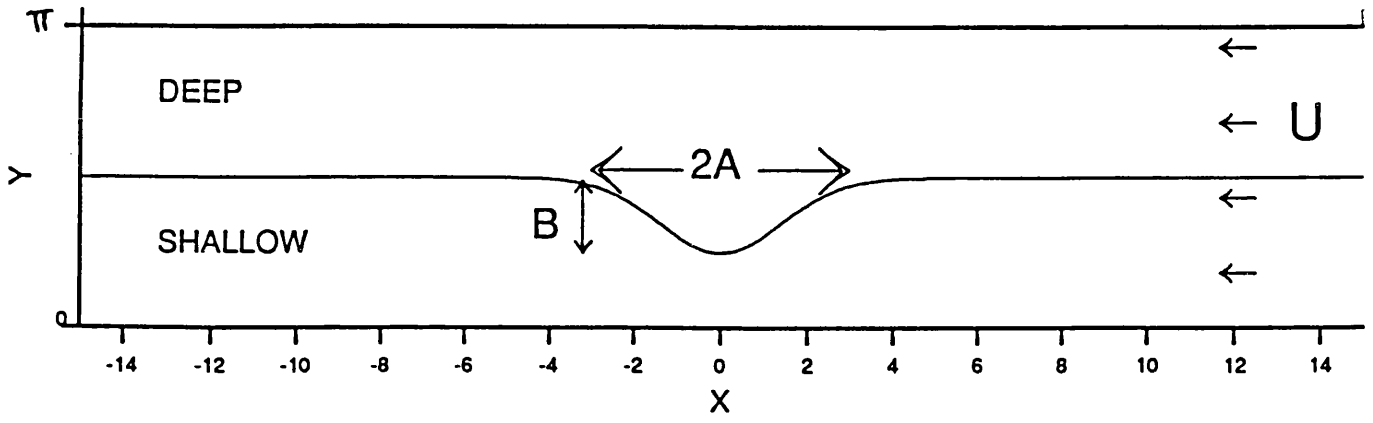

Figure 5.1

The physical system considered. A rapidly rotating channel of uniform width contains a step in the bottom topography at $y = Y_{TOP}$. The oncoming flow has speed U and is from right to left. The approximate length of the topographic perturbation is given by 2A, the width by B.

Chapter 2 and used in Chapter 3, but the channel geometry leads to a different Green's function in the stream function integral.

The vorticity distribution, and hence the entire flow field, may be determined from the instantaneous position of the line which initially lies along the step. This line, $y = Y(x,t)$, say, divides the regions of fluid with differing potential vorticities. In the final steady state $Y(x)$ is a streamline and in §5.3 the position of this streamline is found in three limits: $S \ll 1$, corresponding to a fast oncoming flow; $B \ll 1$, corresponding to a small cross-stream perturbation width and $A \gg 1$, i.e. the longwave limit wherein the perturbation varies slowly with x.

First, the fast case mentioned above is examined and the shape and position of the resulting region of positive relative vorticity are determined. The cross-stream width of this region is found to increase with B. As A is increased, the position of the interface rapidly reaches that predicted by longwave theory. The second case considered is that with a small value of B, i.e. a small cross-stream perturbation width. The nonzero relative vorticity region is treated as a sheet along the line $y = \pi/2$. It is in this limit that a standing topographic wave is seen, as larger values of S are used. For relatively small values of S the topographic waves cannot travel against the oncoming flow, but are carried downstream, leaving behind a simple vorticity distribution, similar to that of the first limit. As $S \to 0$ the predictions of the former theory are recovered and as A is increased the longwave prediction for the interfacial position is again rapidly attained. The critical value for S for the existence of a standing wave is found to be $4/\pi$. The group velocity of the waves is shown to be less than or equal to the phase speed for all wavelengths, with equality occurring only in the longwave limit, thus there is no standing wave possible upstream of the perturbation. Instead $Y(x)$ decays exponentially

towards $y = \pi/2$ in this direction for these small values of B.

In the third case the flow is considered in the longwave limit, i.e. $A \to \infty$, and we can study the effects of larger values of B and S. For small values of S the symmetric shape with the interface lying between the step and the wall at $y = \pi$ is again found. For values of S above the critical value of $4/\pi$, a new symmetric shape results, with the interface lying between the step and the wall at $y = 0$. This solution is shown to be possible only for values of B below a critical value which depends on S. For values of B above this critical value, a qualitatively new final position for the interface is shown. In this case the interfacial position tends to a constant value, greater than $\pi/2$, upstream and a different constant value, less than $\pi/2$, downstream. This asymmetric behaviour is significant, in that it shows that models of such flows must allow for the possibility of upstream influence.

The nonlinear evolution of Y(x,t) from its initial value of Y_{TOP} may be followed using the method of contour dynamics. The results are discussed in §5.4. Initially, in §5.4.1, the computation is carried out for parameter values corresponding to the limiting cases of §5.3, for comparison. The results show good agreement, particularly with the longwave limit, in which both the symmetric and asymmetric interfacial positions are seen. In §5.4.2 a wider parameter range is explored and a qualitatively new set of results is revealed, containing features which the three theories fail to capture. For values of S above the critical value, a lee wave again appears. However, in some cases this wave becomes highly nonlinear and overturns or "breaks", in a fashion reminiscent of the work of Pullin (1981), discussed in §2.1. An eddy is seen to form on the downstream side of the topographic perturbation and is then pinched off, in a similar way to those eddies studied by Pratt & Stern (1986).

§5.2 The governing equations and modifications to the contour dynamics method.

The governing equation is again that of conservation of potential vorticity, equation (1.7), and, as in Chapter 2, this may be linearised to give equation (2.2.4) for the stream function, Ψ. The rigid lid approximation is made throughout this chapter, i.e. the nondimensional Rossby radius, a/L, is taken as infinitely large. Thus in this case the stream function is given by equation (2.2.5), i.e.

$$\nabla^2\Psi = -Sh_B + \Omega \qquad (5.2.1)$$

The flow is started from rest and, as a result of the topographic variation, there are two regions with different potential vorticities: the shallow region, $y < Y_{TOP}(x)$, and the deeper region, $y > Y_{TOP}(x)$, where the position of the step is given by $y = Y_{TOP}(x)$. The topography is nondimensionalised to be

$$h_B = \begin{cases} 1 & y < Y_{TOP} \\ 0 & y > Y_{TOP} \end{cases}. \qquad (5.2.2)$$

The potential vorticities are therefore given by

$$\Omega = \begin{cases} S & y < Y_{TOP} \\ 0 & y > Y_{TOP} \end{cases}. \qquad (5.2.3)$$

As the fluid is advected by the oncoming stream the boundary between these two regions, $y = Y(x,t)$, is carried off the step, thus generating regions of nonzero relative vorticity, labelled A_1 and A_2 in Figure 5.2. Equation (5.2.1) thus gives

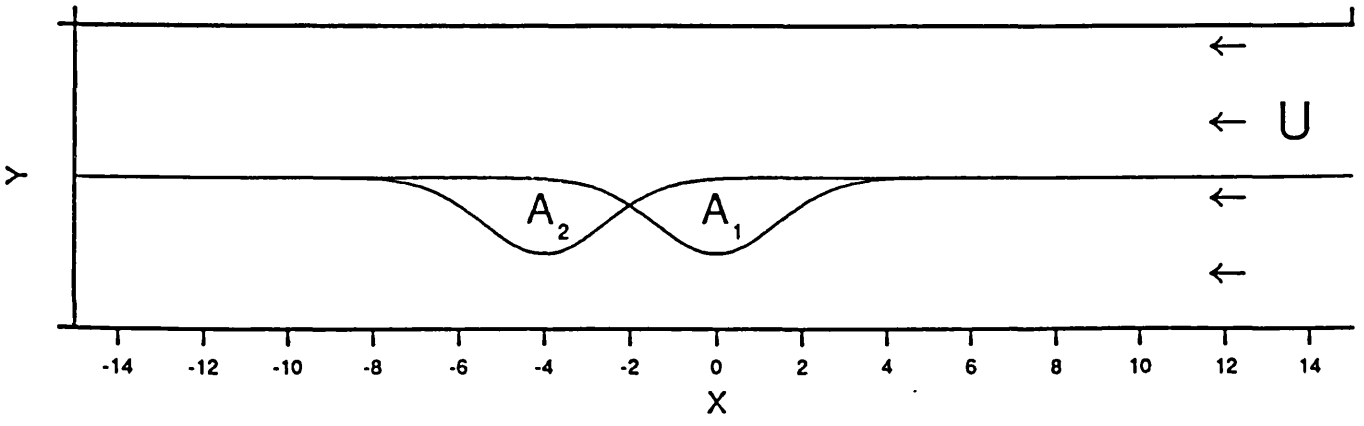

Figure 5.2

The nonzero relative vorticity regions generated from the oncoming flow. Region A_1 contains positive relative vorticity, region A_2 contains negative relative vorticity.

$$\nabla^2\Psi = \begin{cases} S & Y_{TOP} < y < Y \\ -S & Y^{TOP} < y < Y_{TOP} \\ 0 & \text{elsewhere} \end{cases}. \qquad (5.2.4)$$

As in Chapters 2 and 3, Ψ may be found from equation (5.2.4) by the use of Green's functions. In calculating the Green's function in this case the effects of the channel walls must be taken into account. This is achieved by using the transformation $\zeta = e^z$, where $z = x + iy$, to assess the contribution from the image vorticity patches. This maps the channel into the semi-infinite plane. Then the contribution to the stream function from a point vortex at (x_0,y_0), together with its image, is given by

$$(2\pi)^{-1}\log|\zeta - \zeta_0| - (2\pi)^{-1}\log|\zeta - \bar{\zeta}_0|$$

$$= (2\pi)^{-1}\log\left[\sinh^2(x-x_0)/2 + \sin^2(y-y_0)/2\right]^{1/2}$$

$$- (2\pi)^{-1}\log\left[\sinh^2(x-x_0)/2 + \sin^2(y+y_0)/2\right]^{1/2}.$$

Thus in the current case, wherein the only regions of nonzero vorticity are A_1 and A_2, Ψ is given by

$$\Psi(x,y,t)=(2\pi)^{-1}\iint_{A_1} S\log\left[\sinh^2\frac{(x-x_0)}{2} + \sin^2\frac{(y-y_0)}{2}\right]^{1/2} dx_0dy_0$$

$$- (2\pi)^{-1}\iint_{A_1} S\log\left[\sinh^2\frac{(x-x_0)}{2} + \sin^2\frac{(y+y_0)}{2}\right]^{1/2} dx_0dy_0$$

$$- (2\pi)^{-1}\iint_{A_2} S\log\left[\sinh^2\frac{(x-x_0)}{2} + \sin^2\frac{(y-y_0)}{2}\right]^{1/2} dx_0dy_0$$

$$+(2\pi)^{-1}\iint_{A_2} S\log\left[\sinh^2\frac{(x-x_0)}{2} + \sin^2\frac{(y+y_0)}{2}\right]^{1/2} dx_0 dy_0 . \quad (5.2.5)$$

The velocities are therefore given by differentiation of equation (5.2.5) to be

$$(u,v)=(2\pi)^{-1}\int_{\partial A_1} S\log\left[\sinh^2\frac{(x-x_0)}{2} + \sin^2\frac{(y-y_0)}{2}\right]^{1/2} (dx_0,dy_0)$$

$$-(2\pi)^{-1}\int_{\partial A_1} S\log\left[\sinh^2\frac{(x-x_0)}{2} + \sin^2\frac{(y+y_0)}{2}\right]^{1/2} (dx_0,dy_0)$$

$$-(2\pi)^{-1}\int_{\partial A_2} S\log\left[\sinh^2\frac{(x-x_0)}{2} + \sin^2\frac{(y-y_0)}{2}\right]^{1/2} (dx_0,dy_0)$$

$$+(2\pi)^{-1}\int_{\partial A_2} S\log\left[\sinh^2\frac{(x-x_0)}{2} + \sin^2\frac{(y+y_0)}{2}\right]^{1/2} (dx_0,dy_0), \quad (5.2.6)$$

where ∂A_1, ∂A_2 are the boundaries of A_1, A_2 respectively. However, as the magnitude of the vorticity is the same in both A_1 and A_2, integrating around ∂A_1 and ∂A_2 and subtracting the results is equivalent to integrating around the closed contour formed by the line $y = Y(x,t)$ from $x = \infty$ to $x = -\infty$ and the line $y = Y_{TOP}(x)$ from $x = -\infty$ to $x = \infty$. Far from the perturbation $Y(x,t) = Y_{TOP}(x)$, so the contributions cancel and the closed contour is kept finite in length. If further nonzero vorticity regions develop the argument is similar and one closed contour is sufficient to determine the flow. It is this contour that is used in the contour dynamics calculations. Corners are inserted at each "end" of the contour (see §2.1) in order to maintain the acute angle at which $Y(x,t)$ meets $Y_{TOP}(x)$. As the computation proceeds, it becomes

necessary in some cases to move the ends of the contour up- or downstream, to ensure that Y meets Y_{TOP} at a sufficiently acute angle.

As in Chapter 3, to carry out the integrations this closed contour is split into small sections whose contributions to the velocities are calculated separately and added. Along each small section the contour is again approximated by a cubic, ensuring continuity of curvature, and the integral is evaluated using the Lobatto formula (see Abramowitz & Stegun). The sections which end on the node whose velocity is to be found are approximated by straight lines. Here the integrand is approximated by a simple logarithm and the integral is evaluated exactly. In this way the line $y = Y(x,t)$ is tracked from its initial position along $y = Y_{TOP}(x)$ to its final steady position.

§5.3.Some limiting cases.

§5.3.1 The "fast" case, S « 1.

In this sub-section the shelf perturbation is taken to be rectangular. A small value of S represents the case with a fast oncoming flow, which sweeps the fluid away downstream. In terms of topographic waves, the speed of the oncoming flow is far greater than the phase and group speeds of the waves, which therefore cannot propagate upstream.

We seek the steady position of the line, $y = Y(x)$, which divides the regions containing different potential vorticities. The deviation from $Y(x) = \pi/2$ is $O(S)$.

Let $\Psi(x,y) = y + S\Phi(x,y)$. Then the streamline required is that along which $\Psi = \pi/2$, since $\Phi \to 0$ as $|x| \to \infty$. Hence

$$Y(x) = \pi/2 - S\Phi(x,\pi/2) + O(S^2). \qquad (5.3.1)$$

From equation (5.2.3),

$$\nabla^2\Phi = H(x+A)\, H(A-x)\, H(\pi/2-y)\, H(B-\pi/2+y), \qquad (5.3.2)$$

where $H(x)$ is the Heaviside step function. The boundary conditions are given by

$$\Phi = 0 \qquad \text{at } y = 0,\pi, \qquad (5.3.3a,b)$$

$$\Phi, \Phi_y \text{ continuous at } y = \pi/2,\ \pi/2-B. \qquad (5.3.4a\text{-}d)$$

Taking Fourier transforms in x of equation (5.3.2) gives

$$\hat{\Phi}_{yy} - k^2\hat{\Phi} = \sigma(k)\, H(\pi/2-y)\, H(B-\pi/2+y), \qquad (5.3.5)$$

where $\Phi(x,y) = (2\pi)^{-1} \int_{-\infty}^{\infty} \hat{\Phi}(k,y)\, e^{ikx}\, dk$, and $\sigma(k) = (2/\pi)^{1/2}\sin Ak/k$. Hence

$$\hat{\Phi}(k,y) = \begin{cases} A_1 \sinh ky & y<\pi/2-B \\ C_1 \sinh ky + D_1 \cosh ky & \pi/2-B<y<\pi/2, \\ B_1 \sinh k(\pi-y) & y>\pi/2 \end{cases} \qquad (5.3.6)$$

where A_1, B_1, C_1 and D_1 are found from (5.3.4a-d). Then equation (5.3.1) gives

$$Y(x) = \pi/2 - S/2\pi \int_{-\infty}^{\infty} B_1 \sinh k\pi/2\, e^{ikx}\, dk$$

$$= \pi/2 + S/2\pi \int_{-\infty}^{\infty} \frac{\sinh kA}{k^3} \left[1 - \frac{\cosh k(\pi/2-B)}{\cosh k\pi/2}\right] e^{ikx} dk. \qquad (5.3.7)$$

Expression (5.3.7) is readily evaluated using fast Fourier transforms, and the results are shown in Figure 5.3. Figure 5.3(a) shows a typical steady state, here A = 4 and B = $\pi/4$. The line y = Y(x) bows outward from y = $\pi/2$ around x = 0, but rapidly tends to $\pi/2$ away from the perturbation. Figure 5.3(b) shows $S^{-1}Y_0 = S^{-1}(Y(0) - \pi/2)$ against B, again for A = 4. As B increases from zero to its maximum value of $\pi/2$, the maximum deviation of Y(x) from y = $\pi/2$ increases, as there is a larger area of relative vorticity present. Figure 5.3(c) shows $S^{-1}Y_0$ against A, for B = $\pi/4$. As A increases, $S^{-1}Y_0$ quickly attains its longwave limiting value, given by $S^{-1}Y_0 = B(\pi-B)/4$.

§5.3.2 A small perturbation, B << 1.

In the rest of this chapter the position of the step is given by $Y_{TOP}(x) = \pi/2 - B \exp(-x^2/A^2)$. In the limit of small B the region of nonzero vorticity is taken to be of

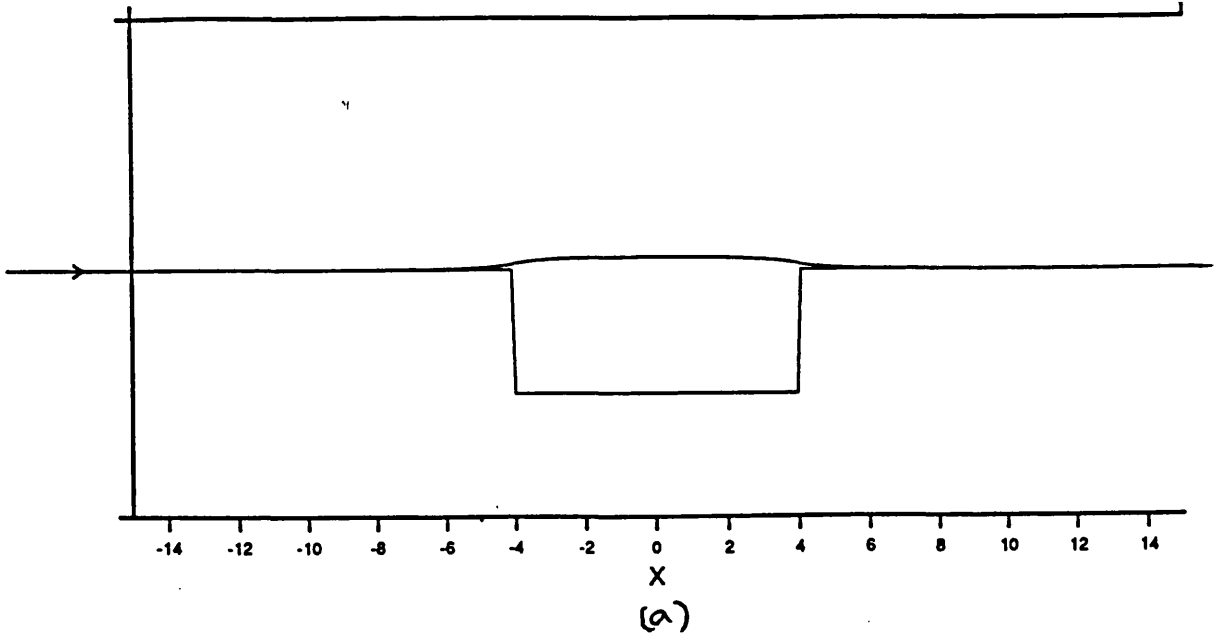

(a)

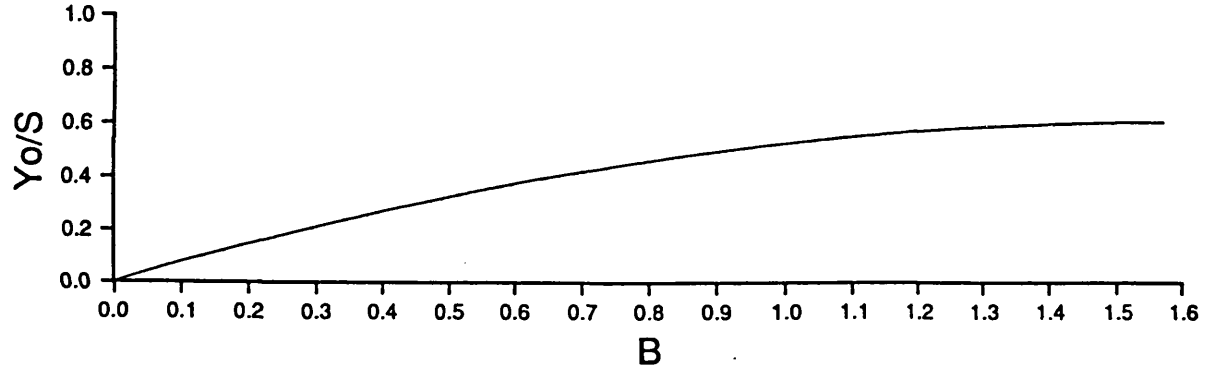

(b)

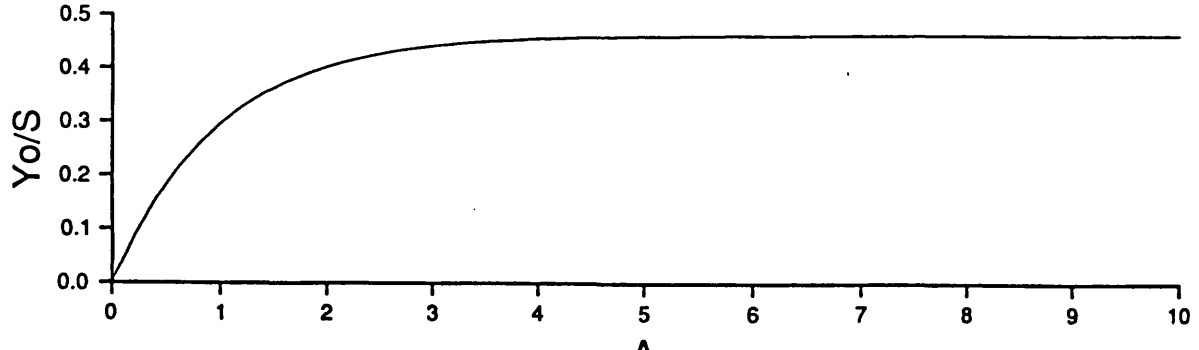

(c)

Figure 5.3

The results for the limiting case of small S. (a) A typical steady state. A = 4, B = $\pi/4$. (b) The maximum deviation of $S^{-1}Y$ from $\pi/2$, given by $S^{-1}Y_0$, against B, for A = 4. (c) $S^{-1}Y_0$ against A for B = $\pi/4$.

y-extent of O(B). We can take the vorticity to be confined to lie along the line $y = \pi/2$. The stream function is written as

$$\Psi(x,y,t) = y + B\Phi(x,y,t). \tag{5.3.8}$$

If A_1 and A_2 are the two nonzero vorticity regions shown in Figure 5.2, then, from equation (5.2.3), Φ is given by

$$B\nabla^2\Phi = \begin{cases} S & \text{in } A_1 \\ -S & \text{in } A_2 \\ 0 & \text{elsewhere} \end{cases}. \tag{5.3.9}$$

Again the argument may be extended to many regions of nonzero vorticity. Before solving the above equations it is helpful to consider the free topographic wave modes which may occur. Away from $y = \pi/2$, equation (2.2.3) reduces to Laplace's equation, i.e.

$$\nabla^2\Phi = 0 \qquad y \neq \pi/2, \tag{5.3.10}$$

with $\Phi = 0$ at $y = 0, \pi$ and integrating equation (2.2.3) across the step gives the jump condition, valid on y-scales greater than O(B),

$$\left[\Phi_{yt} - \Phi_{yx} - S\Phi_x h_B \right] = 0. \tag{5.3.11}$$

Seeking a solution of the form $\Phi \propto g(y)e^{ikx-i\omega t}$, we find g(y) is given to within a multiplicative constant by

$$g(y) = \begin{cases} \sinh ky & y<\pi/2 \\ \sinh k(\pi-y) & y>\pi/2 \end{cases}. \tag{5.3.12}$$

Then equation (5.3.11) gives the dispersion relation for the possible topographic waves as

$$\omega = -k + S/2 \tanh \pi k/2. \qquad (5.3.13)$$

This is the dispersion relation given in Chapter 4, together with an advection term. A standing wave occurs when $\omega = 0$. This is possible only for values of S greater than $4/\pi$ and only for such values of S may waves propagate upstream. These, then, are the possible topographic wave modes which may occur.

Returning now to equation (5.3.9), Φ may be written, as in §5.2, as

$$B\Phi(x,y,t)=(2\pi)^{-1}\iint_{A_1} S\log\left[\sinh^2\frac{(x-x_0)}{2} + \sin^2\frac{(y-y_0)}{2}\right]^{1/2} dx_0 dy_0$$

$$- (2\pi)^{-1}\iint_{A_1} S\log\left[\sinh^2\frac{(x-x_0)}{2} + \sin^2\frac{(y+y_0)}{2}\right]^{1/2} dx_0 dy_0$$

$$- (2\pi)^{-1}\iint_{A_2} S\log\left[\sinh^2\frac{(x-x_0)}{2} + \sin^2\frac{(y-y_0)}{2}\right]^{1/2} dx_0 dy_0$$

$$+ (2\pi)^{-1}\iint_{A_2} S\log\left[\sinh^2\frac{(x-x_0)}{2} + \sin^2\frac{(y+y_0)}{2}\right]^{1/2} dx_0 dy_0 \qquad (5.3.14)$$

using the Green's function for equation (5.3.9), incorporating the effects of the image vortices in the walls of the channel. The kinematic condition along $y = Y(x,t)$ may be written

$$v(x,y,t) = Y_t + Y_x. \qquad (5.3.15)$$

Using the relation between the stream function and the

horizontal velocities, taking y and y_0 to be approximately $\pi/2$ and taking the Fourier transform in x of equation (5.3.15), gives

$$\hat{Y}_t + ik\hat{Y} = ikS\left\{\hat{Y}(k,t) - \hat{Y}_{TOP}(k)\right\} \frac{\tanh k\pi/2}{2k},$$

where $Y(x,t) = (2\pi)^{-1}\int_{-\infty}^{\infty}\hat{Y}(k,t)\, e^{ikx}\, dk$. Hence

$$\hat{Y}(k,t) = \hat{Y}_{TOP}(k)\left[\, 1 - \frac{k}{\omega}\left(e^{i\omega t} - 1 \right) \right], \qquad (5.3.16)$$

where ω is the topographic wave frequency given by (5.3.13) and thus

$$Y(x,t) = Y_{TOP}(x) + (2\pi)^{-1}\int_{-\infty}^{\infty}\hat{Y}_{TOP}(k)\frac{k}{\omega}(1 - e^{i\omega t})e^{ikx}\, dk \qquad (5.3.17)$$

As $\omega'(k)$ has no maximum or minimum, the method of stationary phase may be used to show that the unsteady component of this integral decays algebraically in time. The steady solution is therefore given by

$$Y(x) = Y_{TOP}(x) + (2\pi)^{-1}\int_{-\infty}^{\infty}\frac{-k\hat{Y}_{TOP}e^{ikx}}{k - S/2\, \tanh k\pi/2}\, dk. \qquad (5.3.18)$$

The phase speeds of the waves are given by

$$c_p = \omega/k = -1 + S/2k\, \tanh k\pi/2,$$

thus a standing wave is possible if $S > 4/\pi$. The group velocity is given by

$$c_g = d\omega/dk = -1 + S\pi/4\, \mathrm{sech}^2 k\pi/2,$$

and is thus always less than the phase speed, except in the longwave limit, $k = 0$. Any standing wave must therefore lie only to the downstream side of the perturbation. For $S < 4/\pi$, the only poles in the integrand in equation (5.3.18) lie on the imaginary axis. These give a symmetric solution for $Y(x)$ which decays exponentially as $|x| \to \infty$. For $S > 4/\pi$ there are also two poles on the real axis, which give rise to the wavelike component of $Y(x)$. The above condition, that the standing wave lies only to the downstream side of the perturbation, requires that the path of integration lies above these poles. The integral in (5.3.18) is evaluated using fast Fourier transforms and the results are shown in Figure 5.4. For $S < 4/\pi$ no standing wave is possible and the result is symmetric in x. Figure 5.4(a) shows such a result with $B = .025\pi$, $S = 1$ and $A = 4$. As in the previous limit $Y(x)$ tends rapidly to $\pi/2$ away from $x = 0$.If $S > 4/\pi$, however, a lee wave is present. Such a lee wave is shown in Figure 5.4(b), where $S = 3$ and again $B = .025\pi$, $A = 4$. Figure 5.5(a) shows $Y^* = B^{-1}(Y(x) - \pi/2)$ against A, for $S = 1$. The longwave limit is again reached for a relatively small value of A, and is given by $Y^* = S\pi/(4-S\pi)$. Figure 5.5(b) shows Y^* against S for $S < 4/\pi$, with $A = 4$. As $S \to 0$, $\hat{Y} \to \hat{Y}_{TOP}\tanh(\pi k/2)/2k$ in agreement with the limit of §5.3.1 as $B \to 0$.

§5.3.3 The longwave limit, $A \gg 1$.

In this case the topographic perturbation is taken to be extremely long and $Y(x)$ is calculated assuming Y_{TOP} to be locally constant, thus neglecting variations in the x direction, i.e. along the channel. The method of calculating the steady interfacial position is illustrated in Figure 5.6. The conservation of mass flux above and below the streamline $y = Y(x)$ gives two equations for the unknowns $Y(x)$ and U_1, the velocity for $0 < y < Y_{TOP}$ at the perturbation, for a given B. If Y_1 is

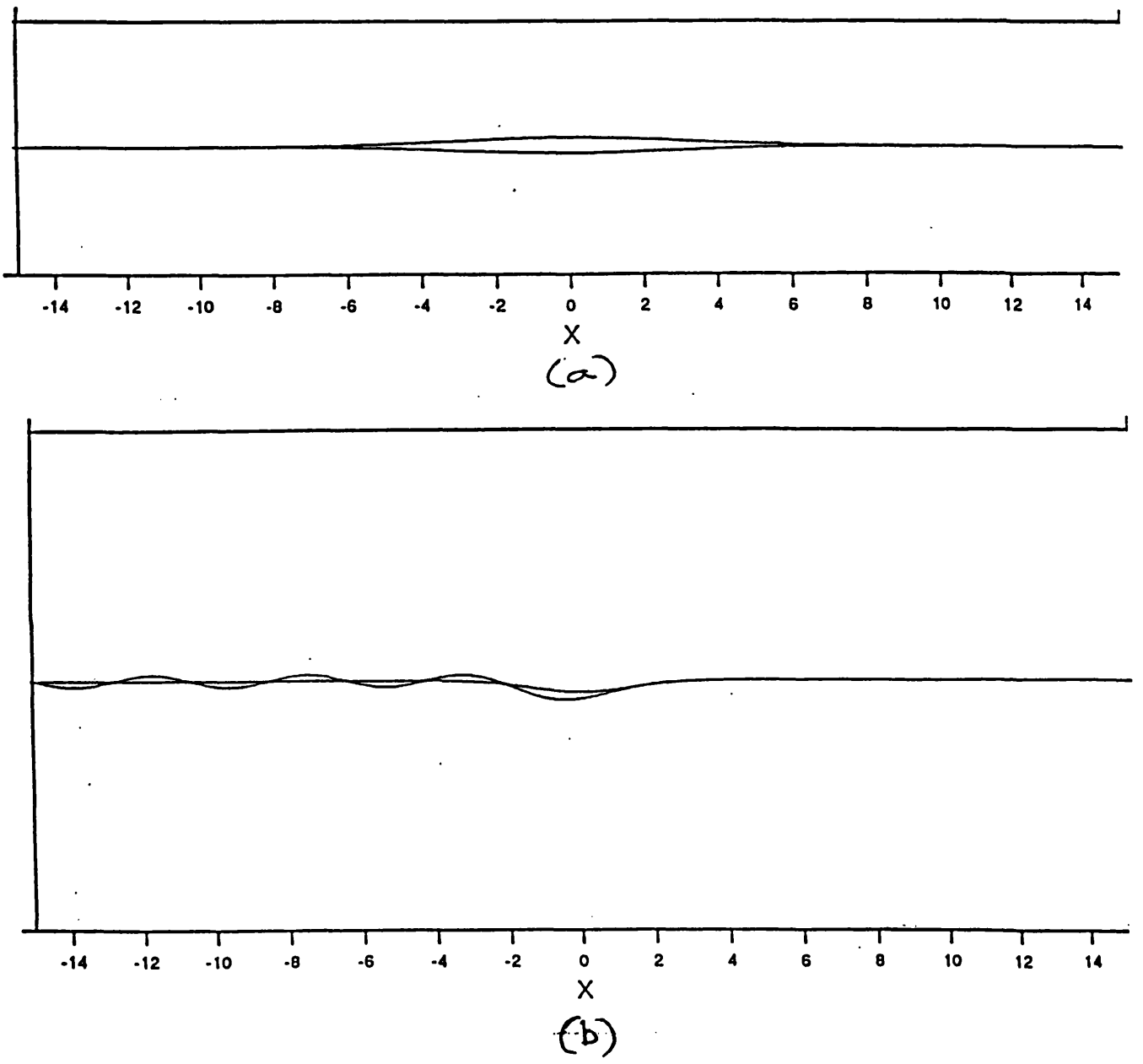

Figure 5.4

The results for the limiting case of small B. (a) The symmetric case $S < 4/\pi$. Here S = 1, A = 4 and B = $.025\pi$. (b) The lee wave generated when $S > 4/\pi$. Here S = 3, A = 4 and B = $.025\pi$.

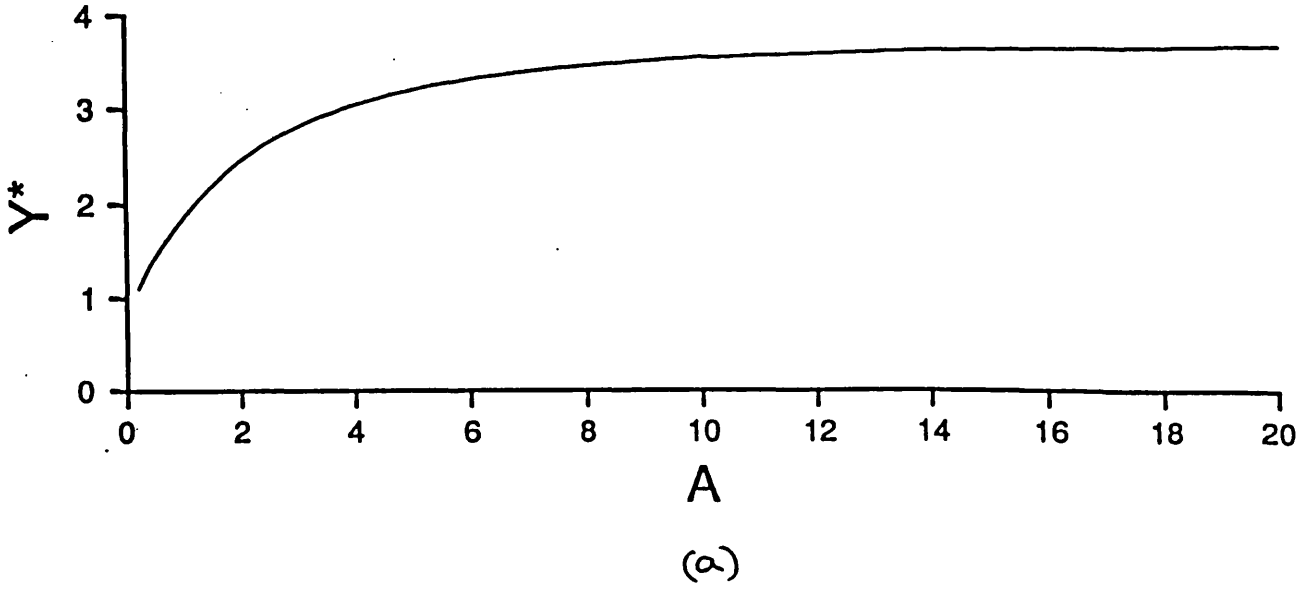

(a)

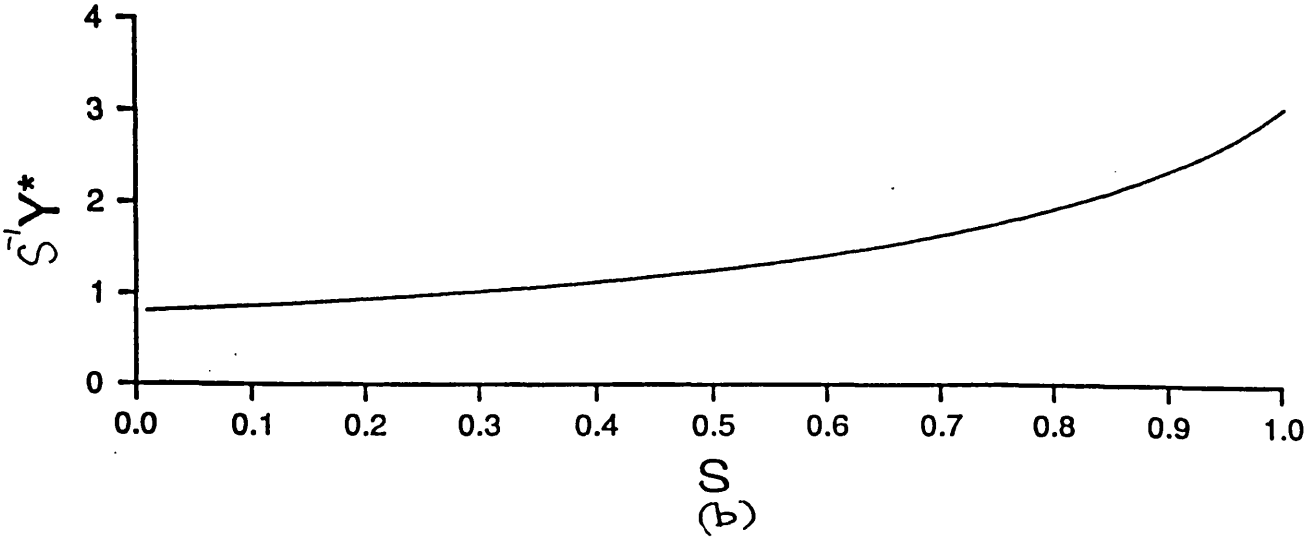

(b)

Figure 5.5

(a) The maximum deviation of $B^{-1}Y$ from $\pi/2$, given by Y^*, against A, for S = 1. (b)$S^{-1}Y^*$ against S for A = 4, S < $4/\pi$.

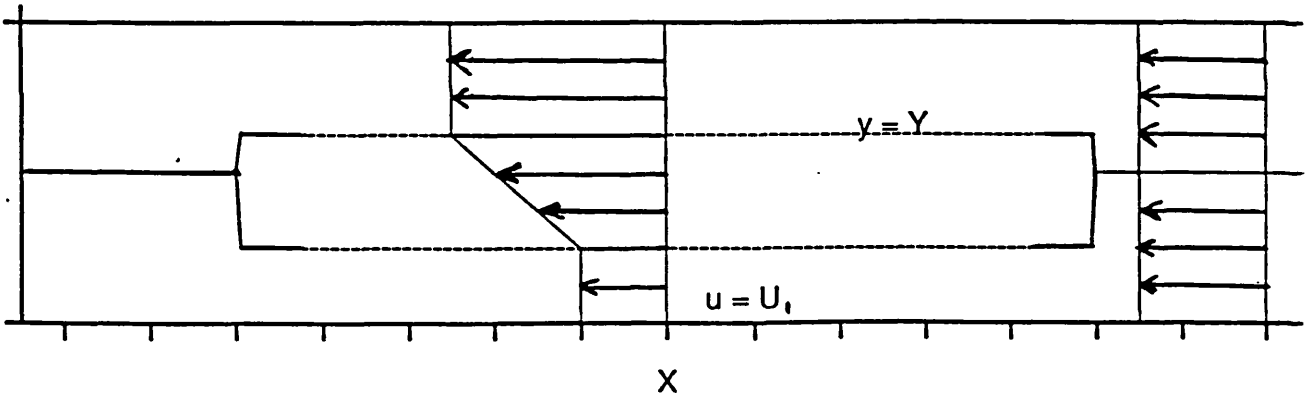

Figure 5.6
The model flow for the limiting case of large A. Two strips containing uniform flow are separated by a shear layer.

the distance from $y = \pi$ to the interface $y = Y$, where $Y > Y_{TOP}$ at the perturbation, then Y_1 is given by

$$Y_1^3-2\pi Y_1^2-Y_1\left[B^2-\pi(B+.75\pi+2U/S)\right]-U\pi^2/S = 0. \qquad (5.3.19)$$

It is also possible that $Y < Y_{TOP}$ at the perturbation, in which case the slightly different flux equations lead to the following equation for Y_2, the distance from $y = \pi$ to $y = Y$.

$$Y_2^3-\pi Y_2^2-Y_2\left[(B+.5\pi)^2-2U\pi/S\right]-U\pi^2/S+\pi(B+.5\pi)^2 = 0. \qquad (5.3.20)$$

Valid roots of these equations are those which tend to $\pi/2$ as $B \to 0$. Equation (5.3.19) has no valid roots in the range $0 < Y_1 < \pi/2 + B$ if $S > 4/\pi$. Thus for such values of S there is no solution which decays towards $\pi/2$ as $|x| \to \infty$ and which bows out towards the wall at $y = \pi$ at the perturbation. Equation (5.3.20) has no valid roots in the range $\pi/2 + B < Y_2 < \pi$ if $S < 4/\pi$. Thus for this range of values of S the only solution possible for $Y(x)$ is $Y_1(x)$. Figure 5.7(a) shows a typical solution for $Y_1(x)$. Here $B = \pi/4$, $S = 1$ and $A = 8$. For $S > 4/\pi$ equation (5.3.20) has a valid root in the required range only for values of B below a certain critical value, which depends on S. Figure 5.7(b) shows a typical solution for $Y_2(x)$. Here $B = \pi/8$, $S = 6$ and $A = 8$. The critical values for B are shown in Figure 5.8. For S near to $4/\pi$ the critical value for B is very small, i.e. there is only a small range in which a symmetric, decaying solution can be found. As S increases, the critical value for B tends to $\pi/2$, i.e. symmetric solutions can be found for any value of B. The roots for Y_1 and Y_2 for various values of (S,B) are shown on Figure 5.9. For $S < 4/\pi$ there are roots for Y_1, shown on the lower half of the figure. As $S \to 0$, $Y_1(0) \to SB(\pi-B)/4$ in agreement with the result of §5.3.1. As $B \to$

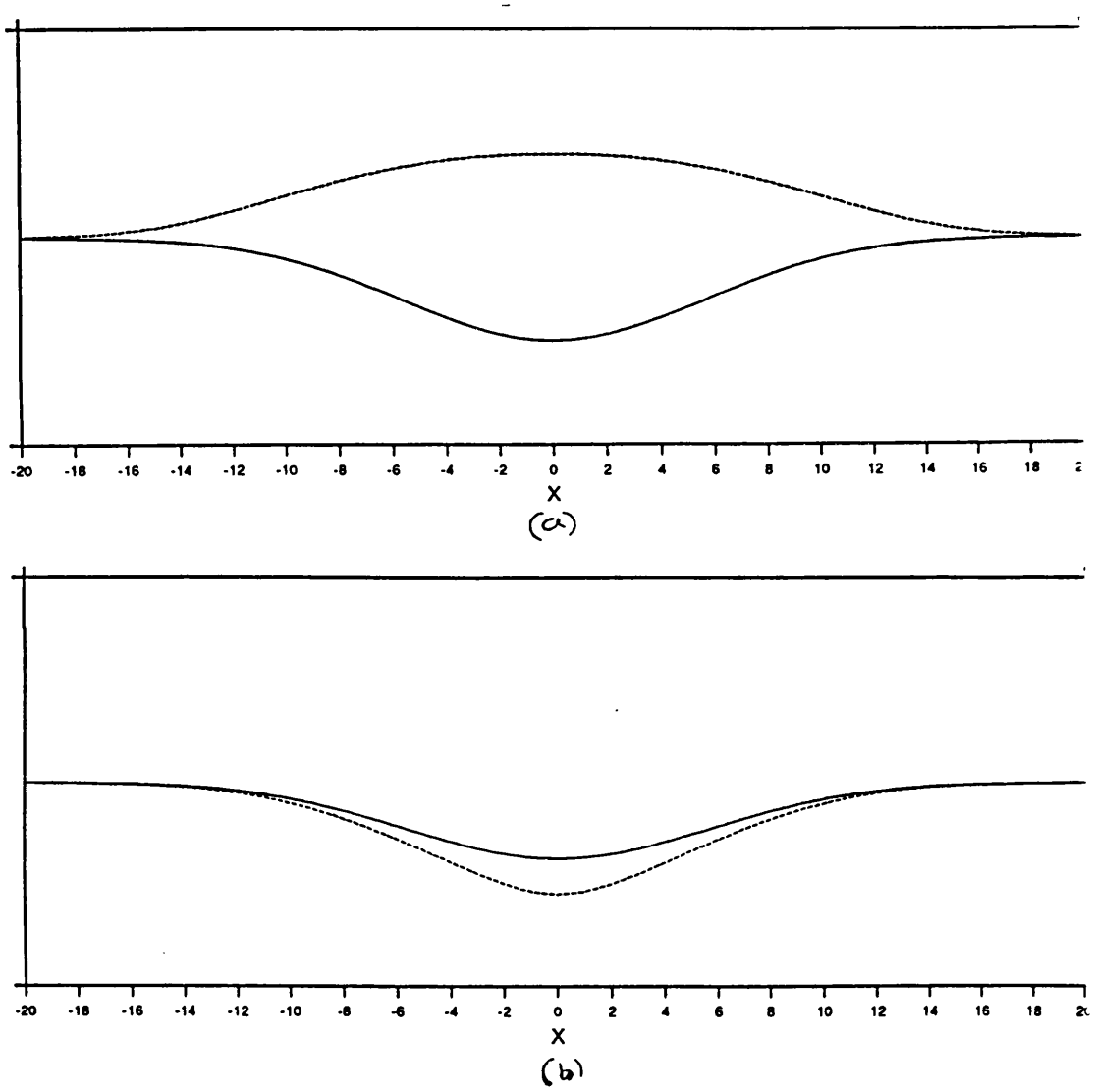

Figure 5.7

Typical solutions for Y(x). (a) The supercritical case. S = 1, B = $\pi/4$, A = 8. (b) The subcritical case. S = 6, B = $\pi/8$, A = 8.

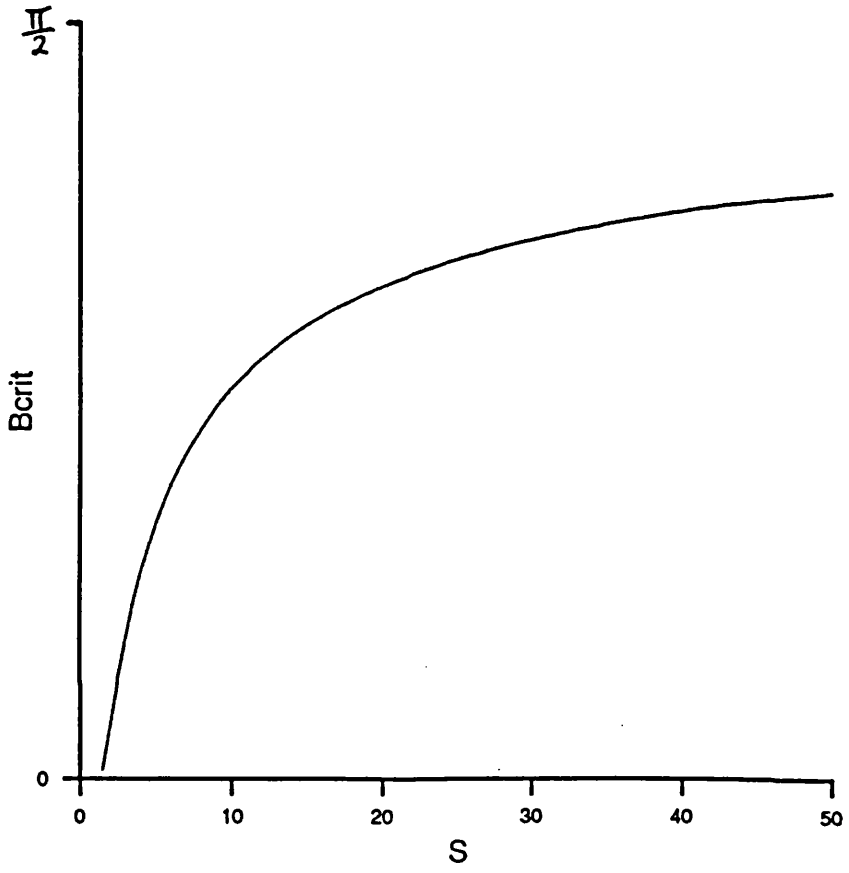

Figure 5.8

The critical values for B, above which no symmetric solutions can be found in the longwave limit for $S > 4/\pi$. As $S \to \infty$ the critical value for B tends to $\pi/2$.

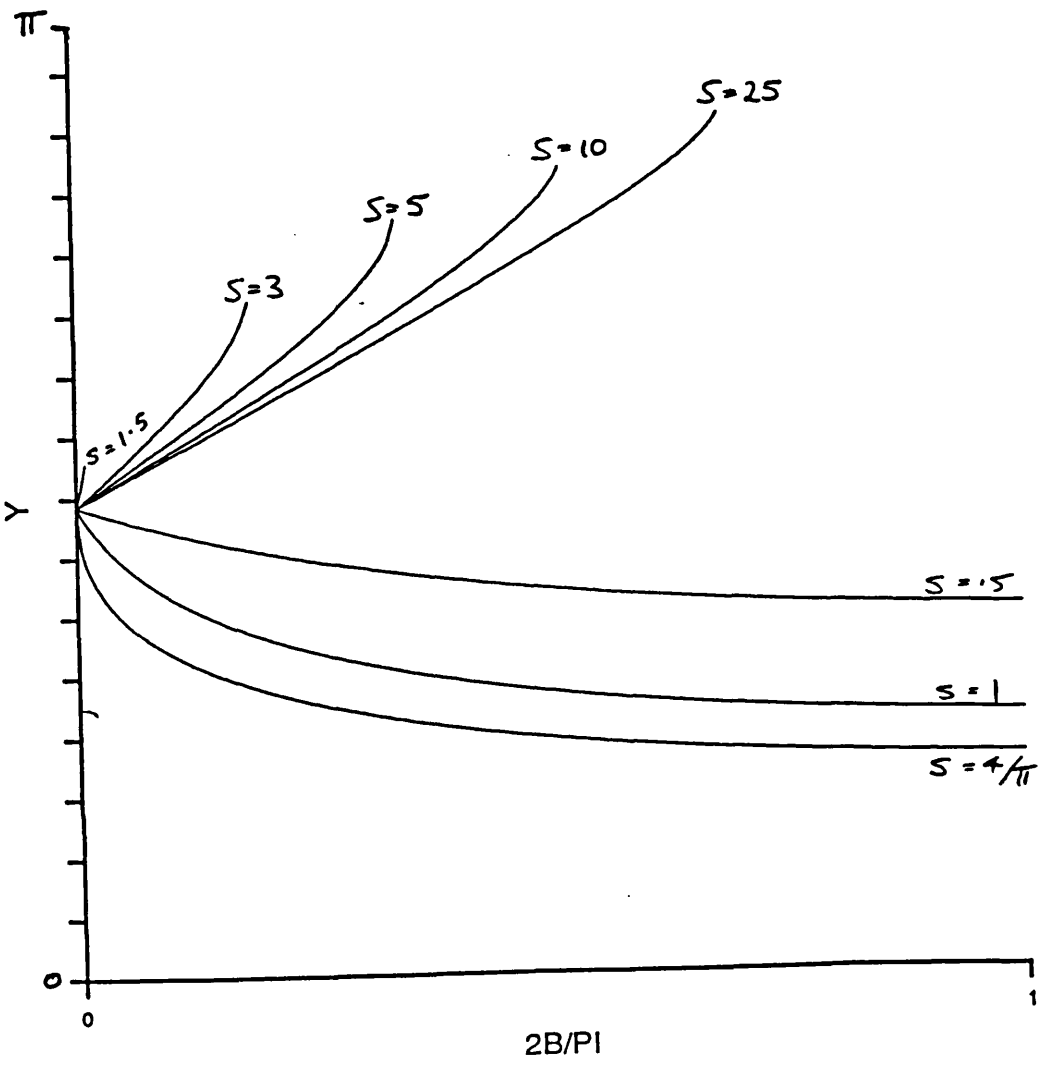

Figure 5.9

The symmetric solutions for Y, given by Y_1 and Y_2, against B for various values of S. For $S < 4/\pi$, $Y = Y_1$ and for $S > 4/\pi$, $B < B_{crit}$, $Y = Y_2$.

0, $Y_1(0) \rightarrow SB\pi/(4-S\pi)$ in agreement with §5.3.2. For $S > 4/\pi$ there are roots for Y_2, shown on the upper half of the figure, for values of B below the critical values of Figure 5.8.

Thus there is a wide range of values for (S,B) for which no solution of Y(x) which decays towards $\pi/2$ as $|x| \rightarrow \infty$ exists. We therefore allow an asymmetric solution for Y(x), which tends to two constant values up- and downstream of the perturbation. This possibility is illustrated in Figure 5.10. As $x \rightarrow \infty$, $Y(x) \rightarrow \pi/2 + C$ and as $x \rightarrow -\infty$, $Y(x) \rightarrow \pi/2 - D$. Again the conservation of mass flux in the regions $y > Y(x)$ and $y < Y(x)$ provides the necessary equations and again this leads to two equations, depending on whether Y lies in the deeper or the shallower region:

$$Y_1^3-2\pi Y_1^2-Y_1\left[C^2+B^2-2U\pi/S+\pi(C-.75\pi-B)\right]-U\pi(\pi-2C)/S=0 \qquad (5.3.21)$$

$$Y_2^3-\pi Y_2^2-Y_2\left[C^2+(B+.5\pi)^2+\pi C-2U\pi/S\right]-U\pi(\pi-2C)/S+\pi(B+.5\pi)^2=0 \qquad (5.3.22)$$

A similar equation is found for D. As $C \rightarrow 0$, equations (5.3.19) and (5.3.20) are recovered.

For a given maximum value of B, B_{MAX} say, i.e. for a given $Y_{TOP}(0)$, the upstream constant C may be determined. We assume that the root for Y(x) required is that for which the maximum allowed value of B is B_{MAX}. The value of this Y(x) for B = 0 then gives us C. This value of C may then be used in equations (5.3.21) and (5.3.22) to give Y(x) for any value of $B < B_{MAX}$. These asymmetric solutions exist for those values of (S,B) for which no symmetric solutions could be found. Examples of the asymmetric predictions of this theory are shown in the following section, in which they are compared with the numerical results obtained using the contour dynamics method.

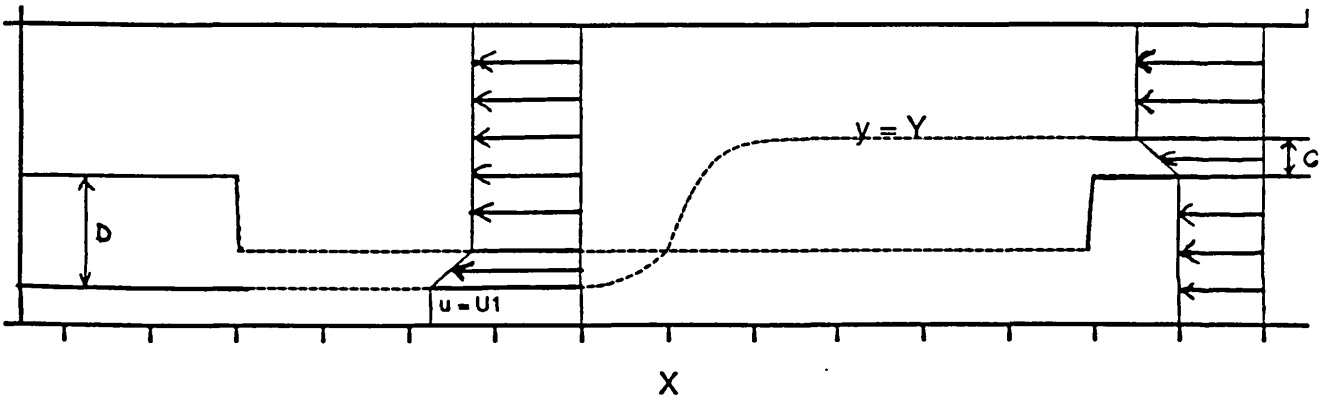

Figure 5.10

The model flow for the asymmetric case in the longwave limit. Upstream, the interface approaches $\pi/2 + C$, downstream the interface approaches $\pi/2 - D$.

An interesting analogy may be drawn between this longwave theory and hydraulic control theory in open channel flow, of depth h, over a submerged symmetric obstacle. The parameter $4/S\pi$ (= $4U/\delta fL\pi$) corresponds to the upstream Froude number, U^2/gh, the topographic perturbation corresponds to the submerged obstacle. Thus for $4/S\pi > 1$ the flow may be said to be supercritical and the advective effects of the oncoming flow dominate the topographic effects just as those of the oncoming flow in the open channel dominate the effects of gravity. No waves, topographic waves in the present case, gravity waves in the open channel, can propagate against this oncoming flow. In this case the free surface in the channel rises over the obstacle and the interfacial position in the present case bows towards the wall $y = \pi$.

If $4/S\pi$ is less than unity, the flow is said to be subcritical. This case corresponds to that with an upstream Froude number of less than unity which results in two possible flows. If the obstacle is less than a critical height a symmetric flow again results, this time with the free surface dropping above the obstacle. The flow therefore speeds up significantly at this point and for a sufficiently large obstacle the local Froude number may reach unity. An obstacle above the critical height acts as a hydraulic control, i.e. it causes the upstream conditions to be modified to accommodate the large obstacle and thus leads to an asymmetric free surface position, with a large upstream depth and a small downstream depth. For the present case, a symmetric interfacial position again results for values of B below the critical value, this time bowing towards the wall $y = 0$. The flow in the region between the interface and the wall at $y = 0$ must speed up at this point. In a similar way to the open channel theory, a stage is reached, as the size of the perturbation is increased, when the symmetric solution is no longer possible. This occurs when the speed required beside the wall $y = 0$ exceeds that which can be produced by the finite-width shear

layer with the given strength, S. In this case modification of the upstream conditions is again necessary and again the asymmetric result is produced.

§5.4 The contour dynamics results

§5.4.1 Comparison with the limiting cases.

The topographic perturbation is again taken to be of a Gaussian shape in this section. The contour dynamics algorithm was run first with parameter values close to those covered in the previous section, in order both to examine the range of validity of the theories, which are, of course, strictly valid only in their various limits, and to investigate the evolution of the flow from its initial state of uniform flow to these final states. The points in parameter space for which the computations were carried out are indicated by crosses on Figure 5.11.

Figure 5.12 shows the results for cases (a-c). In (a) S = .25 ; in (b) S = .5 and in (c) S = 1. In all three cases B = $\pi/8$, A = 2 and the time is given by t = 12. The predictions for Y(x) by the small-S theory are dashed in on the figures. These predictions are made using parameter values such that the area of the rectangular topographic perturbation is the same as that of the Gaussian topographic perturbation used in the computations, since regions of similar area would be expected to produce closer results than regions with the same height or length but differing areas. For small values of S the agreement is fairly good, the slight discrepancy apparently being due to the differing shapes of the perturbations, but as S is increased the disagreement grows and the range of validity of the small-S theory is clearly being exceeded by the case S=1. The figure illustrates the evolution of Y(x,t) in the fast case. A front forms, with an amplitude increasing with S, which moves off downstream, leaving behind the expected symmetric solution.

In the next figure, 5.13, the result of case (d) is shown. The parameter values for this case are those for case (c) except that B is now $\pi/4$. The amplitude of the

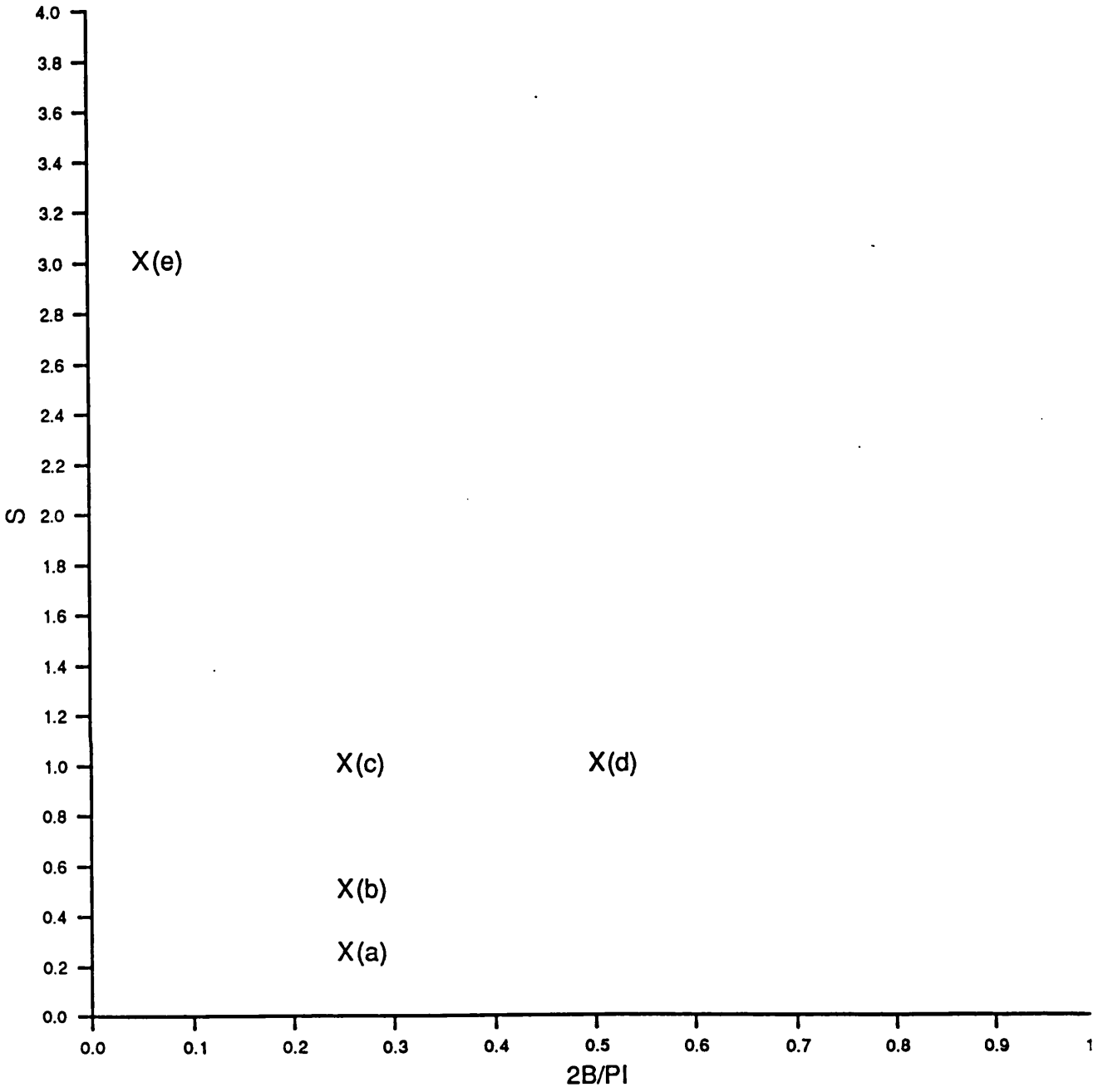

Figure 5.11

The points in parameter space corresponding to the computations carried out in §5.4.1, the results of which are shown in Figures 5.12, 5.13 and 5.14.

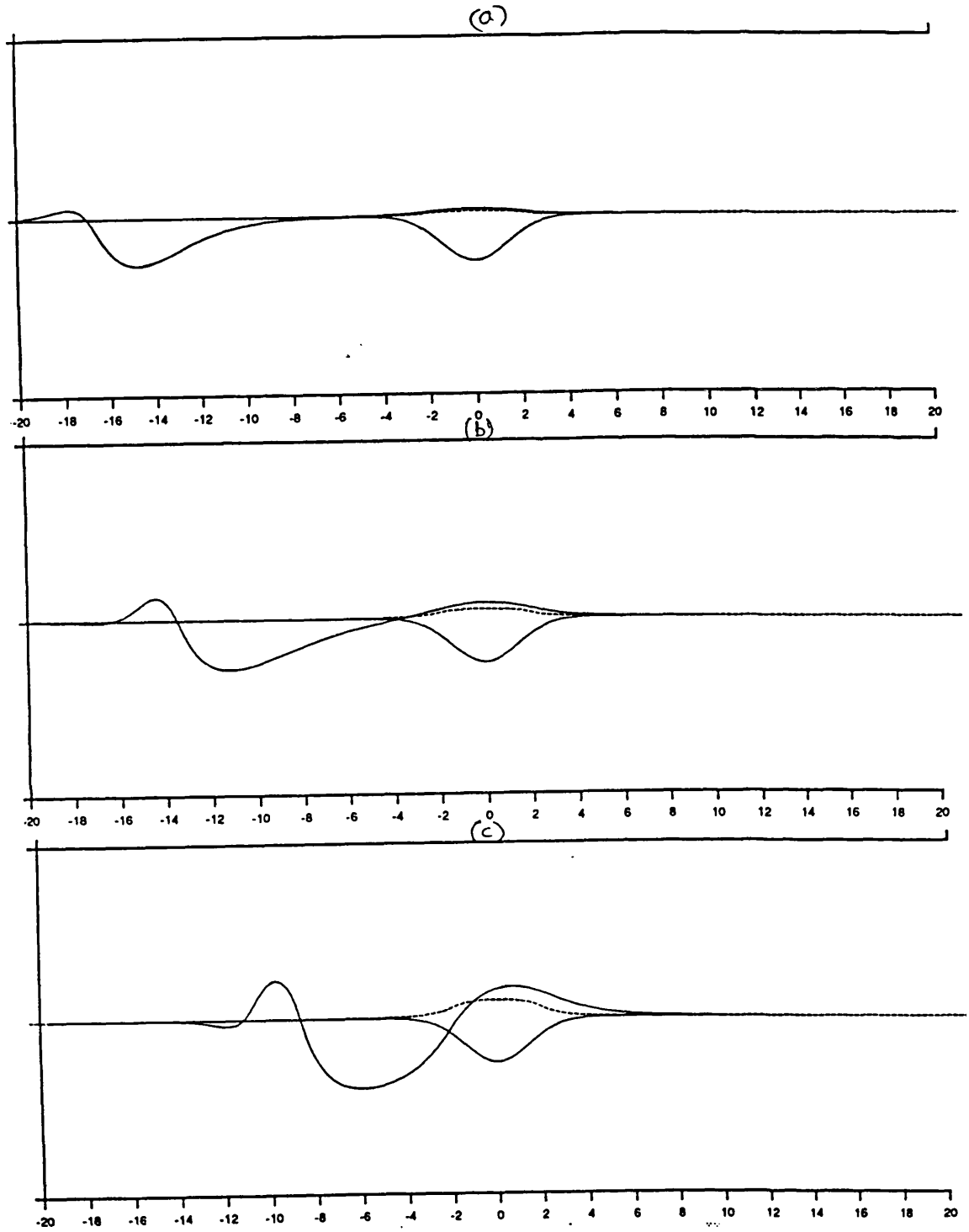

Figure 5.12

The contour dynamics results for the parameter values corresponding to the limiting case of §5.3.1. In all cases t = 12 and A = 2. The dashed line indicates the predictions of the small-S theory for a rectangular perturbation. (a) S = 1/4, B = π/8. (b) S = 1/2, B = π/8. (c) S = 1, B = π/8.

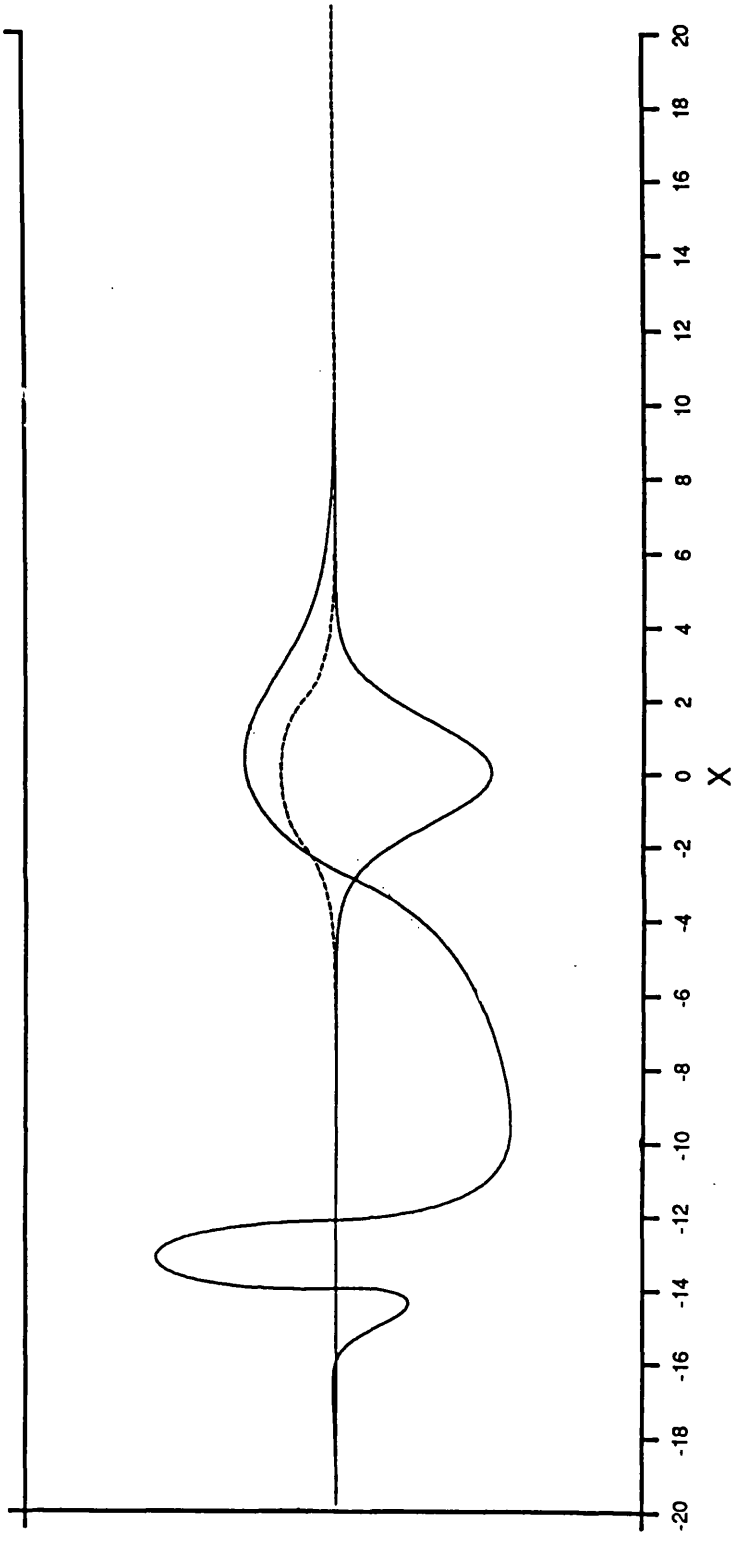

Figure 5.13

A larger value of B: S = 1, B = $\pi/4$, A = 2, t = 12.

front is increased by the larger value of B but the qualitative behaviour is similar to cases(a-c).

The small-B case is illustrated in Figure 5.14. Here A = 2, S = 3, t = 10 and B = $.025\pi$. As expected, as S is above the critical value of $4/\pi$, the downstream behaviour is wavelike. The amplitude seems at first to be larger than that predicted by the small-B theory. However the waves seen up- and downstream of the perturbation in the figure are longwave and shortwave transients respectively, which are predicted by the theory to have larger amplitudes than the standing wave of the steady state. Further work on this matter (Dr. P. Haynes, private correspondence) confirms that large amplitude transients can dominate the flow development for some considerable time.

Next, some cases with large values of A are considered and compared with the longwave theory of §5.3.3. Figure 5.15(a) shows the case with B = $\pi/4$, A = 8, S = 1, at times t = 15, 23. The evolution is qualitatively similar to that of the cases shown in Figure 5.11 - a front moves off downstream leaving behind the symmetric solution. The dashed line indicates the longwave prediction for this solution. As S < $4/\pi$, the predicted position of Y(x) lies between y = $Y_{TOP}(x)$ and y = π, and the agreement with the numerical results is very good. In Figure 5.15(b) a larger value of S is used. Here S = 6, A = $4\sqrt{2}$, B = $\pi/8$ and t = 17. The solution is now the symmetric solution lying between y = Y_{TOP} and y = 0. Again the agreement is very good.

Values of B above the critical value are used in the cases shown in Figure 5.16. Thus symmetric solutions are no longer possible according to longwave theory. In Figure 5.16(a) S = 6, A = 8, B = $\pi/5$ and t = 6, 12 and 18. It is shown that the asymmetric solution is attained as a wave train moves off downstream. Again the agreement with the theory is good. In Figure 5.16(b) S = 3, A = 8, B = $\pi/4$ and t = 10. In this case a greater upstream influence is both predicted and seen. The front moving

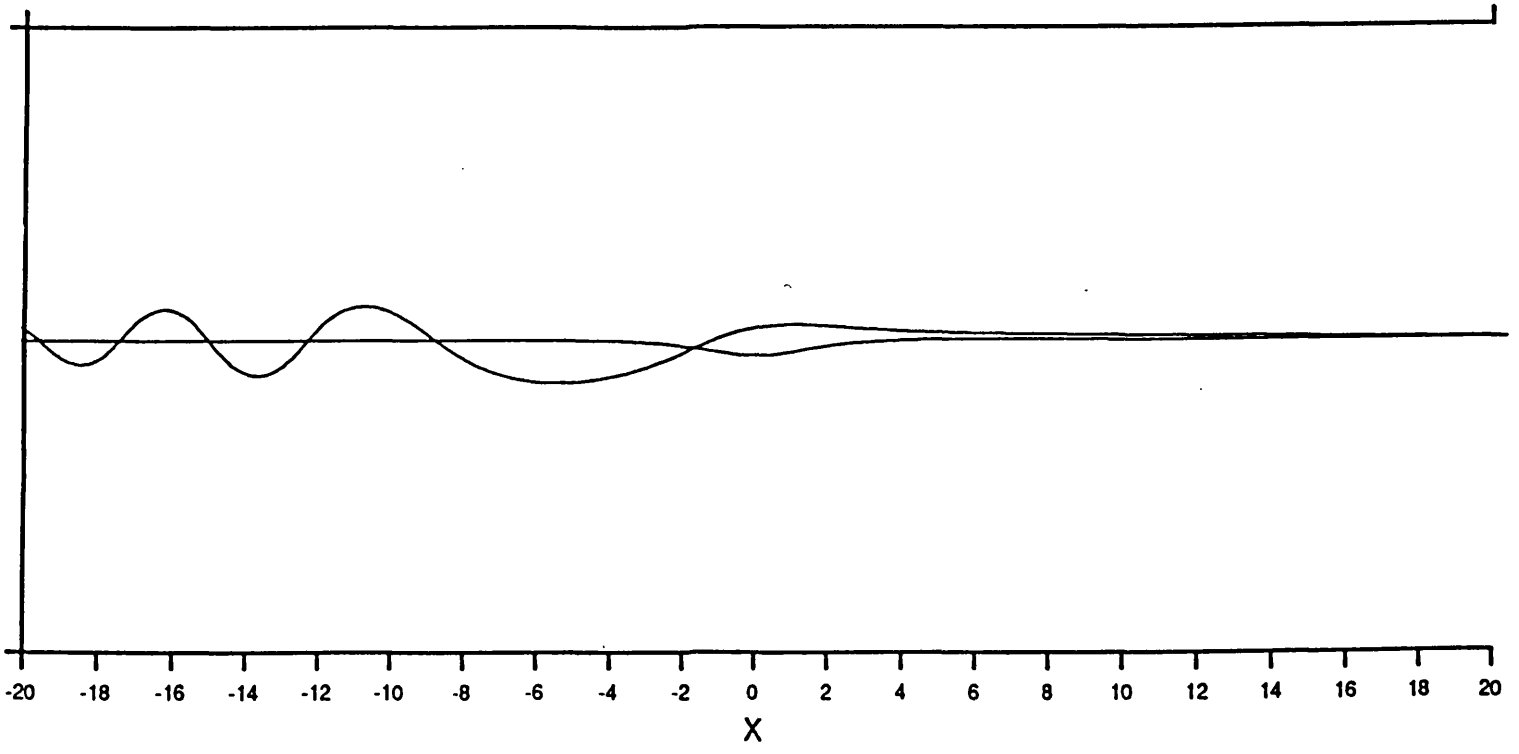

Figure 5.14
The contour dynamics results for the parameter values corresponding to the limiting case of §5.3.2. S = 3, B = .05, A = 2, t = 10.

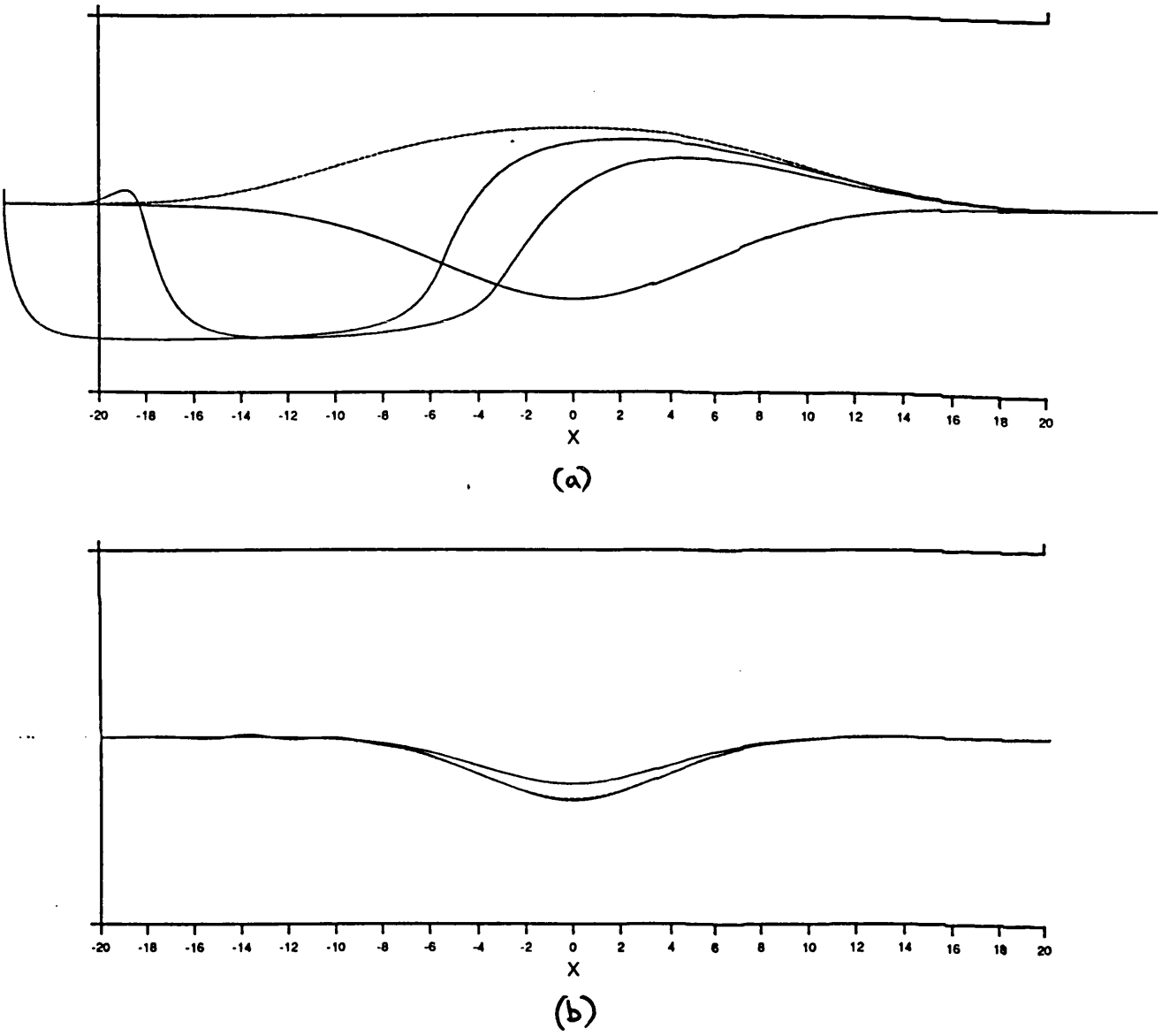

Figure 5.15

The contour dynamics results for the parameter values corresponding to the limiting case of §5.3.3 in the symmetric case. (a) A = 8, B = $\pi/4$, S = 1, t = 15, 23. (b) A = $4\sqrt{2}$, B = $\pi/8$, S = 6, t = 17.

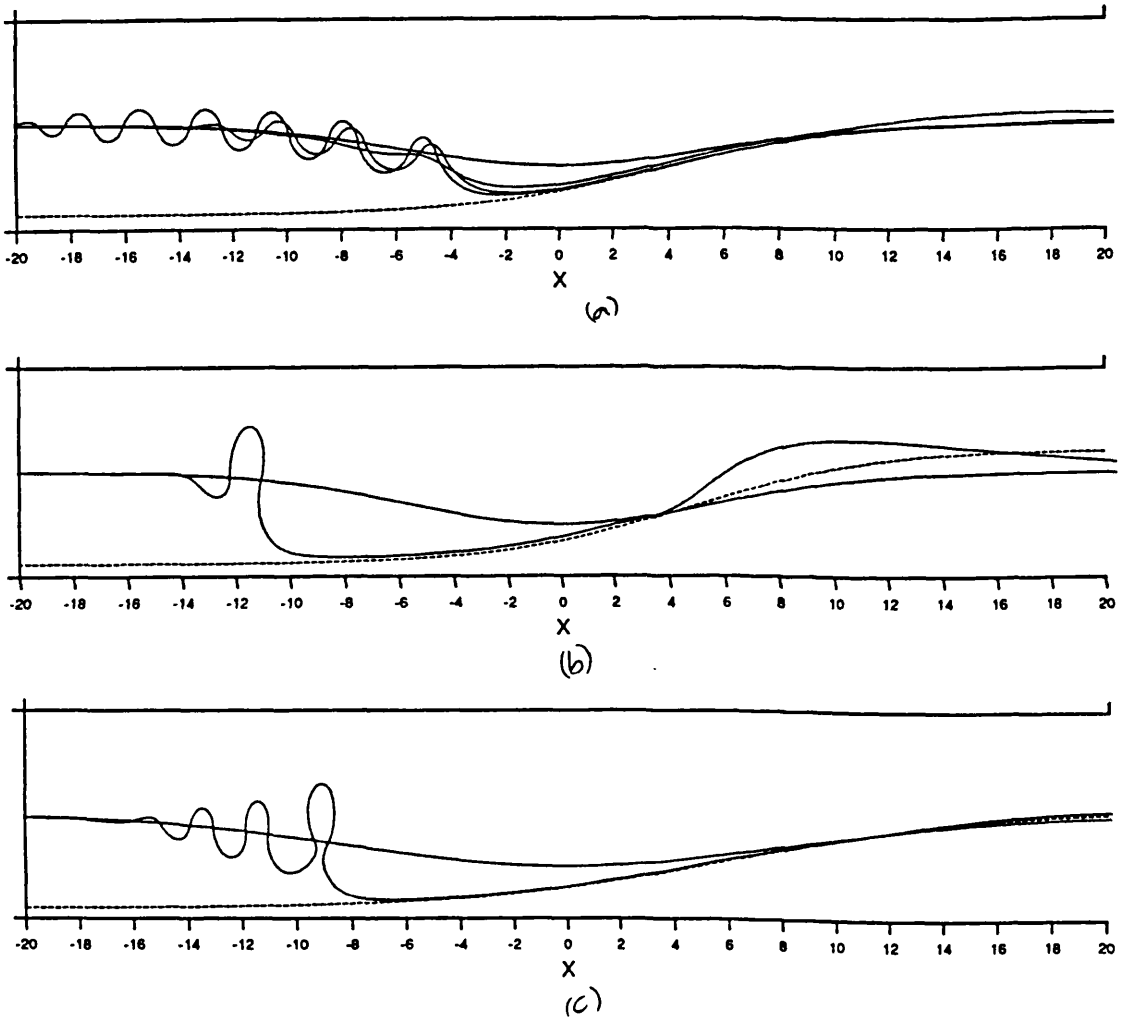

Figure 5.16

The contour dynamics results for the parameter values corresponding to the limiting case of §5.3.3 in the asymmetric case. (a) A = 8, S = 6, B = $\pi/5$, t = 6, 12, 18. (b) A = 8, S = 3, B = $\pi/4$, t = 10. (c) A = $8\sqrt{2}$, S = 6, B = $\pi/4$, t = 13.

downstream is larger and non-sinusoidal. Again the predicted interfacial position is approached as the front moves off. In Figure 5.16(c) the perturbation is still longer. Here $A = 8\sqrt{2}$, $B = \pi/4$, $S = 6$ and $t = 13$. Again the shortwave feature is non-sinusoidal and moves off downstream leaving behind the predicted asymmetric solution. Continuing the analogy with open channel hydraulic control theory given in the previous section, we may consider the fronts which move off up- and downstream, adjusting the flow to the asymmetric steady solution and producing upstream influence, as corresponding to travelling hydraulic jumps or bores.

§5.4.2 Other parameter regimes

We now consider the points in parameter space indicated by crosses on Figure 5.17. The results are shown in Figure 5.18. The longwave predictions are again shown (dashed), although $A = 2$ in all cases. In spite of this small value of A, the predictions still show good agreement with the numerical results. In Figure 5.18(a) $B = \pi/4$, $S = 3$ and $t = 5$. The region of negative vorticity to the downstream side of the perturbation is sufficiently large that we may expect it to be influenced by the image region in the wall $y = 0$. This pair of patches seem to act in a way similar to the translating pairs of Pierrehumbert (1980), mentioned in §2.3, and move off downstream together. Nearer to the step, however, this effect is diminished and this differential translation results in the overturning of the interface, in a fashion similar to that described by Pullin (1981). This effect is seen more clearly in Figure 5.18(b), where $B = 3\pi/8$, with all other parameter values as in the previous case. The negative vorticity region is brought still closer to the wall and the overturning process is faster. In Figure 5.18(c,d) a larger value of S is used, $S = 6$. Again $B = \pi/4$ and $3\pi/8$ respectively and the values

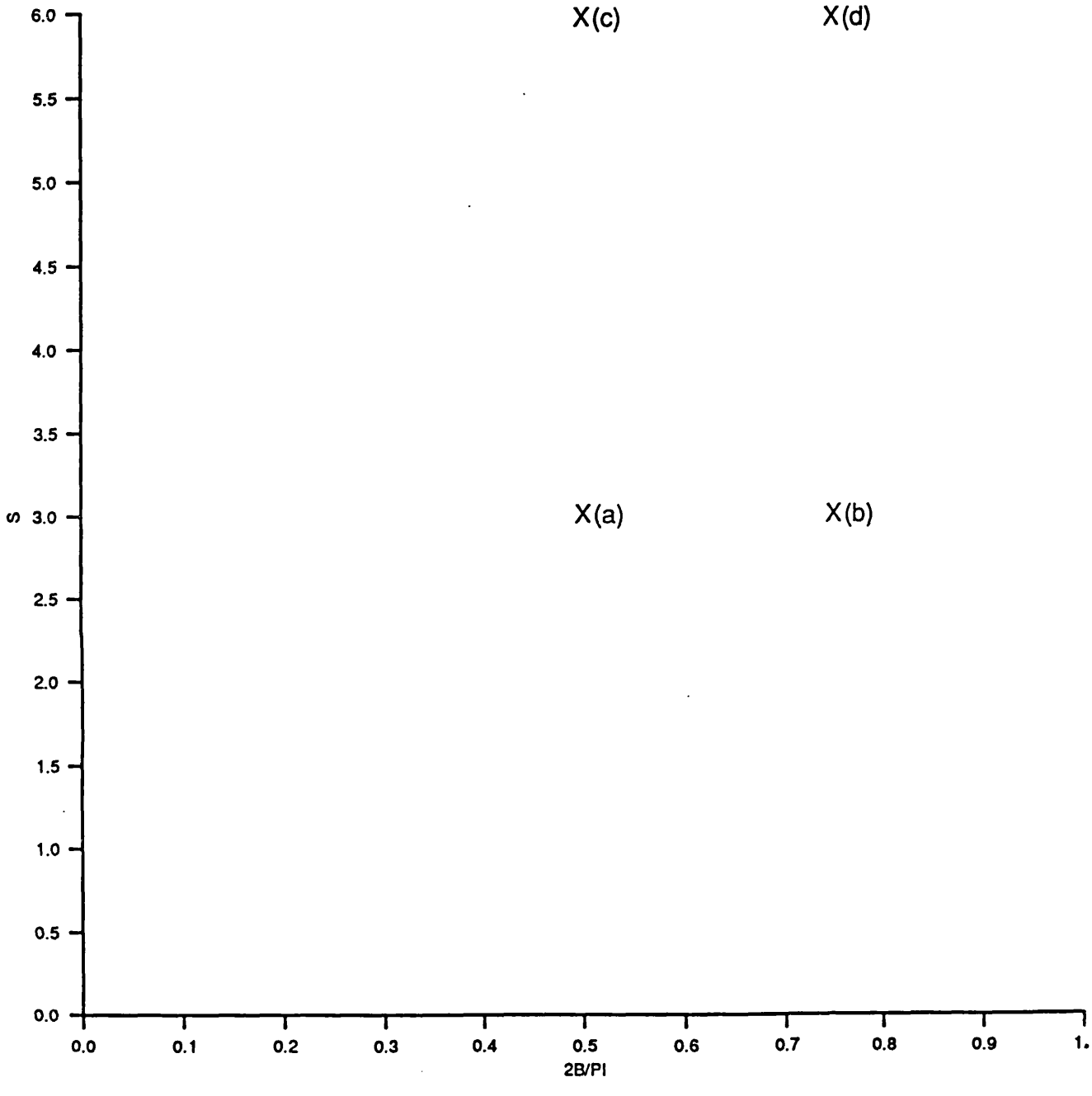

Figure 5.17

The points in parameter space corresponding to the computations carried out in §5.4.2, the results of which are shown in Figure 5.18.

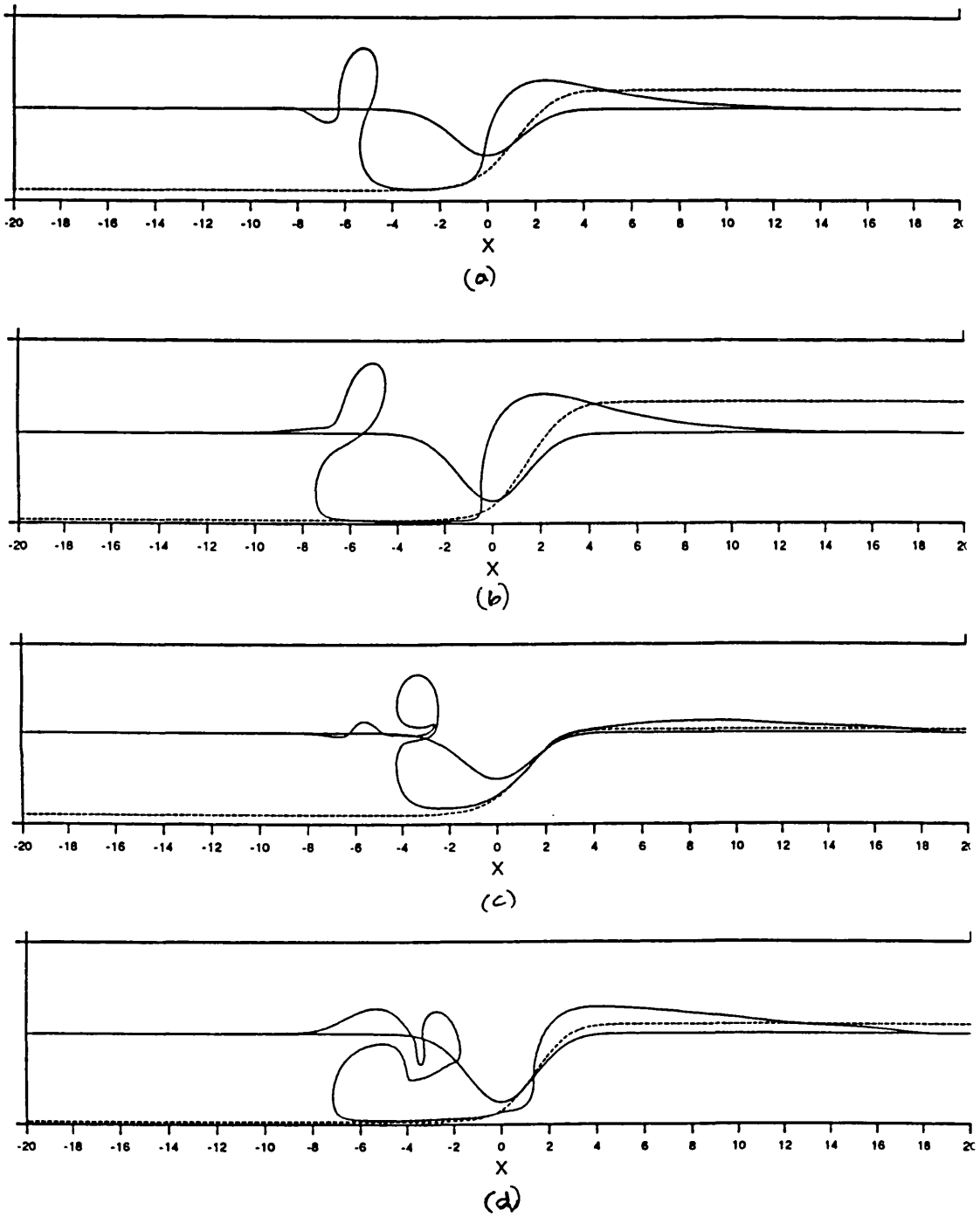

Figure 5.18

(a) S = 3, B = $\pi/4$, t = 5. (b) S = 3, B = $3\pi/8$, t = 5.

(c) S = 6, B = $\pi/4$, t = 4.5. (d) S = 6, B = $3\pi/8$, t = 4.

In all cases A = 2.

of t are 4 and 4.5. In 5.18(c) the overturning process has led to the formation and shedding of an eddy, while in 5.18(d) the developing eddy has been drawn into the shallow region and a highly complicated structure is evolving.

In all cases shown in this figure, the shortwave features, which the longwave theory obviously cannot capture, move off downstream as the negative vorticity patch translates along the wall, thus the asymmetric solution again results.

§5.5 Discussion

The evolution of a flow forced over a step change in bottom topography in a rapidly rotating channel has been investigated in various parameter regimes. Three limiting cases have been discussed and the resulting predictions compared with the results of the fully nonlinear time-dependent contour dynamics calculations. Further such calculations have been carried out, for parameter values outside the ranges of validity of the limiting cases, revealing new features in the development of the flows.

The first limit considered is that of small S, in which the oncoming flow is strong and all fluid is advected downstream. a permanent region of positive vorticity is formed at the topographic perturbation. As the value of S is increased, the size of this region grows. The time-dependent contour dynamics calculations reveal that this steady state is reached as a front moves off downstream, with an amplitude increasing with both S and B.

Flows with a larger value of S are considered in the second limiting case, that with values of B sufficiently small that the nonzero vorticity regions may be approximated as lying along the line $y = \pi/2$. If $S > 4/\pi$ a standing topographic wave is predicted downstream from the perturbation. The contour dynamics results for this regime show the large-amplitude transients which dominate the development of the flow, with long waves travelling upstream and short waves travelling downstream.

The final limiting case considered is the longwave limit. The theory predicts two qualitatively distinct results, depending on the values of S and B. If S is small, again the symmetric solution of the small-S theory is found. For values of $S > 4/\pi$, the topographic waves of the small-B theory are no longer possible in the longwave limit. In this case a symmetric solution for the

interface is again predicted, this time lying in the shallow region of the channel, provided B is below a critical value which depends on S. Thus in this case the permanent nonzero vorticity region formed contains negative relative vorticity. For values of B above this critical value, no symmetric solutions can be found and instead an asymmetric interfacial position is predicted, with the interfacial position tending to a constant value, greater than $\pi/2$, upstream and a different constant value, less than $\pi/2$, downstream. Thus the possibility of upstream influence must be allowed in modelling flows of this nature. An analogy is considered between this theory and hydraulic control theory in open channel flow.

The contour dynamics results show extremely good agreement with both the symmetric and asymmetric predictions of this limit. In the symmetric cases a front is again seen to move off downstream, as in the earlier cases. The larger value of A leads to a larger cross-stream width for the permanent vorticity region. The evolution of the asymmetric case may be understood in terms of translating vortex pairs. The region of negative relative vorticity produced at the perturbation as the fluid is advected up the step is sufficiently close to the wall at $y = 0$ to be affected by its image and hence to translate downstream, sweeping out the asymmetric shape as it does so. The region between the interface and the wall at $y = 0$ narrows as B or S is increased and, as the interface is a streamline in the steady state, this means that the flow between the interface and the wall becomes virtually blocked at the perturbation, since an upper limit is imposed on the flow speed in this region by the requirement that it match with the slower flow in the region $y > Y_{TOP}$ through a shear layer of finite width and strength. Hence the flow in the shallow region upstream must be slow and a shear layer is required to match this flow with the faster flow in the deeper region. The width of this shear layer therefore increases

with S and B, i.e. greater upstream influence is expected for larger values of S and B.

For large values of A the downstream-travelling front has a relatively small amplitude and little effect on the flow development. As the value of A is decreased, the longwave predictions still show remarkable agreeement with the numerical results. However, the amplitude of the front increases with decreasing A and now becomes non-sinusoidal and overturns, in some cases producing an eddy which may be shed or may be drawn into the shallow region, in which case the interface becomes extremely convoluted. It is expected that these shortwave features are carried downstream as the flow develops, however, thus again leaving a final flow similar to the longwave asymmetric prediction.

There is clearly further study possible on this topic, for example more complicated topography could be considered. I hope to continue with this work in the future.

The work of this chapter forms part of a forthcoming joint paper (Haynes, Hurst & Johnson, 1990).

List of references.

Abramowitz, M. & Stegun, I.A. (Eds.) 1964 "Handbook of Mathematical Functions." Dover, New York.

Deem, G.S. & Zabusky, N.J. 1978 Vortex waves: stationary "V-states", interactions, recurrence and breaking. Phys. Rev. Lett. 40 859-862

Dritschel, D.G. 1986 The nonlinear evolution of rotating configurations of uniform vorticity. J. Fluid Mech. 172 157-182

Dritschel, D.G. 1988 Contour surgery: a topological reconnection scheme for extended integrations using contour dynamics. J.Comp. Phys. 77 240-266

Dritschel, D.G. 1989 Contour dynamics and contour surgery: numerical algorithms for extended high resolution modelling of vortex dynamics in two-dimensional, inviscid, incompressible flows. Comp. Phys. Rept. 10 77-146

Dritschel, D.G. 1990 The stability of elliptical vortices in an external straining flow. J. Fluid Mech. 210 223-261

Gill, A.E. 1982 "Atmosphere-Ocean Dynamics." Academic Press.

Griffiths, R.W. & Linden, P.F. 1983 The influence of a sidewall on rotating flow over bottom topography. G.A.F.D. 27 1-33

Haynes, P.H.,Hurst, R.G.A. & Johnson, E.R. 1990 Rossby

wave hydraulics. (in preparation).

Hermann, A.J., Rhines, P.B. & Johnson, E.R. 1989 Nonlinear Rossby adjustment in a channel: beyond Kelvin waves. J. Fluid Mech. 205 469-502

Hide, R. 1961 Origin of Jupiter's Great Red Spot. Nature 190 895-896

Hide, R. & Ibbetson, A. 1966 An experimental study of "Taylor columns". Icarus 5 279-290

Huppert, H.E. 1975 Some remarks on the initiation of inertial Taylor columns. J. Fluid Mech. 67 397-412

Huppert, H.E. & Bryan, K. 1976 Topographically generated eddies. Deep Sea Res. 23 655-679

Hurst, R.G.A. & Johnson, E.R. 1990 Rapid formation of Taylor columns: obstacles against sidewalls. G.A.F.D. 52 105-124

Hurst, R.G.A., Johnson, E.R. & Davey, M.K. 1990 Topographic generation, trapping and capture of free-surface eddies. D.A.O. (submitted).

Ingersoll, A.P. 1969 Inertial Taylor columns and Jupiter's Great Red Spot. J. Atm. Sci. 26 744-752

Jacobs, S.J. 1964 The Taylor column problem. J. Fluid Mech. 20 581-591

Jacobs, P.A. & Pullin, D.I. 1989 Multiple-contour-dynamic simulation of eddy scales in the plane shear layer. J. Fluid Mech. 199 89-124

James, I.N. 1980 The forces due to geostrophic flow over shallow topography. G.A.F.D. 14 225-250

Jansons, K.M. & Johnson, E.R. 1988 Topographic Rossby waves above a random array of seamountains. J. Fluid Mech. 191 373-388

Johnson, E.R. 1978a Trapped vortices in rotating flow. J. Fluid Mech. 86 209-224

Johnson, E.R. 1978b Topographically bound vortices. G.A.F.D. 11 61-71

Johnson, E.R. 1982 The effects of obstacle shape and viscosity in deep rotating flow over finite height topography. J. Fluid Mech. 120 359-383

Johnson, E.R. 1983 Taylor columns in horizontally sheared flow. G.A.F.D. 24 143-164

Johnson, E.R. 1984 Starting flow for an obstacle moving transversely in a rapidly rotating fluid. J. Fluid Mech. 149 71-88

Johnson, E.R. 1985 Topographic waves and the evolution of coastal currents. J. Fluid Mech. 160 499-509

Kozlov, V.F. 1983 The method of contour dynamics in model problems of the ocean. Izvestiya, Atm. & Oceanic Phys. 19 no. 8 635-640

Lamb, H. 1932 "Hydrodynamics." Cambridge Univ. Press.

Longuet-Higgins, M.S. 1968 On the trapping of waves along

a discontinuity of depth in a rotating ocean. J. Fluid Mech. 31 417-434

Merkine, L. & Solan, A. 1979 The separation of flow past a cylinder in a rotating system. J Fluid Mech. 92 381-392

Overman, E.A. & Zabusky, N.J. 1982 Evolution and merger of isolated vortex structures. Phys. of Fluids 25 1297-1305

Page, M.A. 1987 Separation and free-streamline flows in a rotating fluid at low Rossby number. J. Fluid Mech. 179 155-177

Page, M.A. & Cowley, S.J. 1988 On the rotating-fluid flow near the rear stagnation point of a circular cylinder. J. Fluid Mech. 194 79-99

Pedlosky, J. 1987 "Geophysical Fluid Dynamics." Springer-Verlag.

Pierrehumbert, R.T. 1980 A family of steady, translating vortex pairs with distributed vorticity. J. Fluid Mech. 99 129-144

Polvani, L.M., Zabusky, N.J. & Flierl, G.R. 1989 Two-layer geostrophic vortex dynamics. Part 1. Upper-layer V-states and merger. J. Fluid Mech. 205 215-242

Pratt, L.J. & Stern, M.E. 1986 Dynamics of potential vorticity fronts and eddy detachment. J. P. O. 16 1101-1120

Proudman, J. 1916 On the motion of solids in a liquid

possessing vorticity. Proc. Roy. Soc. A92 408-424

Pullin, D.I. 1981 The nonlinear behaviour of a constant vorticity layer at a wall. J. Fluid Mech. 108 401-421

Pullin, D.I. & Jacobs, P.A. 1986 Inviscid evolution of stretched vortex arrays. J. Fluid Mech. 171 377-406

Pullin, D.I., Jacobs, P.A., Grimshaw, R.H.J. & Saffman, P.G. 1989 Instability and filamentation of finite-amplitude waves on vortex layers of finite thickness. J. Fluid Mech. 209 359-384

Rosenhead, L. 1963 "Laminar Boundary Layers." Oxford Univ. Press

Rossby, C.-G.1937 On the mutual adjustment of pressure and velocity distributions in certain simple current systems. Vol. I. J. Mar. Res. 1 15-28

Rossby, C.-G.1938 On the mutual adjustment of pressure and velocity distributions in certain simple current systems. Vol. II. J. Mar. Res. 1 239-263

Saffman, P.G. & Szeto, R. 1980 Equilibrium shapes of a pair of equal uniform vortices. Phys. of Fluids 23 2339-2342

Shaw, N. 1916 Gradient wind in meteorological glossary. Meteorological Office, H.M. Stationary Office, London.

Stern, M.E. 1986 On the amplification of convergences in coastal currents and the formation of "squirts". J. Mar. Res. 44 403-421

Stern, M.E. 1989 Evolution of locally unstable shear flow

near a wall or a coast. J. Fluid Mech. 198 79-99

Stern, M.E. & Pratt, L.J. 1985 Dynamics of vorticity fronts. J. Fluid Mech. 161 513-532

Stewartson, K. & Cheng, H.K. 1979 On the structure of inertial waves produced by an obstacle in a deep,rotating container. J. Fluid Mech. 91 415-432

Taylor, G.I. 1917 Motion of solids in fluids when the flow is not irrotational. Proc. Roy. Soc. A93 99-113

Taylor, G.I. 1923 Experiments on the motion of solid bodies in rotating fluids. Proc. Roy. Soc. A104 213-218

Thomson, W. (Lord Kelvin) 1879 On gravitational oscillations of rotating water. Proc. Roy. Soc. Edinburgh 10 92

Walker, J.D.A. & Stewartson, K. 1972 The flow past a circular cylinder in a rotating frame. J. Appl. Math. & Phys. 23 745-752

Zabusky, N.J., Hughes, M.H. & Roberts, K.V. 1979 Contour dynamics for the Euler equations in two dimensions. J. Comp. Phys. 30 96-106

Zabusky, N.J. & Overman, E.A. 1983 Regularization of contour dynamical algorithms. 1. Tangential regularization. J. Comp. Phys. 52 351-373